Generation of Mid-Infrared Frequency Combs for Spectroscopic Applications

by

Daniel L. Maser

B.A., University of California, Berkeley, 2011

M.S., University of Colorado Boulder, 2014

A thesis submitted to the
Faculty of the Graduate School of the
University of Colorado in partial fulfillment
of the requirements for the degree of
Doctor of Philosophy
Department of Physics
2017

This thesis entitled:
Generation of Mid-Infrared Frequency Combs for Spectroscopic Applications
written by Daniel L. Maser
has been approved for the Department of Physics

Prof. Scott Diddams

Prof. Juliet Gopinath

Date

The final copy of this thesis has been examined by the signatories, and we find that both the content and the form meet acceptable presentation standards of scholarly work in the above mentioned discipline.

Maser, Daniel L. (Ph.D., Physics)

Generation of Mid-Infrared Frequency Combs for Spectroscopic Applications

Thesis directed by Prof. Scott Diddams

Mid-infrared laser sources prove to be a valuable tool in exploring a vast array of phenomena, finding their way into applications ranging from trace gas detection to X-ray generation and carbon dating. Mid-infrared frequency combs, in particular, are well-suited for many of these applications, owing to their inherent low-noise and broadband nature. Frequency comb technology is well-developed in the near-infrared as a result of immense technological development by the telecommunication industry in silica fiber and the existence of readily-available glass dopants such as ytterbium and erbium that enable oscillators at 1 and 1.5 µm. However, options become substantially more limited at longer wavelengths, as silica is no longer transparent and the components required in a mid-infrared frequency comb system (oscillators, fibers, and both fiber and free-space components) are far less technologically mature.

This thesis explores several different approaches to generating frequency comb sources in the mid-infrared region, and the development of sources used in the nonlinear processes implemented to reach these wavelengths. An optical parametric oscillator, two approaches to difference frequency generation, and nonlinear spectral broadening in chip-scale waveguides are developed, characterized, and spectroscopic potential for these techniques is demonstrated. The source used for these nonlinear processes, the erbium-doped fiber amplifier, is also studied and discussed throughout the design and optimization process. The nonlinear optical processes critical to this work are numerically modeled and used to confirm and predict experimental behavior.

Dedication

In memory of Esther Lutwak and Robert Nathan Maser.

Acknowledgements

This thesis would not have been possible without the help and support of countless others. I would like to thank:

- my advisor, Scott Diddams, for leading and teaching me for the past four and half years,
- Gabe Ycas, for being an invaluable resource throughout each project, instilling most of the skills I needed to accomplish this work,
- Lora Nugent-Glandorf, who guided me during my start at NIST and provided regular assistance with my early projects, especially the optical parametric oscillator,
- Flavio Cruz, for designing and setting up the first generation of the difference frequency generation system and contributing time-domain numerical modeling,
- Nima Nader, for fabricating and coupling the 3 µm source into the silicon waveguides, enabling our spectral and dual comb measurements,
- my other past and present labmates, especially Andrew Klose, A. J. Metcalf, Alex Lind, Ryan Terrien, Henry Timmers, and Abijith Kowligy, who have all taken time at NIST to assist me along the way,
- my parents Ken Maser and Susan Lutwak, my brother Gabe, and my sister-in-law Jana, for their long-distance support throughout my graduate school career,
- Patrick Lavin and Andrew Koller, for sharing their Sundays with me during Patriots season,
- Nick Adams, Aaron Wolf, Martin Cuddy, Jeff Chin, John Coglianese, and my other close Arlington friends, for our cherished annual group trips,
- Ben Smith, Robyn Comfort, Laura Mack, Ben Weise, and Katie Fleeman, for writing, texting, messaging, and otherwise maintaining our wonderful friendships from Cal Band,
- Wayne and Jackie Seltzer, for welcoming me and becoming my local Jewish family,
- the Cal Alumni community, for extending their love and support to a fellow Golden Bear, and
- Will Lewis, Adam Green, and Claire Opel, for being dependable friends when I need them the most.

Contents

Chapter

1 Introduction and Background **1**

1.1 Historical Background 1

1.2 The Need for Sensitive, Broadband Sources for Molecular Spectroscopy 2

1.3 Optical Frequency Combs 3

1.4 Frequency Comb Spectroscopy 5

1.5 Reaching the Mid-Infrared and Other Applications 5

1.6 Alternate Methods to Generate Mid-Infrared Radiation 9

1.7 Dual Comb Spectroscopy and Other Measurement Techniques 12

1.8 Thesis Outline 15

2 Theory of Three- and Four-Wave Mixing **16**

2.1 Introduction 16

2.2 Microscopic Nature of Nonlinear Susceptibility 17

2.3 $\chi^{(2)}$ Processes and Three-Wave Mixing 20

2.3.1 Test Case: Continuous-Wave, Undepleted Pump 25

2.4 $\chi^{(3)}$ Processes and Four-Wave Mixing 27

2.4.1 Test Cases from Literature 30

3 Optical Parametric Oscillator **34**

3.1 Introduction 34

3.2 Methods . . . 35
3.3 Results . . . 40
3.4 Discussion and Simulations . . . 41
3.5 Conclusions . . . 44

4 Erbium-Doped Fiber Amplifier (EDFA) Development **46**
4.1 Introduction . . . 46
4.2 EDFA Design . . . 47
4.3 Approaches to EDFA Pulse Compression . . . 48
4.3.1 EDFA Design at Higher Repetition Rates . . . 48
4.3.2 Dispersion-Compensating Fiber . . . 51
4.3.3 Large Mode Area Fiber . . . 51
4.3.4 Silicon Prism Pair . . . 52
4.4 Simulation Testing . . . 54
4.4.1 Design Confirmation . . . 54
4.4.2 Exploring Other Options . . . 56
4.5 Bandpass Filtering . . . 57
4.6 PANDA Minimization . . . 58
4.7 Conclusion . . . 60

5 Difference Frequency Generation at 3 Microns **63**
5.1 Introduction . . . 63
5.2 Design and Characterization . . . 64
5.3 Application to MIR Molecular Spectroscopy . . . 75
5.4 Conclusion . . . 79

6 Extending Difference Frequency Generation to 5 Microns **80**
6.1 Introduction and Overview . . . 80

6.2 Theory . . . 81
6.3 Experimental Design and Results . . . 83
6.3.1 Experimental Setup . . . 83
6.3.2 Pump and Signal Characterization . . . 85
6.4 Results and Analysis . . . 87
6.4.1 Spectral Coverage . . . 87
6.4.2 Beam Characterization . . . 87
6.4.3 Power Measurements . . . 88
6.4.4 Bandwidth Comparison to Simulations . . . 90
6.4.5 Coherence and Noise Measurements . . . 92
6.5 Conclusions . . . 94

7 Spectral Broadening in the Mid-Infrared Using Waveguides **95**
7.1 Introduction . . . 95
7.2 Motivation . . . 95
7.3 Dispersion Engineering . . . 96
7.3.1 Bulk Dispersion . . . 96
7.3.2 Dispersion Control . . . 96
7.3.3 Waveguide Design . . . 98
7.3.4 Dispersion Simulations . . . 101
7.4 Waveguide Spectral Broadening . . . 106
7.4.1 Spectral Broadening in Silicon Nitride . . . 106
7.4.2 Spectral Broadening in Silicon . . . 107
7.5 RIN in Silicon . . . 108
7.6 5 µm Dual Comb Spectroscopy with Output of Silicon Waveguide . . . 109
7.7 Conclusion . . . 111

8 Conclusion **112**

Bibliography **114**

Appendix

A Mathematical Identities **122**

B List of Part Numbers and Manufacturers Used in Dissertation **123**

B.1 Oscillators 123

B.2 EDFA 123

B.3 YDFA Pre-Amp 124

B.4 High-Power YDFA 124

B.5 Pump Diode Controller Infrastructure 124

B.6 Nonlinear Crystals 125

B.7 Diagnostics 125

Tables

Table

B.1 Commercial oscillator used as basis for near-infrared frequency comb system. 123
B.2 List of parts used in PM EDFA and pulse compression testing in Chapter 4. 123
B.3 List of parts used in the PM YDFA. This device is used as a pre-amplifier to see the high-power ytterbium amplifier, used in difference frequency generation in Chapters 5 and 6. 124
B.4 Full list of parts used in the high-power PM YDFA used in difference frequency generation in Chapters 5 and 6 124
B.5 Hardware required for pump diode current and TEC control. 124
B.6 Nonlinear crystals featured in Chapters 3, 5, and 6. 125
B.7 Diagnostic tools used in the mid-infrared. 125

Figures

Figure

1.1 Representation of a frequency comb, plotted as power vs. frequency (ν). The vertical dashed lines show the spacing f_r (or f_{rep}) between neighboring comb modes counting from zero, and the solid vertical lines show the location of the comb modes in frequency space, offset from the dashed lines by the offset frequency f_0. Any given comb mode ν_n (or f_n) is therefore defined as $nf_r + f_0$. The solid curve shows comb's bandwidth in the frequency domain; it corresponds to the inverse of the pulse duration $\frac{1}{\tau}$ [1]. 4

1.2 A cartoon of a frequency comb (left) passing through a molecular absorption feature (middle) leaves the molecular imprint on the transmitted comb modes (right). 4

1.3 Top: atmospheric water vapor windows over a 1 km path. Bottom: background absorbance from CO_2 (purple), CH_4 (cyan), and H_2O (tan), in addition to chemical warfare agents, shown at 1 ppb concentration over 1 km, multiplied by 100 for clarity [2]. 6

1.4 Cartoon showing applications of mid-infrared sources. Spectroscopic applications of mid-infrared sources include medicine, industry, security and defense, and pure science, enabled by greater sensitivity. Outside of spectroscopy, mid-infrared sources can be implemented in high-harmonic generation, in order to produce higher-energy X-rays, and in optical microscopy, taking advantage of the spectral capabilities of mid-infrared sources while beating their traditional diffraction limit. 7

1.5 A summary of related literature regarding mid-infrared mode-locked lasers and quantum cascade lasers. Difference frequency generation (DFG) sources [3–24], optical parametric oscillators (OPOs) [25–31], quantum cascade lasers (QCLs) [32–40], mode-locked lasers [41–43], supercontinuum sources [44–46], microresonators [47–50], and the work discussed in this thesis [51–53] are plotted as power per mode vs. wavelength. 10

1.6 Simplified summary of the various mid-infrared generation techniques from Fig. 1.5. Many other mid-infrared sources (microresonators, mode-locked lasers, and supercontinuum generation) are unable to generate light beyond 4 µm. Quantum cascade lasers (QCLs) generate high power but with narrow bandwidth and limited tunability. Difference frequency generation (DFG) and optical parametric oscillators (OPOs) support widespread spectral coverage and broad instantaneous bandwidth. . 11

1.7 Survey of electromagnetic radiation sources, detection media, and measurement techniques. The left panel summarizes four sources that can cover molecular absorption features: incoherent blackbody sources, picosecond supercontinuum sources broadened with nonlinear fiber, frequency combs, and tunable single-frequency lasers. These can be implemented in several ways in order to perform a spectroscopic measurement, such as passing once through a gas cell, passing tens to hundreds of times through a multipass cell, passing orders of magnitude more times through a resonant cavity, and scattering off of a surface. Lastly, the spectroscopic signal can be detected through a variety of methods, such as the traditional Fourier-transform spectrometer, a spatially-separated grating spectrograph, a high-resolution spectrograph called a VIPA (virtually-imaged phased array), a lifetime measurement using a cavity ring-down spectrometer, a rapid time-domain measurement using a dispersed supercontinuum, and lastly, a dual-comb spectrometer. 13

1.8 Time domain representation of dual comb spectroscopy. Two frequency combs, of repetition rates f_r and $f_\mathrm{r} + \Delta$, interfere when combined and sensed by a detector when pulses arrive simultaneously. This first occurs at $t = 0$, then subsequently at time $t = 1/\Delta$, when the pulse-to-pulse walk-off fully "wraps around." 14

1.9 Frequency domain representation of dual comb spectroscopy. Two frequency combs, of repetition rates f_r and $f_\mathrm{r} + \Delta$, are combined and sensed by a detector, seen at left. The beats between the modes of the two combs generate a frequency comb in the RF with a mode spacing of Δ, shown at right. 14

2.1 Diagram demonstrating inversion symmetry. The cube at left exhibits inversion symmetry; each corner matches the color of that when each its coordinate's positions are inverted. The cube at right does not exhibit inversion symmetry; each corner matches the color when two of its coordinates are inverted, but not when all three are. 18

2.2 Cartoon of the difference frequency generation and optical parametric oscillation process. Pump photons (ω_p) drive the down-conversion process, which generates both signal (ω_s) and idler (ω_i) photons. 24

2.3 Comparison of analytical solution (Eqs. 2.60 and 2.61, black dots) to the integrated coupled equations (Eq. 2.52, blue line) for the strong pump case. Near-perfect agreement is seen. $\lambda_p = 1560$ nm, $\lambda_s = 2200$ nm, and $\lambda_i = 5360$ nm. $P_p = 25$ kW and $P_s = 100$ kW. The beam waist $w = 10$ mm. 27

2.4 Behavior of a pulse due to the nonlinear refractive index. Intensity is shown in grayscale, where the highest intensity is the darkest. The x-axis shows a dimensionless normalized frequency, where the centered frequency ($\nu - \nu_0$, where ν_0 is the central frequency) is multiplied by T_0, the pulse width. The y-axis shows the distance divided by $L_{NL} = (\gamma P_0)^{-1}$, the nonlinear length. 31

2.5 A fourth-order soliton propagating in optical fiber, the intensity of which is plotted both in time (left) and frequency (right). The x-axis of the left plot is delay divided by T_0, the pulse width. The x-axis of the right plot is frequency, plotted as in Fig. 2.4. The y-axis is distance divided by $L_D = T_0^2/|\beta_2|$, the dispersion length. 32

2.6 Three slices of Fig. 2.5, shown in time (top) and wavelength (bottom). Blue curves represent $z/L_{NL} = 0$, green is at 0.4, and red is at 0.8. 32

2.7 Full GNLSE simulation of a pulse propagating in silica fiber, regenerated from parameters listed in Ref. [54]. The Raman frequency shift is evident, as a band of spectral intensity is quickly shifted from the center frequency of 850 nm to 950 nm, and continues to shift to longer wavelengths as the pulse propagates. 33

3.1 Diagram depicting the doubly-resonant optical parametric amplification process. Pump photons (ω_p) are coupled into a cavity, where signal (ω_s) and idler (ω_i) photons are produced in a nonlinear crystal (here, silver gallium selenide) and amplified in the resonant cavity enclosed by mirrors M_1 and M_2. A portion of the signal and idler are coupled out of the cavity for measurements. 34

3.2 Schematic for the source used to pump the OPO. An erbium fiber oscillator generated comb light centered at 1.5 µm, which was amplified in an erbium-doped fiber amplifier. This spectrum was then broadened to 2 µm in highly nonlinear fiber (HNLF), and the remaining 1.5 µm light self-pumped the 2 µm portion of the spectrum in thulium/holmium co-doped fiber (THDF). The pulse was then stretched to avoid acquiring nonlinear phase in fiber, then amplified to 4.8 W in thulium fiber, pumped with an external diode via a pump-signal combiner (PSC). An isolator and collimator module (ICM) launched the amplified beam into free-space, where a grating compressor shortened the pulse, yielding 2.0 W of compressed output. 36

3.3 Left: Optical spectrum of the Tm:fiber amplifier output. Data were measured using a long-wave optical spectrum analyzer (OSA). Right: Interferometric autocorrelation (black), intensity autocorrelation (red), and Fourier-transformed and autocorrelated optical spectrum (yellow) of the amplified pump beam. The x-axis was calibrated by measuring how a delay introduced by a translation stage was mapped to the scope trace temporally. 37

3.4 Diagram of the experimental setup. Red indicates the pump beam, purple indicates the combination of pump, signal, and idler, and blue indicates the signal and idler with the pump removed by the long-pass filter (LPF). The 2 µm pump source (detailed in Fig. 3.2) was shaped by two cylindrical lenses (not shown) before entering the oscillator box through a Brewster-angled window. The pump light was coupled into the cavity through an output coupler (OC). A piezoelectric transducer (piezo) allowed the cavity length to be locked. The residual pump light and a small fraction of the generated light escaped the cavity through the output coupler. The photodetector (PD) is used to measure the depletion of the pump as it is converted into the signal and idler. A Fourier-transform spectrometer (FTS) was used to measure the wavelength of the produced light, and an InSb camera was used to image the generated beam. 37

3.5 Three sample spectra produced by the 1 mm crystal, denoting the spectral coverage of different signal-idler pairs. Shown are degenerate (red), nearly degenerate (blue), and non-degenerate (green) spectra. 38

3.6 Spectra generated in a 1 mm crystal, in ambient air. Top: oscilloscope trace of pump transmission vs. cavity length, showing the position of each resonance where 2 µm light was depleted as optical parametric oscillation occurred. First and last resonance positions are marked 1 and 27. Bottom: mid-infrared spectrum produced at each resonance position, corresponding to peaks marked in the top plot. Spectra are normalized individually to 1, vertically separated for clarity, and plotted on a logarithmic scale. 39

3.7 Spectra generated in a 1 mm crystal, plotted as in Fig. 3.6, with coarse cavity purging using dry nitrogen. 39

3.8 Spectra generated in a 0.5 mm crystal, plotted as in Fig. 3.6, with coarse cavity purging using dry nitrogen. 40

3.9 Atmospheric transmission for one round-trip around the cavity (3 meters) [55]. The prominent feature in the center, at 4.3 µm, is as a result of carbon dioxide. 41

3.10 Simulation of OPO without atmospheric absorption, plotted similarly to experimental data. Depletions in the 2 µm pump as a function of cavity length are shown at top, and the generated spectra as a function of wavelength and cavity length are plotted at bottom. 42

3.11 Simulation of OPO with atmospheric absorption. Generated spectra are shown at bottom, and corresponding pump depletions are shown at top. Compared to the simulation without absorption (Fig. 3.10), distinct gaps are seen in the idler spectrum at the strong carbon dioxide absorption feature near 4.2 µm, but the inclusion of absorption alone is unable to account for spectral gaps observed in experimental data. 43

3.12 Simulation of OPO with atmospheric absorption and dispersion. Generated spectra are shown at bottom, and corresponding pump depletions are shown at top. With the inclusion of both absorption, the simulated spectral gaps match those observed in experimental data. 44

3.13 One particular resonance position, plotted for two simulated cases (with and without atmospheric dispersion, in green and blue, respectively), as well as experimental data from the same resonance position (red). The effect of atmospheric dispersion is strongly evident and causes the spectral narrowing seen in experimental traces. . . 45

4.1 Schematic of a typical EDFA. Light from a non-PM oscillator is linearly polarized using quarter- and half-wave plates, and, after passing through an optical isolator, is coupled into PANDA (polarization-maintaining anomalous-dispersion single-mode fiber). The pulse is stretched in a short section of PANDA fiber, amplified in normal-dispersion erbium gain fiber while stretched to avoid pulse break-up, then compressed in PANDA before exiting the amplifier. Pump power is coupled into the amplifier using either one or two wavelength-division multiplexers (WDMs) using either two or three pump diodes. The output of the EDFA may be spectrally broadened to new wavelengths using highly nonlinear fiber (HNLF). Specific parts shown in Sec. B.2. . 47

4.2 Left: temporal profile of the pulse used in numerical simulations, measured using frequency-resolved optical gating (FROG). The amplitude is shown in solid black (left axis) and the phase is shown in dashed blue (right axis). Right: spectral profile. The amplitude is shown in solid black (left axis) and the phase is shown in dashed blue (right axis). 49

4.3 The optimal output of traditional amplifier design as shown in Fig. 4.1. The pulse is plotted in solid black as delay vs. normalized intensity, the integrated intensity is plotted in long red dashes, and the corresponding temporal phase is plotted in short blue dashes. With 350 mW of average power, this resulted in 26 kW peak power, with a duration of 70 fs FWHM and 60% of energy in main pulse. 49

4.4 Use of 65 cm of dispersion-compensating fiber (DCF) before fiber bench and 85 cm of PANDA after in order to compensate for excess DCF. With 300 mW of average power, this resulted in 31 kW of peak power, with a duration of 40 fs FWHM and 50% of energy in the main pulse. 50

4.5 Compression using large mode area (LMA) fiber. With 270 mW of average power, this resulted in 18 kW of peak power, with a duration of 80 fs FWHM and 50% of energy in the main pulse. 52

4.6 Compression using a pair of bulk silicon prisms. This resulted in a duration of 140 fs FWHM and 65% of energy in main pulse. Because compression using silicon prisms is lossy, average power and peak power were not measured. 53

4.7 Simulation of an EDFA using the measured spectrum and phase of the fiber oscillator as the input. The pulse's spectrum as a function of propagation length is plotted at left, and the pulse's temporal shape is plotted as a function of propagation length at right. The three sections of fiber are evident in the temporal plot as the dispersion flips from anomalous in PANDA (0–0.4 m) to normal in EDF (0.4–1.4 m) and back to anomalous (1.4–2.1 m). At left, nonlinear broadening is evident beyond 1.4 m as the pulse shortens and the nonlinear refractive index strongly affects the pulse's behavior. 55

4.8 Slice of spectrum and pulse at the shortest pulse duration from the simulation in Fig. 4.7, at 1.87 m. The maximum peak power was 28 kW, and the shortest pulse duration was 67 fs (measured as the full-width at half-maximum). 56

4.9 Computed spectrum of the narrower hyperbolic secant (sech) input used in modeling an alternative amplifier design. 57

4.10 Simulation of an EDFA using a hyperbolic secant (sech) pulse with 25000 fs^2 of chirp on a 50 fs pulse. The design used 30 cm of PANDA followed by 100 cm of EDF. Despite a spectrally narrower input, the resulting short pulse has a substantially broader spectrum and a shorter pulse duration than that simulated using the FROG-measured comb input. 58

4.11 Slice of spectrum and pulse using the sech input pulse from the simulation in Fig. 4.10 at the shortest pulse duration, 1.74 m. The maximum peak power was 45 kW, and the shortest pulse duration was 37 fs. 59

4.12 The experimental results using a bandpass-filtered comb output as the amplifier input. With an average power of 220 mW, the amplifier generated 50 fs pulses with 27 kW of peak power and 75% of energy in main pulse. 59

4.13 Simulation of an EDFA using the measured spectrum and phase of the fiber oscillator as the input and minimal PANDA length before the gain fiber (EDF). Only 0.1 m of PANDA was used before 1.2 m of EDF. The highest peak power occurred at 1.67 m. 60

4.14 Slice of spectrum and pulse using minimal PANDA before the EDF from Fig. 4.13 at the shortest pulse duration, at 1.67 m. The maximum peak power was 61 kW, and the shortest pulse duration was 32 fs. 61

4.15 Image of a packaged EDFA with short fiber lengths. The output of the polarization optics (bottom left) is connected via a short section of PANDA fiber to PM EDF at the splice protector (barrel-shaped component, middle). This particular amplifier uses one WDM and is pumped exclusively backwards with two pump diodes; the pump light is coupled in at a connector (labeled “980 in”). The amplifier’s output is spliced internally to highly nonlinear fiber (HNLF), the output of which is sent to a ytterbium-doped fiber amplifier from the “1060 out” port. 62

5.1 Diagram depicting the difference frequency generation process. Pump (ω_p) and signal (ω_s) photons are focused into a periodically-poled lithium niobate (PPLN) crystal, depleting the pump, generating the idler (ω_i), and creating parametric gain in the signal. 64

5.2 Schematic diagram of the MIR DFG comb and heterodyne spectroscopy setup. Boxes are connected via fiber and the color lines represent free-space beams. Lenses (not shown) are used to expand the beams and focus them into the PPLN crystal. EDFA: erbium-doped fiber amplifier, YDFA: ytterbium-doped fiber amplifier, MIR PD: mid-infrared photodetector, Ge filter: germanium window, acting as a low pass optical filter, BS: beamsplitter, PPLN: periodically-poled lithium niobate crystal, HNLF: highly nonlinear fiber. Specific part numbers are provided in Appendix B. 65

5.3 MIR power (corrected for 90 % transmission of the Ge filter) as function of pump power at 1050 nm, for a signal input power of 130 mW at 1567 nm. 67

5.4 MIR power stability plot, for PM-fiber-based MIR comb without environmental noise isolation. 67

5.5 Interferometric (black) and intensity (blue) autocorrelation traces for the MIR pulses. 68

5.6 Relative intensity noise (RIN) for the pump, signal and idler beams. RIN for the pump and signal beams has been measured before and after the PPLN crystal (under DFG). 69

5.7 MIR spectrum generated by DFG in a single PPLN grating, recorded in a high-resolution grating-based optical spectrum analyzer (RBW = 0.2 nm). Absorption lines due to atmospheric propagation in a 1.5 m path length can be seen. 70

5.8 MIR comb spectra recorded in a low-resolution FTIR spectrometer (RBW = 4 nm) for different powers, showing that the combs bandwidth was preserved at high powers. Different spectra can be obtained as the temporal overlap between the pump and signal pulses is adjusted. 70

5.9 Pump spectra measured after the PPLN crystal when both beams were present (DFG on, blue trace) and when one of them was blocked (DFG off, red trace). The red side of the pump spectrum underwent less depletion. The DFG was correspondingly less efficient on the red side of the idler spectrum. 71

5.10 Signal spectra measured after the PPLN crystal when both beams were present (DFG on, blue trace) and when one of them was blocked (DFG off, red trace). The blue side of the signal spectrum underwent less amplification. 72

5.11 Autocorrelation trace for the pump beam, measured before the PPLN crystal. The pedestal was a result of higher-order dispersion unable to be corrected using the pair of transmission gratings. 72

5.12 Autocorrelation trace for the signal beam, measured before the PPLN crystal. 73

5.13 Simulated average powers for pump (blue), signal (black) and idler (red) beams as a function of propagating distance inside the 3-mm-long PPLN crystal. 74

5.14 Absorption spectra (without subtraction of the comb spectra) of two gas cells of $^{12}C_2H_2$ and $^{13}C_2H_2$ (75 mm long, 50 Torr). Inset: zoomed region shows isotope shifts of individual lines when each gas component is measured separately. 76

5.15 Spectrum of a CH_4 cell (75 mm long, 200 Torr). 76

5.16 Average of five interferograms from heterodyning two combs, with a C_2H_2 gas cell (75 mm long, 50 Torr) in the path of one of them. The central burst corresponds to the comb pulses crossing at the detector, and is followed by revivals due to molecular free-induction decay. The x-axis is the laboratory time. 78

5.17 Fast Fourier transform of the interferogram, revealing absorption lines of the ν_3 band of $^{12}C_2H_2$. 78

6.1 Left: Overview of mid-infrared difference frequency generation using a 1.5 µm erbium fiber laser. A supercontinuum was generated and was centered about the 1.5 µm source, portions of which were used in difference frequency generation in periodically-poled lithium niobate (PPLN). The details of this procedure are described in Sec. 6.3.1. Right: Energy level diagram of the difference frequency generation process. Pump photons (ω_p) at 1 µm drive the down-conversion process, which is seeded by 1.5 µm signal photons (ω_s), leading to parametric gain in the signal and also generating idler photons (ω_i). 81

6.2 Schematic of one of the two difference frequency generation (DFG) apparatuses. An erbium fiber oscillator was split into two branches. The pump branch (top) was amplified to roughly 200 mW in an erbium-doped fiber amplifier (EDFA) before launching into highly nonlinear fiber (HNLF) to broaden the spectrum to 1 µm. This served as the seed for a ytterbium-doped fiber amplifier (YDFA), which provided 1 W of power after compression using a pair of transmission gratings. The signal branch (bottom) was also amplified to roughly 200 mW in an EDFA and launched into a HNLF of different dispersion to broaden the spectrum to 1.3 µm. The output of these two branches were combined using a dichroic beam-splitter (BS), focused into to a periodically-poled lithium niobate (PPLN) crystal. This generated idler spectra spanning 2.6–5.2 µm, the center wavelength of which was adjusted by choosing different poling periods. The generated mid-infrared light was combined with a second DFG system for dual-comb interferometry (discussed in Sec. 6.4.5), and a long-pass filter (LPF) filtered out the pump and signal beams for diagnostic purposes and to isolate the idlers, which were detected on a mercury cadmium telluride (MCT) detector. 83

6.3 Second harmonic generation autocorrelation of the 1 µm pump beam (left) and 1.3 µm signal beam (right). Delay vs. second harmonic intensity is plotted, and the autocorrelation width of each is shown adjacent to the plot. 85

6.4 Main figure: the broadened output of the EDFA used as the signal in the DFG process is shown (black, thick). This spectrum was measured using a grating-based optical spectrum analyzer (OSA). The phase-matching wavelengths for different poling periods present in the PPLN crystal for a fixed 1074 nm pump are also indicated (red, short sticks). Inset: the signal spectrum can be tailored for maximum signal power at a given poling period phase-matching wavelength by varying the pump current (original spectrum in black, thick; other spectra are thin and in color). . . . 86

6.5 The attainable spectral coverage using both 1 mm (top) and 3 mm (bottom) PPLN crystals. Spectra are scaled according to their measured integrated power. Each colored curve corresponds to a different poling period, shown in color-coded text (in microns) on the bottom plot. The gap seen near 4.2 µm results from weak power at the corresponding signal wavelength, as seen in Fig. 6.4. The longer of the two crystals has a narrower phase-matching bandwidth, and thus the spectra shown at bottom are narrower. 88

6.6 Indium antimonide (InSb) camera image of collimated 5 µm beam, with line plots above and to the right showing the integrated x- and y-axes (solid red) and Gaussian fits to each (dashed blue). 89

6.7 Optical power as a function of wavelength for 1 mm (black square) and 3 mm (red circle) PPLN crystals, plotted on a logarithmic scale. As PPLN absorption increases at longer wavelengths [56], the generated idler power decreases. 89

6.8 Simulated and observed bandwidth in 1 and 3 mm PPLN crystals. Dots signify the corrected observed full-width at half-maximum (FWHM) measurements for the two different crystal lengths. The correction divides the observed FWHMs by the convolution of the input pump and signal, which allows for the removal of the effect of the signal's spectral features. The solid lines show the simulated bandwidth of the idler, assuming a Gaussian pump and signal of durations as determined via the autocorrelations shown in Fig. 6.3. Dashed lines show the bandwidth of the input signal and the phase-matching bandwidth of a 1 mm crystal solely via ΔkL walk-off. Inset: simulated (dashed, blue) and experimental (solid, red) spectral widths for the 5.05 µm poling period. 91

6.9 Main figure: interferogram of free-running (unstabilized) 5 µm multi-heterodyne. Inset: Fourier transform, re-scaled, of unaveraged interferogram (gray) and 16 averaged interferograms (blue). 93

6.10 The relative intensity noise (RIN) of the 1 µm pump, broadened portion of the 1.5 µm signal after passing through a 1500 nm short pass filter (SPF), the generated 5 µm idler, and both the near-infrared and mid-infrared detector backgrounds. 93

7.1 Plot of the dispersion of bulk silicon in the mid-infrared. The calculated dispersion is based on the Sellmeier equation, the coefficients of which are from Ref. [57]. . . . 97

7.2 Plot of the dispersion of bulk silicon nitride in the mid-infrared. The calculated dispersion is based on the Sellmeier equation, the coefficients of which are from Ref. [48]. 97

7.3 SEM image of a 2.71 µm by 600 nm ridge waveguide design in silicon, overlaid with the simulated mode profile of the waveguide. The mode profile is visibly present in both the top cladding (air) and the bottom cladding (sapphire). 98

7.4 Diagram of the cross-section of a silicon nitride waveguide [58]. The core is comprised of silicon nitride, on a silica substrate. The core height is 2500 nm, the width varies from 1000 to 1600 nm, and the sidewall angle is 85°. The sidewalls are not a dispersion-oriented feature, but rather as a result of the Damascene process used in fabrication. 99

7.5 Design of the inversed taper in silicon nitride [58]. The tapers have a width of 560 nm, with the same waveguide height of 1900 nm. 99

7.6 SEM image of a ridge waveguide design in silicon. The waveguide width in the image is 2.5 µm, with a height of 600 nm. 100

7.7 SEM image of a sample notch waveguide design in silicon. The notch width in the image is 0.8 µm, and the notch is offset from the center of the waveguide by 0.4 µm. The notch depth is 300 nm. 101

7.8 Dispersion as a function of wavelength for TE propagation in silicon nitride for nine different waveguide widths. 102

7.9 Dispersion as a function of wavelength for TM propagation in silicon nitride for nine different waveguide widths. 102

7.10 Dispersion as a function of wavelength for ridge waveguides in silicon for four different waveguide widths. 103

7.11 SEM image of a notch waveguide design in silicon, overlaid with the mode profile of the waveguide. 104

7.12 Dispersion as a function of wavelength for notch waveguides in silicon for four different notch positions. 105

7.13 Dispersion as a function of wavelength for the two most promising waveguide designs in silicon: a ridge waveguide with a width of 3.06 µm and a notch waveguide with a notch position of 1 µm. 105

7.14 Normalized spectra for the pump and five different 20-mm-long silicon nitride waveguides, with widths ranging from 1000 to 1600 nm. An additional spectrum at the 1600 nm width was retrieved with the 3 µm source power increased by 25 %. 107

7.15 Spectra from the four ridge waveguide designs in silicon simulated in Fig. 7.10. The waveguides with lower 3 µm dispersion are able to generate spectra at longer wavelengths. 108

7.16 Spectra from the four notch waveguide designs in silicon simulated in Fig. 7.12. The wider notches, which have longer-wavelength zero crossings in Fig. 7.12, generate spectra at longer wavelengths. 108

7.17 Spectra from the two waveguide designs in silicon simulated in Fig. 7.13, along with the 3 µm pump. The notched waveguide, in yellow, spans an octave, from below 3 µm to beyond 6 µm. The ridge waveguide, in blue, is also able to generate a broad spectrum spanning nearly an octave, from 2.5 µm to nearly 5 µm. 109

7.18 The relative intensity noise (RIN) of the generated supercontinuua as compared to that of the pump and the dark detector. 109

7.19 Top: train of interferograms of the heterodyne beat between the silicon waveguide output and the long-wave DFG output at 4.8 µm. Bottom: single interferogram of the heterodyne beat, with three different averages shown. 110

7.20 Fourier transform of the heterodyne beat interferogram, overlaid with the HITRAN spectrum of carbonyl sulfide (OCS). Transforms are plotted for three different averages. While individual ro-vibrational absorptions are unable to be resolved, the broader absorption branches are well-resolved. 110

Chapter 1

Introduction and Background

1.1 Historical Background

The behavior of different colors of light has long fascinated humankind. The most prevalent and striking optical phenomenon experienced by early humans was the rainbow, which was originally attributed to a mystical and supernatural source. The first scientific approach to optics, however, was undertaken by two ancient scholars — the Greco-Roman astronomer Claudius Ptolmaeus (130 C.E.) and the Arab scientist Alhazen (1038 C.E.) — who studied the relationship between angles of incidence and angles of refraction [59]. Alhazen recognized the existence of atmospheric refraction and its effect on the apparent position of celestial bodies, but it was not until Willebrord Snell of Leyden (1591–1626) that the correspondence between the sines of the incident and refracted angles was recognized.

Snell, along with the preeminent scientists before him, did not understand the nature of colors. Even Newton's predecessor as Lucasian Professor of Mathematics at Cambridge University wrote: "Yellow is a mixture of much white and a little red...The blue color of the sea arises from the whiteness of the salt it contains, mixed with the blackness of the pure water in which the salt is dissolved [59]."

It is within this framework that Isaac Newton published **Opticks** in 1704. His experiments were rather basic; in his first paper published in **Transactions of the Royal Society** in 1671 [60], he describes placing red and blue strips of paper side by side, viewing them through a prism, and noting their different displacements. He then performed his most famous experiment: passing sunlight through a small hole and into a prism, he viewed a series of colored images of the entrance hole, which he named a “spectrum.” Newton’s discovery proved both that sunlight is a mixture of colors, and that prisms cause these colors to disperse. The field of spectroscopy advanced little in the remainder of the eighteenth century, with one key exception: the discovery in 1752 by Thomas Melvill [61] of the emission spectrum of sodium, measured using a sodium flame and a prism. It took another hundred years for this emission spectrum to be connected to matching absorption features seen in the solar spectrum.

Similar discoveries occurred with sunlight in the nineteenth century, with Wollaston in 1802 [62] reporting the observation of dark lines within the solar spectrum — now known as Fraunhofer lines — and Fraunhofer’s own detailed measurements of the roughly 700 lines seen in the solar emission spectra, the most prominent of which he named (and are still named) with letters A through H [63]. Looking at planets and other stars, he was able to discern the similarities between the solar spectra and those of planets, and also discern the differences between the sun’s spectra and that of Sirius.

It was not until 1859, by Gustav Kirchhoff, that these spectra were connected to emissions by different elements [64]. Kirchhoff also realized the relationship between absorption and emission, and was able to explain how the dark lines present in the solar spectrum matched those in sodium flame through absorption of the sun’s emission by its cooler outer atmosphere. Kirchhoff, with the assistance of Robert Bunsen, then set out to characterize the makeup of the sun’s atmosphere, and also discovered a number of elements, including rubidium and cesium [65]. This laid the foundation for modern spectroscopy [66].

1.2 The Need for Sensitive, Broadband Sources for Molecular Spectroscopy

In order for Kirchhoff to make his measurements of sodium absorption from the sun, he depended on the broadband nature of the sun’s spectrum: a source that extends beyond the spectral range of the absorption feature being studied such that the absorption features can be distinguished. Modern-day tunable diode laser technology accomplishes this objective; these are able to tune across atomic resonances quite readily, and can do so both rapidly and accurately. The coherence properties of lasers are such that their frequency can be compared to a standard, and thus the spectral position of detected absorption features can determined to a high precision. However, as diode lasers have a limited tuning range, they do not have the ability to span the wide wavelength ranges present in molecular spectra.

In addition to the challenge of maintaining accuracy while extending measurement bandwidth, there are additional challenges that arise in the broad-bandwidth detection within molecular spectroscopy. These include sensitivity, quantification, and discrimination. Sensitive measurements entail detection of part-per-billion or part-per-trillion [67] concentrations. The minimum detection limit is determined by both the measurement signal-to-noise ratio (SNR) and the species being detected. For perspective, one part-per-billion is equivalent to one drop of water diluted down amongst 250 chemical drums, and one part-per-trillion corresponds to one drop of water, diluted down amongst 400 Olympic-sized swimming pools. Quantification describes a high degree of precision and accuracy, and needs a model with which to fit the data, also using knowledge of the background. Discrimination involves the identification of a target species in a crowded spectral window, and requires the combination of broad bandwidth, high resolution, and an accurate model to correctly and precisely identify trace gas concentrations when the identifying features are buried beneath the absorption features of ambient gases in the raw data.

Thus, precision molecular spectroscopy requires a combination of the precision and coherence of a laser, but the broad bandwidth provided by white-light sources.

1.3 Optical Frequency Combs

The optical frequency comb is a perfect tool for this challenge; frequency combs allow for rapid measurement, broad bandwidth, and good spectral discrimination. An optical frequency comb is essentially the combination of 10^6 continuous-wave lasers, and as such can provide an absolute frequency reference like a continuous-wave laser can provide, and also has the stability native to lasers. Each of a comb's "teeth" are separated in the frequency domain from its neighbor

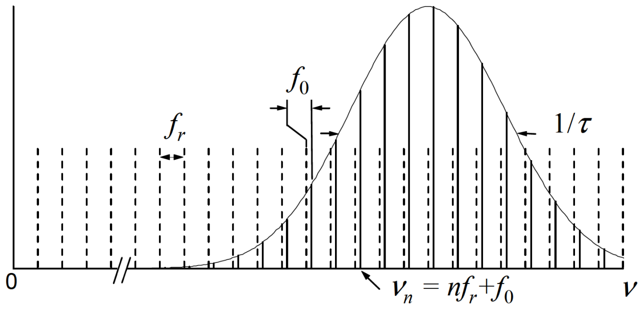

Figure 1.1: Representation of a frequency comb, plotted as power vs. frequency (ν). The vertical dashed lines show the spacing f_r (or f_{rep}) between neighboring comb modes counting from zero, and the solid vertical lines show the location of the comb modes in frequency space, offset from the dashed lines by the offset frequency f_0. Any given comb mode ν_n (or f_n) is therefore defined as $nf_r + f_0$. The solid curve shows comb's bandwidth in the frequency domain; it corresponds to the inverse of the pulse duration $\frac{1}{\tau}$ [1].

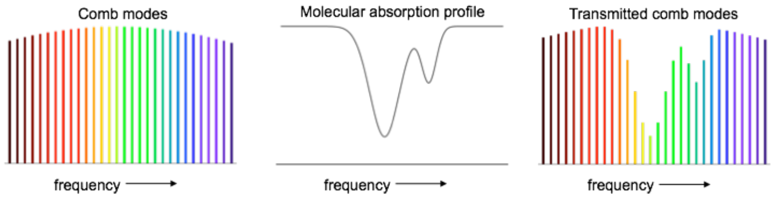

Figure 1.2: A cartoon of a frequency comb (left) passing through a molecular absorption feature (middle) leaves the molecular imprint on the transmitted comb modes (right).

by the repetition rate of the laser, f_{rep}; its absolute frequency is defined as:

$$f_n = nf_{\text{rep}} + f_0, \tag{1.1}$$

where f_0 (the offset frequency, also often referred to as f_{ceo}, the carrier-envelope offset frequency) defines how the comb is offset from zero. (See Fig. 1.1 for a visual representation.)

In a spectroscopic application, the absorption fingerprint is simply “imprinted” on the comb lines, and the absorption feature can readily be recovered (see Fig. 1.2). Frequency comb spectroscopy has grown to be a sizable field since the first demonstration of broadband, high-resolution detection of molecular iodine in 2007 [68]. These first measurements were done using a titanium-doped sapphire (Ti:S) mode-locked laser, and since then, both the Ti:S laser and a near-infrared laser, the erbium-doped fiber laser, have become commercially available frequency comb technology and have been implemented in countless spectroscopy experiments.

1.4 Frequency Comb Spectroscopy

Frequency combs have been implemented in spectroscopic applications across a wide range of fields, both at NIST and elsewhere. In the near-infrared, frequency combs have been implemented in industrial applications [69] to determine concentrations of impurities, and in human breath analysis [70, 71] to identify biomarkers indicative of various diseases. For example, abnormal levels of carbon monoxide (CO) can indicate oxidative stress, respiratory infection, or anemia, and abnormal levels of nitric oxide (NO) can be markers of asthma, hypertension, rhinitis, and lung disease.

Another application that has been pursued heavily at NIST is the detection and quantification of greenhouse gases. Here, frequency combs centered near 1.5 µm [72] have been successfully transmitted and collected outdoors over a 2 km path and spectroscopy was performed on several species simultaneously, including carbon dioxide, methane, and water vapor [73]. In the lab, an erbium fiber-based system was broadened to 2 µm [74] to perform spectroscopy on a more sensitive absorption feature in carbon dioxide, and to demonstrate accurate measurements of temperature as a function of absorption in temperature-dependent absorption bands in that molecule [75, 76].

1.5 Reaching the Mid-Infrared and Other Applications

However, absorption spectroscopy is far more powerful in the mid-infrared spectral region. Traditionally, mid-infrared laser sources have been based on continuous wave (CW) gas and diode lasers [77–79], but the development of frequency combs in this spectral region has drastically expanded measurement capabilities. Small molecules such as carbon dioxide have fundamental rotational-vibrational absorption bands at these wavelengths, which allow for such sensitive measurements as time-resolved spectroscopy [80, 81], airborne spectroscopy [82, 83], and trace gas sensing [84]. Larger molecules also begin to exhibit absorption features at these wavelengths, including many species of interest such as chemical warfare agents (see Fig. 1.3) and explosives

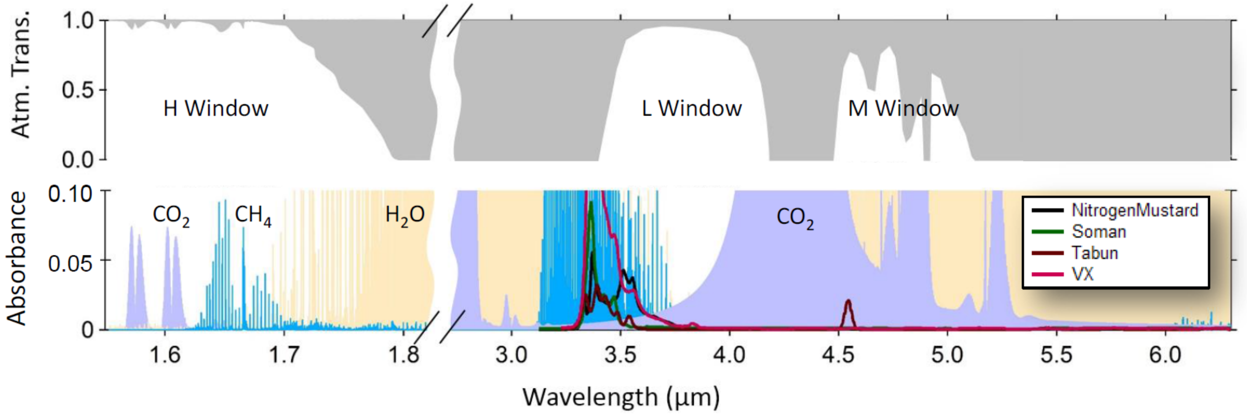

Figure 1.3: Top: atmospheric water vapor windows over a 1 km path. Bottom: background absorbance from CO_2 (purple), CH_4 (cyan), and H_2O (tan), in addition to chemical warfare agents, shown at 1 ppb concentration over 1 km, multiplied by 100 for clarity [2].

[34, 38, 85–92].

It should be noted that the applications of mid-infrared frequency combs are not limited to spectroscopy. These are depicted in Fig. 1.4. One prominent application is in high harmonic generation (HHG), a process in which an intense laser pulse impinges upon a target (often a gas or plasma) and coherent harmonics of the pump frequency are generated. Mid-infrared frequency combs prove useful for this process, as the shortest wavelength generated is proportional to the square of the driving wavelength [93]. Mid-infrared frequency combs provide the seed for amplified high-peak-power mid-infrared sources ranging from between 2 µm [94] to 3.9 µm [95] which are implemented to extend the photon energy of generated X-rays beyond 100 eV and into the 1 keV range.

Scattering scanning near-field microscopy (s-SNOM) is another application for mid-infrared femtosecond lasers. This is an imaging technique that allows for nanoscale spatial resolution, beating the wavelength-dependent diffraction limit characteristic of traditional microscopy techniques. s-SNOM requires low-noise, bright, spectrally broad sources [96, 97]. Laser-based supercontinua and infrared beamlines have been implemented as broadband, coherent sources for s-SNOM; however, a tunable, femtosecond source is ideal for combining bandwidth coverage and high spectral irradiance with low average power to avoid sample heating and damage.

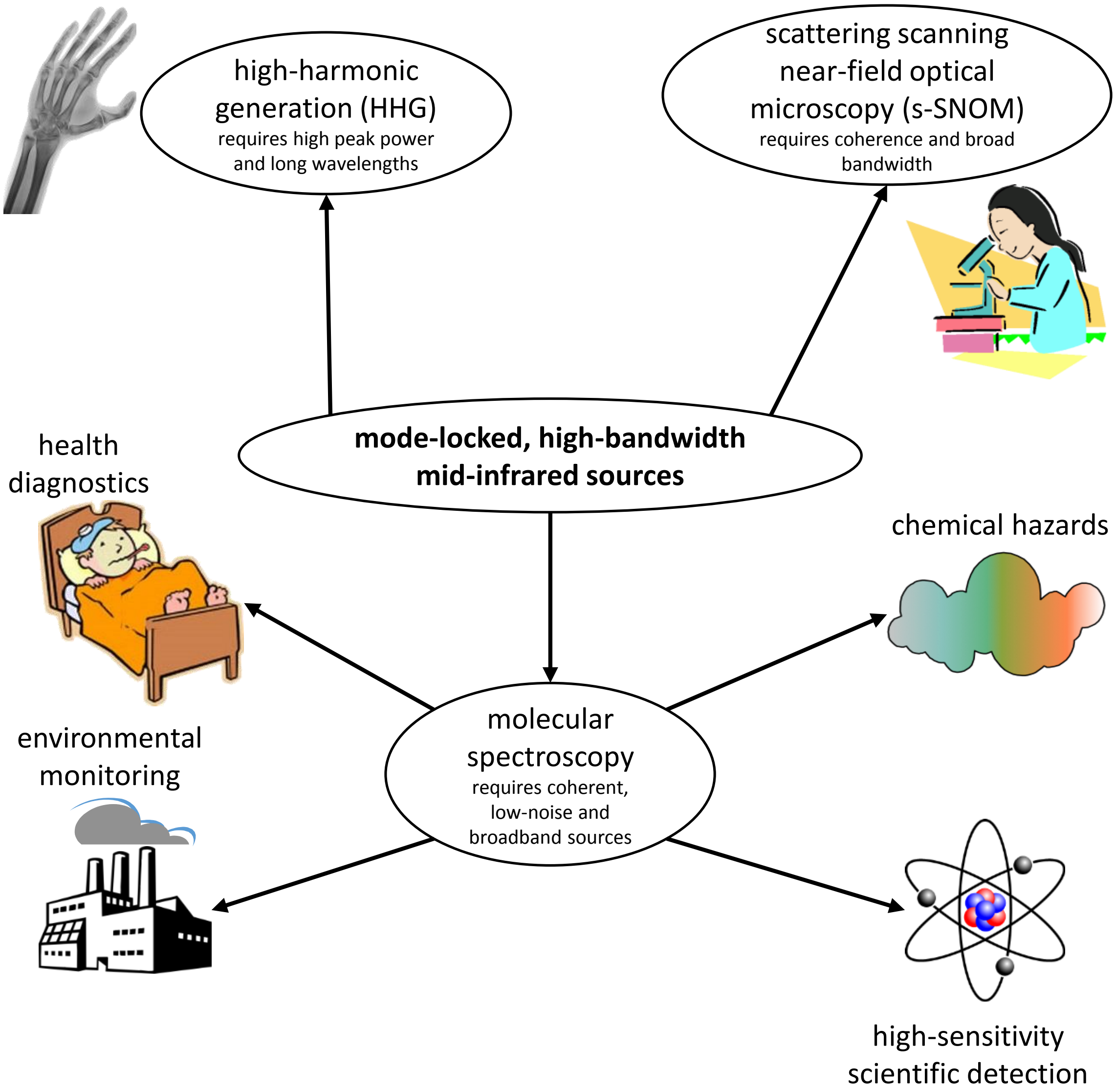
high-harmonic generation (HHG)
requires high peak power and long wavelengths
scattering scanning near-field optical microscopy (s-SNOM)
requires coherence and broad bandwidth
mode-locked, high-bandwidth mid-infrared sources
health diagnostics
chemical hazards
molecular spectroscopy
requires coherent, low-noise and broadband sources
environmental monitoring
high-sensitivity scientific detection

Figure 1.4: Cartoon showing applications of mid-infrared sources. Spectroscopic applications of mid-infrared sources include medicine, industry, security and defense, and pure science, enabled by greater sensitivity. Outside of spectroscopy, mid-infrared sources can be implemented in high-harmonic generation, in order to produce higher-energy X-rays, and in optical microscopy, taking advantage of the spectral capabilities of mid-infrared sources while beating their traditional diffraction limit.

The metrological potential of frequency combs has been implemented at mid-infrared wavelengths, as well. Mid-infrared sources allow chemists to probe the nature of molecular chirality — the “handedness of a molecule” — and investigate if the left- and right-handed versions of a molecule (enantiomers, or optical isomers) exhibit a slight shift in their absorption features. Theory predicts a small variation as a result of weak force, which can violate parity. One of the lightest chiral molecules, bromochlorofluoromethane (CHFClBr), can be examined closely in the 10 µm region to look for this spectral change [98].

An additional application that requires a similarly high degree of sensitivity is the measurement of isotopologue concentrations, which is implemented in carbon dating and carbon source determination [99]. Ref. [67] describes the success of comb-assisted cavity ringdown spectroscopy in the detection of trace concentrations of radiocarbon-dioxide ($^{14}C^{16}O_2$), at parts-per-quadrillion levels. Here, measurements are performed at the 4.5 µm absorption feature of carbon dioxide, and the mid-infrared detection source used is locked to a frequency comb. This technique is able to distinguish between depleted, enriched, and present-day levels of ^{14}C, and has immense potential in supplanting the more established technique of accelerator mass spectroscopy for dating biological samples from the past 50,000 years.

Generating mid-infrared frequency combs for these applications is far from trivial, however. The most common methods of frequency comb development occur in either the near-infrared or visible spectral regions: titanium-doped sapphire lasers, erbium-doped fiber lasers, and ytterbium-doped fiber lasers. Fiber laser technology becomes increasingly more limited at wavelengths longer than 2 µm. Fiber-based lasers typically depend on fused silica glass (the basis for optical fiber telecommunication), which begins to exhibit strong absorption at wavelengths longer than 2 µm as a result of tails of absorption bands in the far-infrared and impurities, such as hydroxyl ions from water, introducing absorption features. To amplify light, glass is doped with a variety of different elements, which can be pumped and used to create gain at a seeded wavelength. There are four common dopants used to realize gain in silica fiber: ytterbium (Yb) can produce gain near 1050 nm, erbium (Er) can produce gain near 1560 nm, thulium (Tm) can produce gain near 1950 nm, and holmium (Ho) can produce gain near 2000 nm. These elements can provide gain at longer wavelengths, but a more transmissive glass is required in order to support light generation in this wavelength region. For example, in fluoride fiber, erbium ions provide lasing at 2.75 µm and holmium ions provide lasing at 2.85 µm [41].

This thesis describes the use of free-space nonlinear down-conversion (through either optical parametric oscillation or difference frequency generation) pumped by near-infrared fiber sources, the physics of which is described in greater detail in Chapter 2. The near-infrared fiber sources are based upon robust and technologically mature erbium-doped fiber oscillators centered at 1.5 µm [72, 100]. Erbium-doped fiber amplifiers (EDFAs) boost the power of these combs in order to drive four-wave mixing in fiber, which can extend the spectrum from 1 to 2 µm [101, 102]. Here, Yb amplifiers (at 1 µm) or Tm amplifiers (at 2 µm) can boost the power in these spectral regions further in order to drive three-wave mixing in free space. Using these methods, mid-infrared light has been generated between 3–5 µm using an optical parametric oscillator pumped at 2 µm [52], at 3 µm using difference frequency generation of 1 and 1.5 µm light [51, 103], and between 3–5 µm using difference frequency generation of 1 and 1.3–1.5 µm light [104].

1.6 Alternate Methods to Generate Mid-Infrared Radiation

There are many other techniques used in addition to three-wave mixing of near-infrared sources in order to generate broadband light for precision spectroscopy. The method that most naturally extends from the popular near-infrared fiber-based techniques is the use of an infrared-transmissive glass, such as fluoride or chalcogenide. Dopants such as erbium and holmium can provide gain in fluoride where it was not possible in silica-based fiber systems [41, 105]. Near-infrared sources can be shifted to longer wavelengths and broadened in fluoride fiber [106] or chalcogenide [107], or, alternatively, a fluoride-based system can use chalcogenide for broadening [108]. Other fiber-based techniques can implement chromium-doped zinc sulfide (Cr:ZnS) to produce mode-locked mid-infrared light at 2.4 µm [109]. Gas-filled hollow-core photonic crystal fiber can lase in the mid-infrared, as well [110].

The more popular method for generating broadband mid-infrared light for spectroscopy uses either quantum cascade lasers (QCLs) or interband cascade lasers (ICLs) [36, 39, 40, 111–114], which are tunable, continuous-wave mid-infrared sources that have emerged in the last twenty years. Frequency combs are generated from these continuous-wave sources through cascaded four-wave

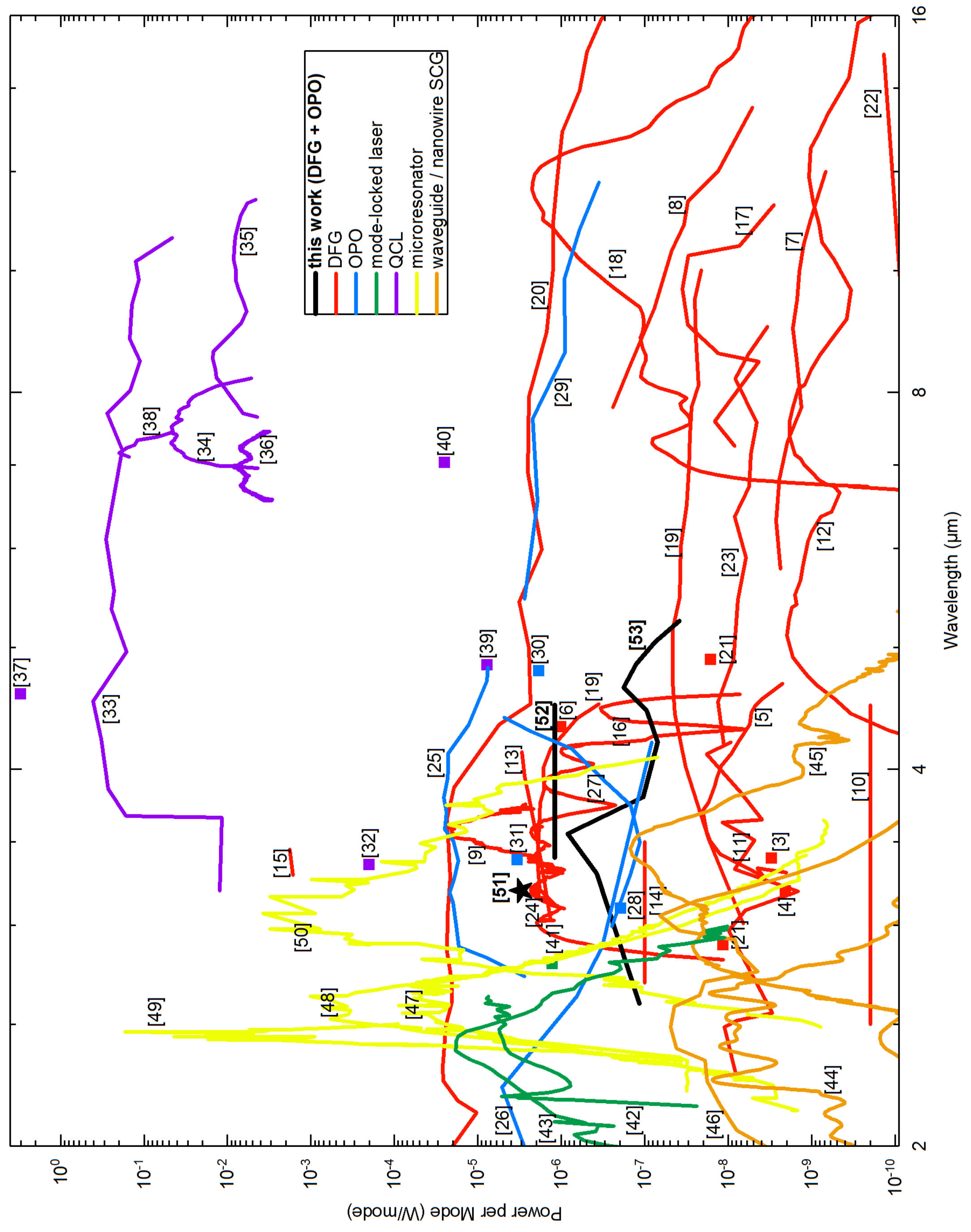

Figure 1.5: A summary of related literature regarding mid-infrared mode-locked lasers and quantum cascade lasers. Difference frequency generation (DFG) sources [3–24], optical parametric oscillators (OPOs) [25–31], quantum cascade lasers (QCLs) [32–40], mode-locked lasers [41–43], supercontinuum sources [44–46], microresonators [47–50], and the work discussed in this thesis [51–53] are plotted as power per mode vs. wavelength.

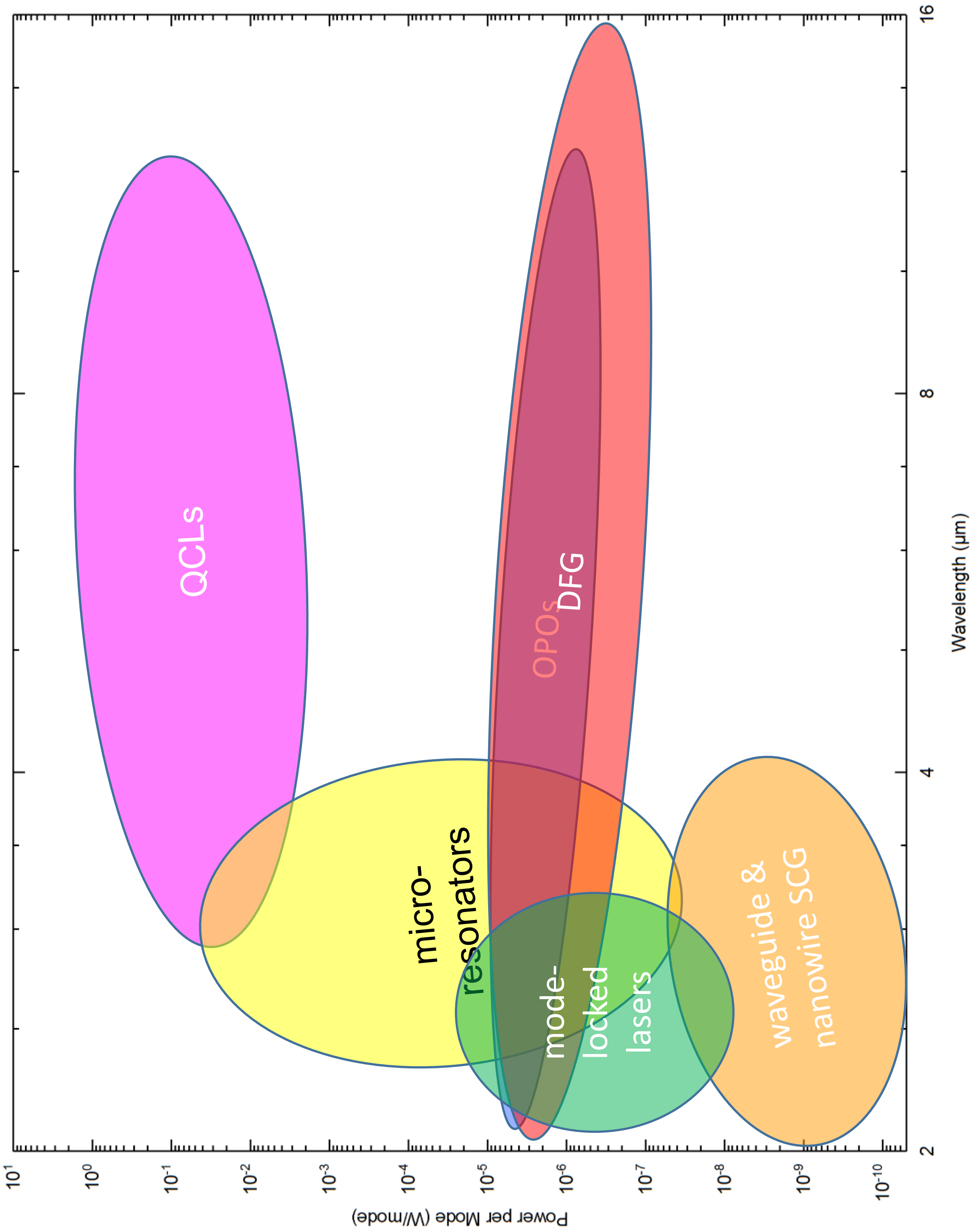

Figure 1.6: Simplified summary of the various mid-infrared generation techniques from Fig. 1.5. Many other mid-infrared sources (microresonators, mode-locked lasers, and supercontinuum generation) are unable to generate light beyond 4 µm. Quantum cascade lasers (QCLs) generate high power but with narrow bandwidth and limited tunability. Difference frequency generation (DFG) and optical parametric oscillators (OPOs) support widespread spectral coverage and broad instantaneous bandwidth.

mixing in microresonators or waveguides, fashioned out of materials more suited for mid-infrared transmission, such as chalcogenide [115], silicon [44, 47, 50], and silicon nitride [48].

The various methods of mid-infrared generation described above are summarized in Fig. 1.5. These are plotted as power per mode versus wavelength, and are synthesized into a cartoon in Fig. 1.6. As can be seen in the Figure, many of these other techniques for generating coherent mid-infrared radiation are unable to generate light beyond 4 µm. While QCLs can achieve high powers per mode and the spectral coverage of DFG and OPOs, the instantaneous bandwidth is substantially more narrow than other techniques, and only limited spectral tunability can be achieved in a single device. Thus, the two techniques explored in this thesis — difference frequency generation and optical parametric oscillation — are the most promising techniques by which broadband mid-infrared molecular spectroscopy can be achieved.

1.7 Dual Comb Spectroscopy and Other Measurement Techniques

Secs. 1.5 and 1.6 review some of the other techniques used to generate mid-infrared radiation. This section discusses a few of the measurement methods in spectroscopy, and will highlight the ones featured in this thesis. Fig. 1.7 gives a top-level perspective of the entire spectroscopy process: at left, the electromagnetic radiation sources; at center, the detection media; and at right, the measurement method. The spectroscopy described in Chapters 5 and 7 was conducted with simple, single-pass cells filled with the desired gas species.

For detection, the Fourier-transform spectrometer (FTS) is an effective tool for measuring infrared wavelengths. An FTS separates a beam with a beam-splitter and recombines them after reflecting off of one fixed and one moving arm, where intensity is measured at a detector as a function of mirror position, called an interferogram. The Fourier transform of this interferogram produces the incident optical spectrum. The resolution of an FTS depends upon the arm length of the Michelson interferometer it uses; in order for an FTS to be able to resolve the individual comb modes of a 100 MHz comb, the interferometer arms need to be 3 m long. A second effective spectroscopic technique is the virtually-imaged phased array, or VIPA. A VIPA essentially is a

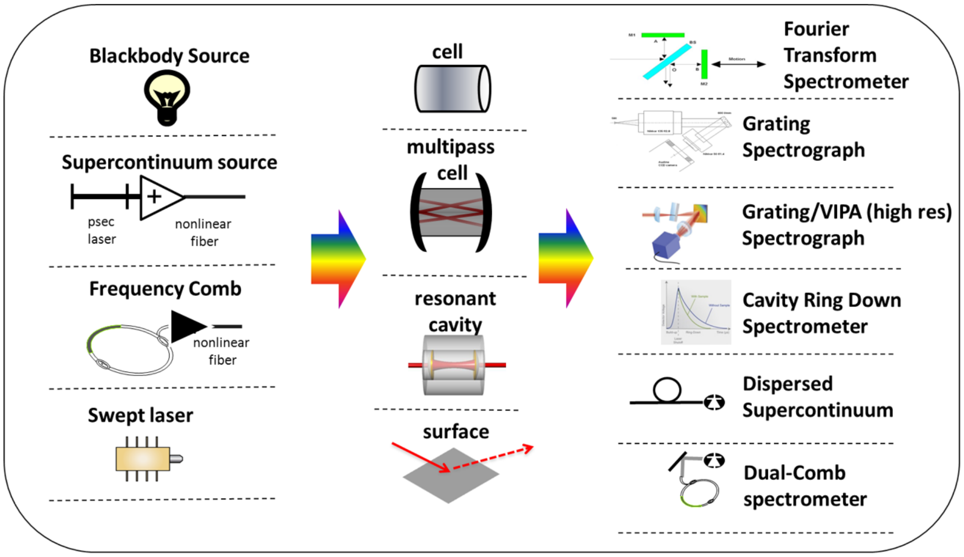
Blackbody Source
Supercontinuum source
psec laser
nonlinear fiber
Frequency Comb
nonlinear fiber
Swept laser
cell
multipass cell
resonant cavity
surface
Fourier Transform Spectrometer
Grating Spectrograph
Grating/VIPA (high res) Spectrograph
Cavity Ring Down Spectrometer
Dispersed Supercontinuum
Dual-Comb spectrometer

Figure 1.7: Survey of electromagnetic radiation sources, detection media, and measurement techniques. The left panel summarizes four sources that can cover molecular absorption features: incoherent blackbody sources, picosecond supercontinuum sources broadened with nonlinear fiber, frequency combs, and tunable single-frequency lasers. These can be implemented in several ways in order to perform a spectroscopic measurement, such as passing once through a gas cell, passing tens to hundreds of times through a multipass cell, passing orders of magnitude more times through a resonant cavity, and scattering off of a surface. Lastly, the spectroscopic signal can be detected through a variety of methods, such as the traditional Fourier-transform spectrometer, a spatially-separated grating spectrograph, a high-resolution spectrograph called a VIPA (virtually-imaged phased array), a lifetime measurement using a cavity ring-down spectrometer, a rapid time-domain measurement using a dispersed supercontinuum, and lastly, a dual-comb spectrometer.

strongly dispersive etalon, and, combined with a weakly dispersive diffraction grating, can separate incident frequency comb modes in a two-dimensional array. However, VIPA spectroscopy is limited to GHz resolution, and requires an array detector, such as a camera. A VIPA has no moving parts, performs rapid and parallel detection, and has proven successful for frequency comb spectroscopy [69, 74, 75, 116, 117].

Dual comb spectroscopy behaves much like a Fourier-transform spectrometer, but without the moving arms characteristic of the Michelson interferometer. Two mode-locked lasers with slightly different repetition rates (f_r and $f_\mathrm{r} + \Delta$) are combined and are sensed by a detector. In the time domain, this can be considered as two pulses hitting the detector simultaneously at $t = 0$, generating an interferogram, and subsequently walking off until time $t = \frac{1}{\Delta}$ when a second interferogram is

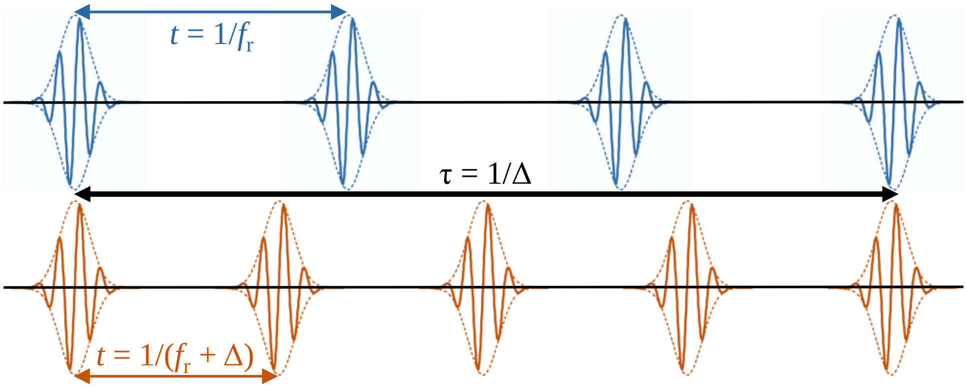

Figure 1.8: Time domain representation of dual comb spectroscopy. Two frequency combs, of repetition rates f_r and $f_r + \Delta$, interfere when combined and sensed by a detector when pulses arrive simultaneously. This first occurs at $t = 0$, then subsequently at time $t = 1/\Delta$, when the pulse-to-pulse walk-off fully "wraps around."

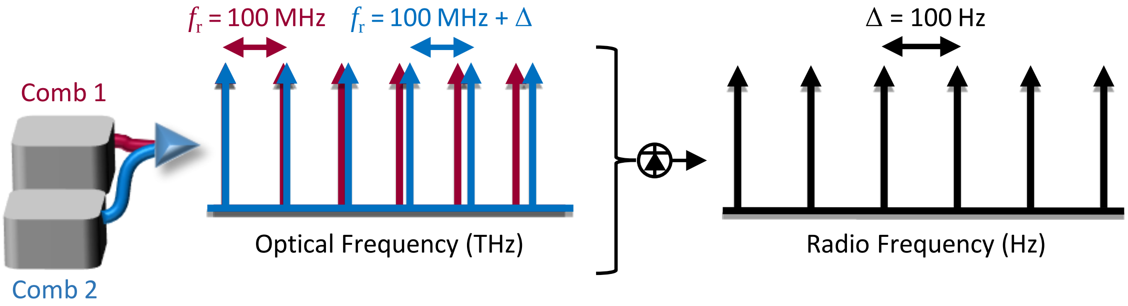

Figure 1.9: Frequency domain representation of dual comb spectroscopy. Two frequency combs, of repetition rates f_r and $f_r + \Delta$, are combined and sensed by a detector, seen at left. The beats between the modes of the two combs generate a frequency comb in the RF with a mode spacing of Δ, shown at right.

generated, as shown in Fig. 1.8. Dual comb spectroscopy can achieve the 100 MHz resolution possible with an FTS, but has no moving parts like the VIPA. While it requires a duplicate mid-infrared source to perform a measurement, the detection instrument required is simply a high-speed photodetector, and can therefore be substantially easier and less expensive to use, without any distortions or transfer functions introduced by the camera and the VIPA etalon.

Dual comb spectroscopy can also be visualized in the frequency domain, shown in Fig. 1.9. Two frequency combs, of repetition rates f_r and $f_r + \Delta$, will generate a series of heterodyne beats that uniquely map the optical spectrum to the radio frequency domain. The first comb mode of one will generate a beat with the first comb mode of the other at the radio frequency Δ. The second will similarly generate a beat with the second of the other at 2Δ, and so forth, until the n^{th} mode of one will beat with the n^{th} mode of the other at $n\Delta$. This generates a radio frequency comb of beats with a mode spacing of Δ. The radio frequency comb is a convolution of the two input frequency combs, and as such, the amplitudes of each beat reflects the amplitude of the comb modes generating the beat. (Similarly, the relative phase between the two combs can be measured, so the phase response of a sample can be determined if only one of the two combs passes through a sample.) This is how absorption features are detected; one or both of the frequency combs passes through a sample, and the molecular absorptions are imprinted on the radio frequency comb. The resulting radio frequency comb can then be scaled back into the optical domain using the values of Δ and f_{r}. This technique is implemented for spectroscopy in Chapters 5, 6, and 7.

1.8 Thesis Outline

Chapter 2 will outline the physical basis for three- and four-wave mixing, the processes behind the erbium-doped fiber amplifiers used in source development and the nonlinear down-conversion that generates mid-infrared light. Chapter 3 will describe an optical parametric oscillator used to generate light ranging from 3–5 μm, pumped using a thulium amplifier at 2 μm. Chapter 4 will detail the development of more robust source technology in the near-infrared to drive these nonlinear processes. Chapter 5 will discuss using these more stable near-infrared sources to make a reliable mid-infrared source at 3 μm using difference frequency generation to generate high powers and perform some basic spectroscopic measurements. Chapter 6 will examine extending the difference frequency generation output to longer wavelengths: through broadening of one of the branches of the near-infrared sources. Chapter 7 will summarize using the DFG source from Chapter 5 to pump chip-scale waveguides.

Chapter 2

Theory of Three- and Four-Wave Mixing

2.1 Introduction

Much of the work described in this thesis involves the process of nonlinear optical mixing, either in optical fiber (four-wave mixing) or in free space in a nonlinear crystal (three-wave mixing). The chapter will describe both of these processes. The basis of this nonlinear response comes from the interaction between an electric field, $\tilde{E}(t)$, and a material. The objective here is to demonstrate that the physical processes featured in this thesis originate from the classical descriptions of the interactions between light and matter, and can be explained in a straightforward manner with a couple of reasonable approximations. Much of the derivations presented here follow those from Ref. [118].

Next, computer simulations were then developed based on the theory described here. The initial effort for developing both simulations was performed with substantial assistance from Gabe Ycas, based off of Ref. [119] for $\chi^{(2)}$ processes and MATLAB code from Ref. [120] for $\chi^{(3)}$ processes. A Python package, entitled PyNLO, was published by Dr. Ycas for a fully-developed model, with both $\chi^{(2)}$ and $\chi^{(3)}$ processes, and is available for general use at `github.com/pyNLO`. The test cases discussed are included in the package, as well.

The dipole moment per unit volume (polarization) is given by $\tilde{P}(t)$, which, in linear optics, is linearly dependent on the electric field strength:

$$\tilde{P}(t) = \epsilon_0 \chi^{(1)} \tilde{E}(t), \tag{2.1}$$

where $\chi^{(1)}$ is the linear susceptibility, and ϵ_0 is the familiar permittivity of free space, and the tilde indicates that the corresponding variable changes rapidly with time. In nonlinear optics, $\tilde{P}(t)$ can be generalized to a power series:

$$\begin{aligned}\tilde{P}(t) &= \epsilon_0 \left(\chi^{(1)}\tilde{E}(t) + \chi^{(2)}\tilde{E}^2(t) + \chi^{(3)}\tilde{E}^3(t) + \dots\right) \\ &= \tilde{P}^{(1)}(t) + \tilde{P}^{(2)}(t) + \tilde{P}^{(3)}(t) + \dots\end{aligned} \tag{2.2}$$

where $\chi^{(2)}$ and $\chi^{(3)}$ are the second- and third-order nonlinear optical susceptibilities, and $\tilde{P}^{(2)}(t)$ and $\tilde{P}^{(3)}(t)$ are the second- and third-order nonlinear polarizations. In solids, these susceptibilities are typically on the order of [118]:

$$\begin{aligned}&\chi^{(1)} \sim 1, \\ &\chi^{(2)} \sim 10^{-12}\text{m/V}, \text{ and} \\ &\chi^{(3)} \sim 10^{-24}\text{m}^2/\text{V}^2.\end{aligned} \tag{2.3}$$

Based on the field strengths typical of the remainder of this thesis, only the lowest-order nonlinear susceptibility is incorporated; that is, for three-wave mixing, only terms up to the $\chi^{(2)}$ term need to be considered, and for four-wave mixing, only terms up to the $\chi^{(3)}$ term need to be considered.

2.2 Microscopic Nature of Nonlinear Susceptibility

Not all materials exhibit a second-order susceptibility ($\chi^{(2)}$). In materials where $\chi^{(2)} = 0$, the dominant nonlinear effect comes from the third-order susceptibility ($\chi^{(3)}$). The property that determines this is inversion symmetry [121]. In a point group with an inversion center (also known as centrosymmetry), the point (x, y, z) is indistinguishable from the point $(-x, -y, -z)$ (see Fig. 2.1). Media without inversion symmetry can exhibit second-order nonlinearity. The second-order susceptibility leads to an even-order harmonic (such as second-harmonic generation) which creates an asymmetric electric field dependence. This can only occur if the material itself lacks inversion symmetry. Some materials featured in this thesis possess inversion symmetry, while others do not;

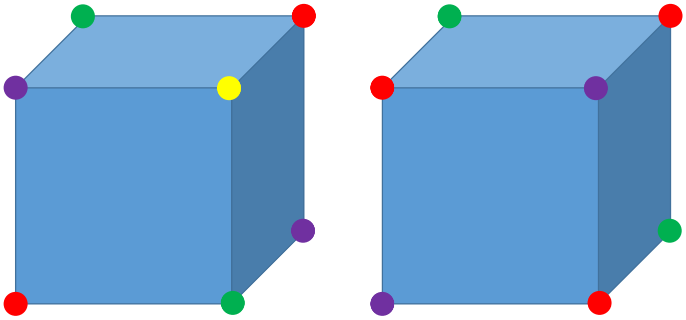

Figure 2.1: Diagram demonstrating inversion symmetry. The cube at left exhibits inversion symmetry; each corner matches the color of that when each its coordinate's positions are inverted. The cube at right does not exhibit inversion symmetry; each corner matches the color when two of its coordinates are inverted, but not when all three are.

silicon, silicon nitride, and silica are centrosymmetric, whereas lithium niobate and silver gallium selenide are not.

According to the Lorentz model, the response of a medium to electromagnetic waves is treated as a harmonic oscillator [118, 121]. This model of an atom as a driven, damped oscillator is expressed as

$$m\frac{\mathrm{d}^2x}{\mathrm{d}t^2} + m\gamma\frac{\mathrm{d}x}{\mathrm{d}t} + m\omega_0^2 x = -e\mathcal{E}, \tag{2.4}$$

where m is the electron mass, γ is the damping coefficient, ω_0 is the resonant frequency of the atom due to bound electrons, e is the magnitude of the electric charge of the electron, and $\mathcal{E}$ is the electric field of the incident light wave. In Eq. 2.4, each term is in units of force, where $U(x) = \frac{1}{2}m\omega_0^2x^2$ is the traditional potential energy of the harmonic oscillator described. If the material is not centrosymmetric, this potential becomes asymmetric, and can be approximated as an anharmonic oscillator:

$$U(x) = \frac{1}{2}m\omega_0^2x^2 + \frac{1}{3}m_0C_3x^3 + \ldots, \tag{2.5}$$

where the corresponding force is

$$F(x) = \frac{\mathrm{d}U}{\mathrm{d}x} = -(m\omega_0^2x + m\alpha x^2), \tag{2.6}$$

and α is an undetermined constant. Here it can be seen that the restoring force now contains a term proportional to the square of the displacement. Such a “nonlinear” restoring force in a real material leads to the optical properties described in this chapter.

Incorporating this sign-dependent restorative force into the differential equation, Eq. 2.4 becomes:

$$m\frac{\mathrm{d}^2x}{\mathrm{d}t^2}+m\gamma\frac{\mathrm{d}x}{\mathrm{d}t}+m\omega_0^2x+m\alpha x^2=-e\mathcal{E}. \tag{2.7}$$

If the driving wave is assumed to be the superposition of two single frequencies:

$$\mathcal{E}(t)=\mathcal{E}_1\cos\omega_1 t+\mathcal{E}_2\cos\omega_2 t, \tag{2.8}$$

then Eq. 2.7 can be solved using a perturbation expansion, following the method detailed in Ref. [118]. The electric field is characterized by the parameter λ which is between zero and one, so, after dividing by m, the differential equation becomes

$$\frac{\mathrm{d}^2x}{\mathrm{d}t^2}+2\gamma\frac{\mathrm{d}x}{\mathrm{d}t}+\omega_0^2x+\alpha x^2=-\frac{\lambda e\mathcal{E}}{m}. \tag{2.9}$$

x can be expressed as a power series in the strength of the perturbation, λ:

$$x=\lambda x^{(1)}+\lambda^2x^{(2)}+\dots \tag{2.10}$$

the solutions of which can be separated into powers of λ. Here, the $x^{(1)}$ term leads to the equation for terms linear in λ:

$$\frac{\mathrm{d}^2x^{(1)}}{\mathrm{d}t^2}+2\gamma\frac{\mathrm{d}x^{(1)}}{\mathrm{d}t}+\omega_0^2x^{(1)}=-\frac{\lambda e\mathcal{E}}{m}, \tag{2.11}$$

which generates the traditional Lorentz dipole solution:

$$x^{(1)}(t)=a_1e^{-i\omega_1 t}+a_2e^{-i\omega_2 t}+\text{c.c.}, \tag{2.12}$$

where c.c. denotes the complex conjugate of terms equal in magnitude and frequency.

The second-order term in λ from Eq. 2.10 includes both $x^{(2)}$ terms and an $x^{(1)}$ term:

$$\frac{\mathrm{d}^2x^{(2)}}{\mathrm{d}t^2}+2\gamma\frac{\mathrm{d}x^{(2)}}{\mathrm{d}t}+\omega_0^2x^{(2)}+\alpha\left[x^{(1)}\right]^2=0. \tag{2.13}$$

Thus, the possible generated frequencies are simply the frequencies found in the square of the $x^{(1)}$ term: $2\omega_1$, $2\omega_2$, $\omega_1+\omega_2$, $|\omega_1-\omega_2|$, and 0 (DC).

In media with the requisite symmetry, this asymmetric potential does not exist, and the next possible higher-order term in the restoring force is a cubic term [118]:

$$F = -m\omega_0^2 x + mbx^3 \tag{2.14}$$

and the corresponding potential energy is given by

$$U = \int F \mathrm{d}x = \frac{1}{2} m\omega_0^2 x^2 - \frac{1}{4} mbx^4. \tag{2.15}$$

b is usually (but not always) positive, meaning that this restoring force is usually dampened at larger x. Eq. 2.15 can be solved in a similar manner to the second-order case above, and is again outlined more thoroughly in Ref. [118]. Similarly to how the solution to Eq. 2.13 includes terms of $\mathcal{E}^2$ and thus incorporates the second-order polarization, this solution includes terms of order $\mathcal{E}^3$ and must incorporate the third-order polarization, and therefore $\chi^{(3)}$. A positive b yields a positive $\chi^{(3)}$, which induces the typical positive nonlinear refractive index n_2. However, b can, in some materials, be negative. The presence of $\chi^{(2)}$ and $\chi^{(3)}$ terms are motivated further in the subsequent sections through a derivation based on Maxwell's equations.

2.3 $\chi^{(2)}$ Processes and Three-Wave Mixing

The combination of two electric fields, one of electric field strength E_1 oscillating at ω_1 and the other of electric field strength E_2 oscillating at ω_2, can be expressed as

$$\tilde{E}(t) = E_1 \mathrm{e}^{-i\omega_1 t} + E_1^* \mathrm{e}^{i\omega_1 t} + E_2 \mathrm{e}^{-i\omega_2 t} + E_2^* \mathrm{e}^{i\omega_2 t}. \tag{2.16}$$

The two fields induce a second-order nonlinear polarization, from 2.2, of

$$\begin{aligned} \tilde{P}^{(2)}(t) = \epsilon_0 \chi^{(2)} (&E_1^2 \mathrm{e}^{-2i\omega_1 t} + E_2^2 \mathrm{e}^{-2i\omega_2 t} + 2E_1 E_2 \mathrm{e}^{-i(\omega_1+\omega_2)t} \\ &+ 2E_1 E_2^* \mathrm{e}^{-i(\omega_1-\omega_2)t} + \mathrm{c.c.}) + 2\epsilon_0 \chi^{(2)} (E_1 E_1^* + E_2 E_2^*). \end{aligned} \tag{2.17}$$

The combinations created here all describe familiar nonlinear optical processes:

$$P(2\omega_1) = \epsilon_0\chi^{(2)}E_1^2 \text{ (second harmonic generation)}, \tag{2.18}$$

$$P(2\omega_2) = \epsilon_0\chi^{(2)}E_2^2 \text{ (second harmonic generation)}, \tag{2.19}$$

$$P(\omega_1 + \omega_2) = 2\epsilon_0\chi^{(2)}E_1E_2 \text{ (sum frequency generation)}, \tag{2.20}$$

$$P(\omega_1 - \omega_2) = 2\epsilon_0\chi^{(2)}E_1E_2^* \text{ (difference frequency generation), and} \tag{2.21}$$

$$P(0) = \epsilon_0\chi^{(2)}\left(E_1E_1^* + E_2E_2^*\right) \text{(optical rectification)}. \tag{2.22}$$

Sum frequency generation requires the presence of ω_1 and ω_2 to generate the higher frequency $\omega_3 = \omega_1+\omega_2$, and in the process, both input frequencies are depleted. However, difference frequency generation operates a bit differently. The high-frequency photon (called the pump, or ω_p) drives the down-conversion process, which is seeded by an intermediate-frequency photon (called the signal, or ω_s), leading to parametric gain in the signal and also generating low-frequency photons (called the idler, or ω_i). Because of the gain in the signal, difference frequency generation is also known as optical parametric amplification. Down-conversion can also occur without a seed, but the absence of a seed provides less gain, because the process is due to spontaneous emission, rather than stimulated emission [118]. As a result, a resonant cavity is typically used to amplify this spontaneous process significantly; this is referred to as optical parametric oscillation.

The second-order polarization term described in Eq. 2.17 is then implemented in a wave equation. The wave equation in a nonlinear medium can be obtained from Maxwell's equations for propagation in matter:

$$\nabla \cdot \tilde{\mathbf{D}} = \tilde{\rho}, \tag{2.23}$$

$$\nabla \cdot \tilde{\mathbf{B}} = 0, \tag{2.24}$$

$$\nabla \times \tilde{\mathbf{E}} = -\mu_0\frac{\partial\tilde{\mathbf{H}}}{\partial t}, \text{ and} \tag{2.25}$$

$$\nabla \times \tilde{\mathbf{H}} = \frac{\partial\tilde{\mathbf{D}}}{\partial t} + \tilde{\mathbf{J}}. \tag{2.26}$$

Assuming there are no free charges ($\tilde{\rho} = 0$), no free currents ($\tilde{\mathbf{J}} = 0$), and that the material is nonmagnetic ($\tilde{\mathbf{B}} = \mu_0 \tilde{\mathbf{H}}$), Maxwell's equations in matter can be simplified to:

$$\nabla \cdot \tilde{\mathbf{D}} = 0, \tag{2.27}$$

$$\nabla \cdot \tilde{\mathbf{B}} = 0, \tag{2.28}$$

$$\nabla \times \tilde{\mathbf{E}} = -\frac{\partial \tilde{\mathbf{B}}}{\partial t}, \text{ and} \tag{2.29}$$

$$\nabla \times \tilde{\mathbf{H}} = \frac{\partial \tilde{\mathbf{D}}}{\partial t}. \tag{2.30}$$

Then, taking the curl of Faraday's Law (Eq. 2.29),

$$\nabla \times \left(\nabla \times \tilde{\mathbf{E}}\right) = \nabla \times \left(-\mu_0 \frac{\partial \tilde{\mathbf{H}}}{\partial t}\right), \tag{2.31}$$

or, using Ampère's Law (Eq. 2.30),

$$\nabla \times \nabla \times \tilde{\mathbf{E}} + \mu_0 \frac{\partial^2}{\partial t^2} \tilde{\mathbf{D}} = 0. \tag{2.32}$$

The electric displacement $\tilde{\mathbf{D}}$ can be expressed in terms of the electric field and electric polarization $\tilde{\mathbf{D}} = \epsilon_0 \tilde{\mathbf{E}} + \tilde{\mathbf{P}}$, and the vacuum permeability μ_0 can be redefined in terms of the speed of light c and the vacuum permittivity ϵ_0:

$$\nabla \times \nabla \times \tilde{\mathbf{E}} + \frac{1}{c^2} \frac{\partial^2}{\partial t^2} \tilde{\mathbf{E}} = -\frac{1}{\epsilon_0 c^2} \frac{\partial^2 \tilde{\mathbf{P}}}{\partial t^2}. \tag{2.33}$$

The curl of the curl on the left-hand side can be expanded (Eq. A.1) and simplified, since $\nabla \cdot \tilde{\mathbf{E}}$ is slowly varying and thus $\nabla(\nabla \cdot \tilde{\mathbf{E}}) \ll \nabla^2 \tilde{\mathbf{E}}$, yielding the wave equation for light propagating in a medium [118]:

$$\nabla^2 \tilde{\mathbf{E}} - \frac{1}{c^2} \frac{\partial^2}{\partial t^2} \tilde{\mathbf{E}} = \frac{1}{\epsilon_0 c^2} \frac{\partial^2 \tilde{\mathbf{P}}}{\partial t^2}. \tag{2.34}$$

The polarization can be split into linear and nonlinear terms: $\tilde{\mathbf{P}} = \tilde{\mathbf{P}}^{(1)} + \tilde{\mathbf{P}}^{\mathrm{NL}}$. In an isotropic material, the linear term can be collected with the electric field using the relative permittivity $\epsilon^{(1)}$:

$$\epsilon_0\tilde{\mathbf{E}} + \tilde{\mathbf{P}}^{(1)} = \epsilon_0\epsilon^{(1)}\tilde{\mathbf{E}}. \tag{2.35}$$

Eq. 2.35 can be substituted into Eq. 2.34, which reduces to the inhomogenous wave equation

$$\nabla^2\tilde{\mathbf{E}} - \frac{\epsilon^{(1)}}{c^2}\frac{\partial^2\tilde{\mathbf{E}}}{\partial t^2} = \frac{1}{\epsilon_0 c^2}\frac{\partial^2\tilde{\mathbf{P}}^{\mathrm{NL}}}{\partial t^2}, \tag{2.36}$$

where the only driving term is the nonlinear polarization [118]. Eq. 2.36 can then be simplified into one-dimensional propagation (along the z direction), with the objective of forming coupled differential equations that can be solved numerically with experimental values [119]:

$$\frac{\partial^2 E(t,z)}{\partial z^2} - \mu_0\epsilon\frac{\partial^2 E(t,z)}{\partial t^2} = \frac{1}{\epsilon_0 c^2}\frac{\partial^2 P_{NL}(t,z)}{\partial t^2}. \tag{2.37}$$

In the frequency domain, Eq. 2.37 can be rewritten using Eq. A.2, the wavenumber k, and the angular frequency ω:

$$\frac{\partial^2 e(\omega,z)}{\partial z^2} + k^2 e(\omega,z) = -\frac{\omega^2}{\epsilon_0 c^2}p_{NL}(\omega,z), \tag{2.38}$$

where lowercase variables denote the Fourier-transformed counterparts of the uppercase time-domain variables. The k used here is then replaced by κ, a wavenumber centered around $k_0 = k(\omega_0)$ where ω_0 is the central angular frequency. $\kappa(\Omega) = k(\omega) - k_0$, so e is then rewritten as

$$e(\omega,z) = a(\Omega,z)\mathrm{e}^{-ik_0 z}. \tag{2.39}$$

Replacing e with a changes the frequency-basis wave equation to

$$\left(\frac{\partial^2 a}{\partial z^2} + \kappa^2 a\right) - 2ik_0\frac{\partial a}{\partial z} + 2\kappa k_0 a = -\frac{\omega^2}{\epsilon_0 c^2}p_{NL}\mathrm{e}^{ik_0 z}. \tag{2.40}$$

The electric field can be represented with κ in the exponential term, such that its magnitude and phase slowly vary and its second derivative can be approximated to be zero, and use this to simplify Eq. 2.40:

$$s(\Omega,z) = a(\Omega,z)\mathrm{e}^{i\kappa z}, \text{ and so} \tag{2.41}$$

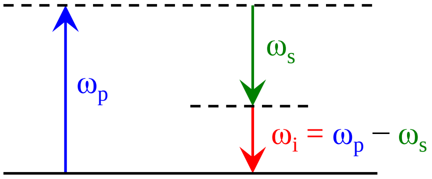

Figure 2.2: Cartoon of the difference frequency generation and optical parametric oscillation process. Pump photons (ω_p) drive the down-conversion process, which generates both signal (ω_s) and idler (ω_i) photons.

$$\frac{\partial^2 s}{\partial z^2} = 0 = \left(\frac{\partial^2 a}{\partial z^2} + 2i\kappa\frac{\partial a}{\partial z} - \kappa^2 a\right)\mathrm{e}^{i\kappa z}. \tag{2.42}$$

Substituting the second-derivative term in Eq. 2.40 simplifies the equation to:

$$\frac{\partial a}{\partial z} + i\kappa a = -i\frac{\omega}{2\epsilon_0 nc}p_{NL}\mathrm{e}^{ik_0 z}. \tag{2.43}$$

Up to this point, the particular $\chi^{(2)}$ process involved has not been chosen. The nonlinear polarization p_{NL} can now be replaced with its definition from Eqs. 2.20 and 2.21, depending on which frequency is the sum of the other two), and $\chi^{(2)}$ can also be defined in terms of d, the effective nonlinear coefficient: $d = \frac{1}{2}\chi^{(2)}$. Using the pump, signal, and idler definition of $\omega_i = \omega_p - \omega_s$ (see Fig. 2.2):

$$P_p^{(2)} = \epsilon_0 d_p E_s E_i, \tag{2.44}$$

$$P_s^{(2)} = \epsilon_0 d_s E_p E_i^*, \text{ and} \tag{2.45}$$

$$P_i^{(2)} = \epsilon_0 d_i E_p E_s^*, \tag{2.46}$$

or, transferring into frequency space using convolutions and cross-correlations (Eqs. A.6 and A.7),

$$p_p^{(2)} = \frac{\epsilon_0 d_p}{2\pi} e_s \otimes e_i, \tag{2.47}$$

$$p_s^{(2)} = \frac{\epsilon_0 d_s}{2\pi} e_p \oplus e_i, \text{ and} \tag{2.48}$$

$$p_i^{(2)} = \frac{\epsilon_0 d_i}{2\pi} e_p \oplus e_s. \tag{2.49}$$

Changing these into a_j and substituting into Eq. 2.43, the final set of coupled differential equations in frequency space used for simulating three-wave mixing processes are as follows:

$$\frac{\partial a_s}{\partial z} + i\kappa_s a_s = -i\frac{\omega_s d_s}{4\pi c n_s} a_p \oplus a_i, \tag{2.50}$$

$$\frac{\partial a_i}{\partial z} + i\kappa_i a_i = -i\frac{\omega_i d_i}{4\pi c n_i} a_p \oplus a_s, \text{ and} \tag{2.51}$$

$$\frac{\partial a_p}{\partial z} + i\kappa_p a_p = -i\frac{\omega_p d_p}{4\pi c n_p} a_s \otimes a_i. \tag{2.52}$$

A numerical simulation has been developed to simulate this three-wave mixing process as it pertains to laboratory work, both in an optical parametric oscillator (Chapter 3) and in difference frequency generation (Chapter 5).

2.3.1 Test Case: Continuous-Wave, Undepleted Pump

A common simple case of difference frequency generation is the case with continuous-wave inputs and significant power in the high-energy pump (ω_p), meaning that the power there depletes very little and can be assumed to be constant. Ref. [118] derives an analytic solution for this case in the time domain, and it can be compared to the complete model shown in Eq. 2.52 to verify its accuracy.

$$P(\omega_1 - \omega_2) = 2\epsilon_0 \chi^{(2)} E_1 E_2^*, \tag{2.21}$$

or, switching to ω_p, ω_s, and ω_i notation and replacing $\chi^{(2)}$ with d_{eff},

$$P(\omega_i) = 4\epsilon_0 d_{\text{eff}} E_p E_s^*. \tag{2.53}$$

The electric field in the time domain varies both temporally and spatially:

$$\tilde{E}_i(z,t) = A_i e^{i(k_i z - w_i t)} + \text{c.c.} \tag{2.54}$$

Substituting Eq. 2.53 and Eq. 2.54 into the inhomogeneous wave equation (Eq. 2.36) gives the differential equation

$$\frac{\mathrm{d}^2 A_i}{\mathrm{d}z^2} + 2ik_i\frac{\mathrm{d}A_i}{\mathrm{d}z} = \frac{-4d_{\text{eff}}\omega_i^2}{c^2} A_p A_s^* e^{i\Delta k z}, \tag{2.55}$$

where Δk is $k_p - k_s - k_i$. Assuming A_j varies slowly, the second derivative of A_i (the first term in Eq. 2.55) is removed, and Eq. 2.55 and its analog for A_s become

$$\frac{\mathrm{d}A_s}{\mathrm{d}z} = \frac{2i\omega_s^2 d_{\text{eff}}}{k_s c^2} A_p A_i^* e^{i\Delta k z} \text{ and} \tag{2.56}$$

$$\frac{\mathrm{d}A_i}{\mathrm{d}z} = \frac{2i\omega_i^2 d_{\text{eff}}}{k_i c^2} A_p A_s^* e^{i\Delta k z}. \tag{2.57}$$

Eqs. 2.56 and 2.57 can be combined by taking the derivative of one and taking the complex conjugate of the other:

$$\frac{\mathrm{d}^2 A_i}{\mathrm{d}z^2} = \frac{4\omega_s^2\omega_i^2 d_{\text{eff}}^2}{k_i k_s c^4} A_p A_p^* A_i \equiv \kappa^2 A_i, \tag{2.58}$$

where the coupling constant κ has been introduced and is defined as

$$\kappa^2 = \frac{4\omega_s^2\omega_i^2 d_{\text{eff}}^2}{k_i k_s c^4} |A_p|^2. \tag{2.59}$$

The solution to this differential equation based on the boundary condition $A_i(z = 0) = 0$ is the hyperbolic secant (sinh) function, and so

$$A_s(z) = A_s(0)\cosh(\kappa z) \text{ and} \tag{2.60}$$

$$A_i(z) = i\sqrt{\frac{n_s\omega_i}{n_i\omega_s}} \frac{A_p}{|A_p|} A_s^*(0)\sinh(\kappa z). \tag{2.61}$$

This analytic solution can be tested against the more generalized set of coupled equations for a sufficiently large pump. Fig. 2.3 compares the two, and is a plot of the output from the test file `dfg_test.py` in the PyNLO package under the `src/validation` directory.

The plot in Fig. 2.3 shows the powers of a signal (top) and idler (bottom) in 10 cm of silver gallium selenide (AgGaSe_2). All beams are continuous-wave (CW) so that group velocity mismatch and group velocity dispersion do not affect the behavior of the beams. With a pump wavelength of 1560 nm and a signal wavelength of 2200 nm, the idler wavelength is 5360 nm. As this is the case of undepleted pump, the pump power is significantly larger than that of the signal; the pump power is 25 kW whereas the signal power is 100 mW. The beam waist here is 10 mm.

With this test case shown to be accurate, the model can be used to predict the behavior in the experimental apparatuses discussed in this thesis, which will be detailed in Chapters 3, 5, and 6.

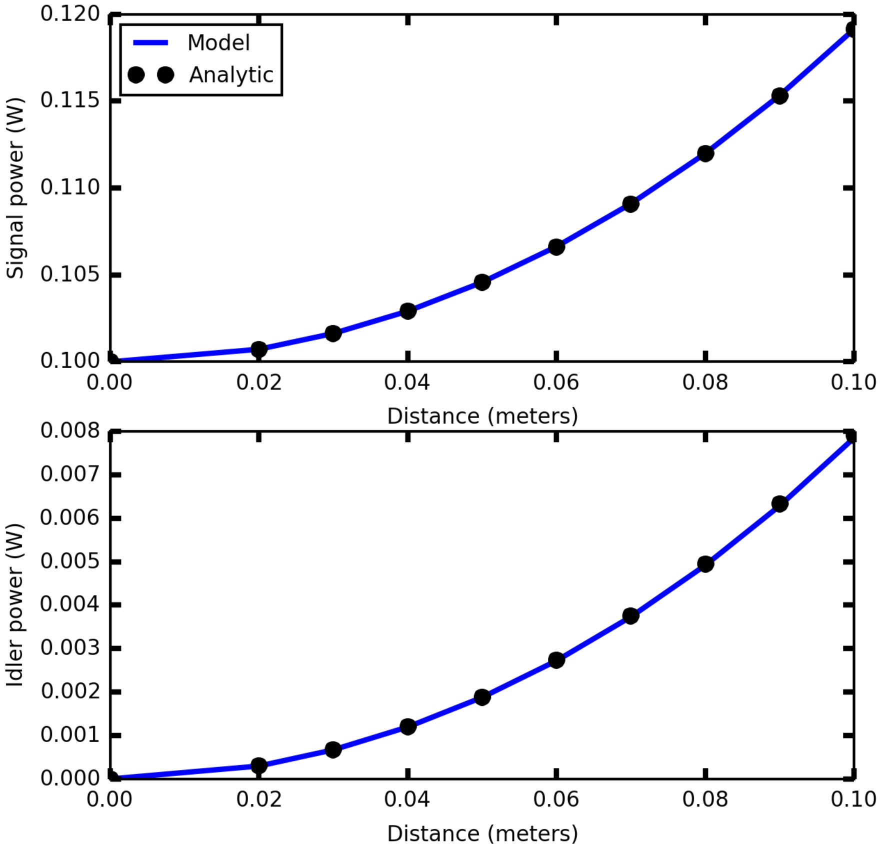

Figure 2.3: Comparison of analytical solution (Eqs. 2.60 and 2.61, black dots) to the integrated coupled equations (Eq. 2.52, blue line) for the strong pump case. Near-perfect agreement is seen. $\lambda_p = 1560$ nm, $\lambda_s = 2200$ nm, and $\lambda_i = 5360$ nm. $P_p = 25$ kW and $P_s = 100$ kW. The beam waist $w = 10$ mm.

2.4 $\chi^{(3)}$ Processes and Four-Wave Mixing

Three-wave mixing describes the free-space nonlinear processes used to reach mid-infrared wavelengths. However, the sources used to seed these processes are generated in optical fiber, and these processes are described using four-wave mixing, which is a $\chi^{(3)}$ process, stemming from the third-order polarization term in Eq. 2.2 [118]. Assuming monochromatic light of the form

$\tilde{E}(t) = \mathcal{E} \cos \omega t$,

$$\tilde{P}^{(3)}(t) = \epsilon_0 \chi^{(3)} \tilde{E}^3(t) \tag{2.62}$$

$$= \epsilon_0 \chi^{(3)} \mathcal{E}^3 \cos^3 \omega t \tag{2.63}$$

$$= \frac{1}{4} \epsilon_0 \chi^{(3)} \mathcal{E}^3 \left(\cos 3\omega t + 3 \cos \omega t \right). \tag{2.64}$$

The first term of Eq. 2.64 describes third-harmonic generation. The second term describes how a third-order polarization term affects the fundamental frequency based on its electric field intensity. This portion of the third-order polarization term behaves as an intensity-dependent refractive index, also known as the optical Kerr effect or self-phase modulation, and can be expressed as $n = n_0 + n_2 I$.

In a material with $\chi^{(1)}$ and $\chi^{(3)}$ responses, these can be collected into an effective susceptibility χ_{eff} where $\chi_{\text{eff}} = \chi^{(1)} + 3\chi^{(3)}\mathcal{E}^2$ [118]. As $n^2 = 1 + \chi_{\text{eff}}$, these terms separate [118]:

$$n^2 = 1 + \chi_{\text{eff}} \tag{2.65}$$

$$(n_0 + n_2 I)^2 = 1 + \chi^{(1)} + 3\chi^{(3)} \mathcal{E}^2$$

$$n_0 = \sqrt{1 + \chi^{(1)}} \text{ (linear term)} \tag{2.66}$$

$$4 n_0 n_2 I = 3\chi^{(3)} \frac{I}{2 n_0 \epsilon_0 c}$$

$$n_2 = \frac{3}{4 n_0^2 \epsilon_0 c} \chi^{(3)} \text{ (nonlinear term)} \tag{2.67}$$

where the term of order I^2 are dropped. Thus, we see that the intensity of a pulse can affect its index refraction, and thus its group velocity.

The group velocity is also affected by group velocity dispersion, which is the dependence of group velocity on frequency. It is defined as:

$$\text{GVD}(\omega) = \frac{\partial}{\partial \omega} \left(\frac{1}{v_g(\omega)} \right) = \frac{2}{c} \left(\frac{\partial n}{\partial \omega} \right) + \frac{\omega}{c} \left(\frac{\partial^2 n}{\partial \omega^2} \right). \tag{2.68}$$

Thus, two different phenomena — group velocity dispersion and the Kerr effect — can affect the evolution of pulses in optical fiber by altering the propagation of different components of a pulse, either based on frequency or intensity. This interplay can be described using the nonlinear

Schrödinger equation (NLSE). A complete derivation is quite extensive, and is described in great detail in [122]. The NLSE for a light field in a medium is [123]:

$$\frac{\partial A(z,t)}{\partial z} = (\hat{D} + \hat{N})A(z,t), \text{ where} \tag{2.69}$$

$$\hat{D} = -i\frac{\beta_2}{2}\frac{\partial^2}{\partial t^2} - \frac{\alpha}{2}, \text{ and} \tag{2.70}$$

$$\hat{N} = i\gamma|A|^2. \tag{2.71}$$

$\hat{D}$ is the dispersion term, describing both the spread of the pulse from second-order dispersion (β_2) and any linear losses (α), and $\hat{N}$ is the nonlinear operator, where the nonlinear coefficient γ is defined as [124]

$$\gamma = \frac{n_2\omega_0}{cA_{\text{eff}}} \tag{2.72}$$

and A_{eff} is the effective core area of the fiber.

In the absence of absorptive losses ($\alpha = 0$), if β_2 is negative (anomalous dispersion), $\hat{D}A$ can equal $-\hat{N}A$, in which case the pulse will not evolve as it propagates. This describes a first-order (or fundamental) soliton.

The NLSE above, however, lacks a few additional optical effects. The generalized nonlinear Schrödinger equation (GNLSE) is more descriptive [54, 123]:

$$\hat{D} = -\frac{\alpha}{2} - \sum_{n\geq 2}\beta_n\frac{i^{n-1}}{n!}\frac{\partial^n}{\partial t^n}, \text{ and} \tag{2.73}$$

$$\hat{N} = \frac{i\gamma(\omega)}{A}\left(1 + i\tau_{\text{shock}}\frac{\partial}{\partial t}\right)\left((1-f_R)|A|^2A + f_RA\int_0^\infty h_R(t')|A(z,t-t')|^2\mathrm{d}t'\right). \tag{2.74}$$

Between both operators (Eqs. 2.73 and 2.74), the GNLSE essentially has four terms. $\hat{D}$ has a linear attenuation term (α) and a chromatic dispersion term (β). Compared to the NLSE, α and the higher-order β terms are new additions to the GNLSE. Additionally, the GNLSE incorporates two new nonlinear optical effects in $\hat{N}$.

One of these effects is transient stimulated Raman scattering [125], which describes a four-photon process transferring energy from a pump wave to lower- and higher-frequency waves through phonon interaction. This is accounted for with the splitting of the Kerr effect into a term that incorporates the fractional Raman response f_R, which features the Raman response function h_R, and a term that describes the Kerr effect without the fractional Raman response, $(1 - f_R)$. This phenomenon is commonly observed as self-frequency shifting, where high-frequency components provide gain for low-frequency components and the optical spectrum shifts to longer wavelengths.

Additionally, $\hat{N}$ allows for for an effect called self-steepening. This describes the formation of an optical shock, where the pulse peak's velocity is reduced, leading to an increasing slope of the trailing edge of a pulse, up to the limit of what chromatic dispersion will permit [126]. The time scale of this effect is τ_{shock}. If the shock term is removed and $f_R = 0$, Eq. 2.74 simplifies to the Kerr effect from Eq. 2.71.

The GNLSE is integrated numerically using the split-step Fourier method [54, 123], where different portions of the differential equation are numerically integrated in different domains. The dispersion, a frequency-dependent effect, is integrated in the frequency domain, but the Kerr effect, an intensity-dependent effect, must be integrated in the time domain.

2.4.1 Test Cases from Literature

The purpose for basic testing of this simulation was two-fold: first, to make sure that basic examples from the literature were able to reproduced, and second, to reach a fundamental understanding of pulse dynamics in fiber based on the dominant effects before introducing the added complexity of all the terms featured in the GNLSE (Eq. 2.74). The code for these test cases is publicly available in the PyNLO package under the `Old and Partial Tests` directory, under `src/validation`.

The first test solely investigates the behavior of a Gaussian pulse, without dispersion, due to the nonlinear refractive index. This is shown in Fig. 2.4, and matches the behavior shown for a pulse in Ref. [124]. Continuous spectral broadening is visible, but does not occur evenly, as is typical in self-phase modulation. The corresponding code for this plot is in `Agrawal_SSFM.py`.

The second test incorporates both self-phase modulation and second-order dispersion, and is also presented in Ref. [124]. Here, anomalous dispersion is introduced to balance self-phase

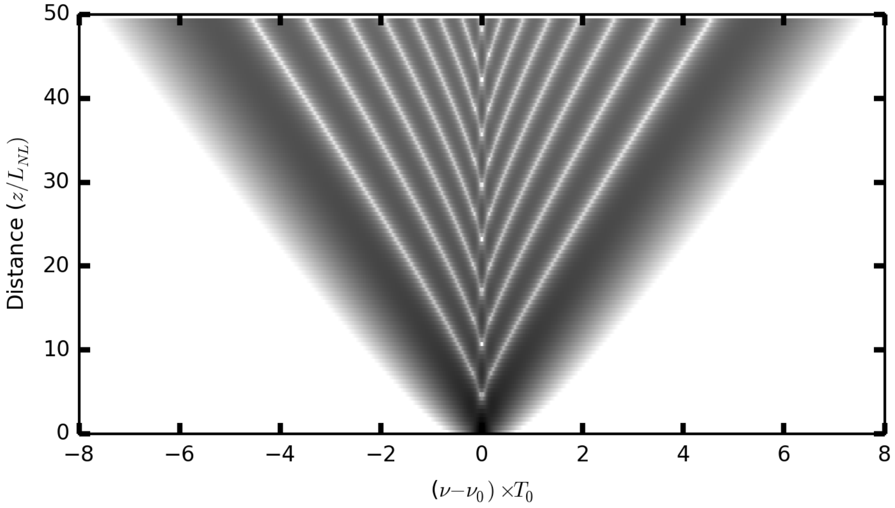

Figure 2.4: Behavior of a pulse due to the nonlinear refractive index. Intensity is shown in grayscale, where the highest intensity is the darkest. The x-axis shows a dimensionless normalized frequency, where the centered frequency ($\nu - \nu_0$, where ν_0 is the central frequency) is multiplied by T_0, the pulse width. The y-axis shows the distance divided by $L_{NL} = (\gamma P_0)^{-1}$, the nonlinear length.

modulation; however, it is not a fundamental soliton. Rather, an integer-square more power results in breathing and repeated behavior of the soliton. In Fig. 2.5, a fourth-order soliton is shown, where the power is $4^2 = 16$ times more than that of a fundamental soliton. Three slices of the plot at different distances are shown in Fig. 2.6, in both time and frequency. The code for this test case is in `fundamental_SSFM.py`.

The "breathing" characteristic of higher-order solitons is evident here. When the pulse is at its longest (blue in Fig. 2.6), at $z/L_{NL} = 0$, anomalous dispersion dominates, and the pulse compresses. As this occurs, the spectrum broadens, reaching maximal spectral width and shortest duration at $z/L_{NL} = 0.2$. Here, self-phase modulation dominates, and the pulse breaks apart into two peaks temporally, as seen in green in Fig. 2.6. Then, the portions of the pulse with high intensity broaden due to self-phase modulation, but the portions with low intensity disperse without the effect of self-phase modulation. This causes three peaks at $z/L_{NL} = 0.8$ (red, in Fig. 2.6). These effects and features then repeat, in reverse order, until the short pulse is created again at $z/N_{NL} = 1.6$.

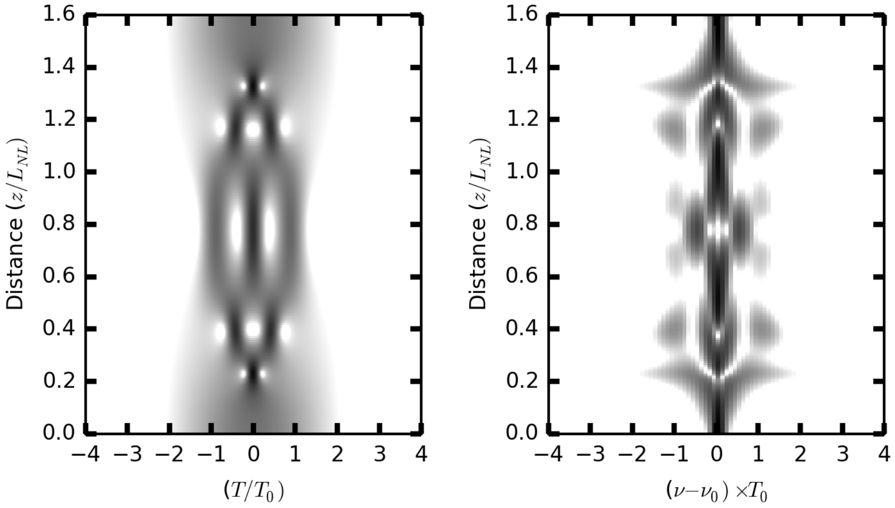

Figure 2.5: A fourth-order soliton propagating in optical fiber, the intensity of which is plotted both in time (left) and frequency (right). The x-axis of the left plot is delay divided by T_0, the pulse width. The x-axis of the right plot is frequency, plotted as in Fig. 2.4. The y-axis is distance divided by $L_D = T_0^2/|\beta_2|$, the dispersion length.

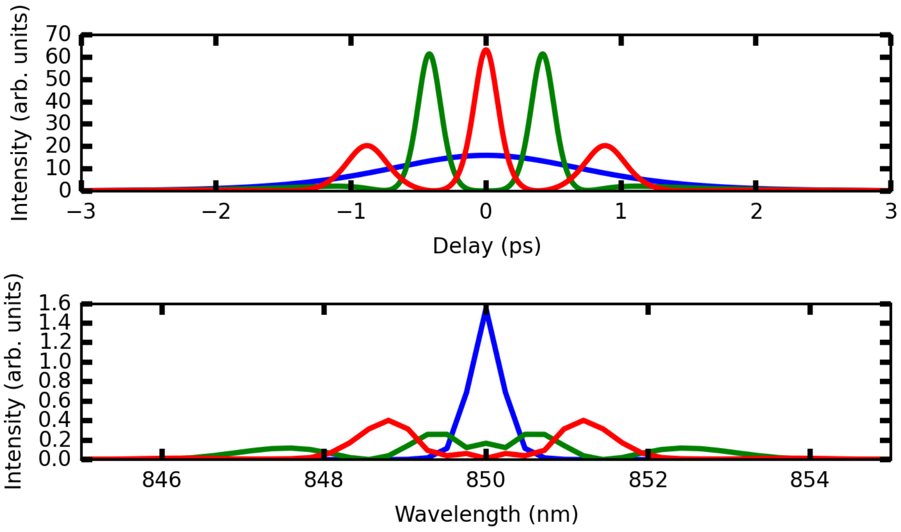

Figure 2.6: Three slices of Fig. 2.5, shown in time (top) and wavelength (bottom). Blue curves represent $z/L_{NL} = 0$, green is at 0.4, and red is at 0.8.

The two examples thus far have only tested the NLSE shown in Eq. 2.69, without any higher-order dispersion or other effects. In order to properly demonstrate the ability to simulate

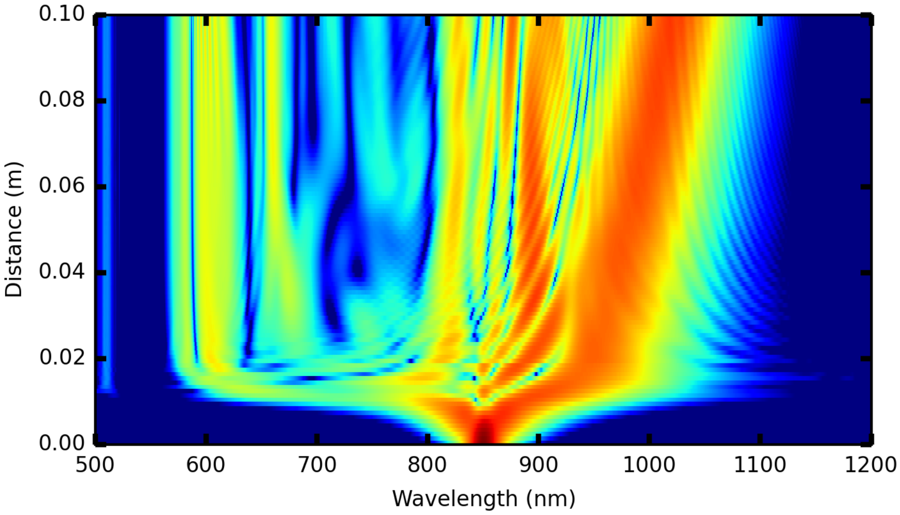

Figure 2.7: Full GNLSE simulation of a pulse propagating in silica fiber, regenerated from parameters listed in Ref. [54]. The Raman frequency shift is evident, as a band of spectral intensity is quickly shifted from the center frequency of 850 nm to 950 nm, and continues to shift to longer wavelengths as the pulse propagates.

experimental conditions, the model needs to be shown to accurately represent higher-order dispersion terms as well as the additional nonlinear interaction terms introduced in Eq. 2.74. In Refs. [54, 120], β_2 through β_7 and γ are listed, and simulations are presented in both works.

Fig. 2.7 successfully reproduces the plot shown in Ref. [54], with a characteristic Raman frequency redshift to approximately 1025 nm after 10 cm of propagation. This shows that the simulation that has been developed can accurately predict all of the fiber behaviors described in the GNLSE, and is suitable for experimental prediction, which will be further described in Chapter 4. The corresponding code for this plot is `Hult_SSFM.py`.

Chapter 3

Optical Parametric Oscillator

3.1 Introduction

This chapter describes the development of an optical parametric oscillator (OPO) used to down-convert a 2 µm pump source into a signal and idler wave between 3 and 5 µm. Optical parametric amplification (briefly introduced in Sec. 2.3) is a process in which high-energy pump photons are down-converted into lower-energy signal and idler photons. This process is not stimulated via the introduction of lower energy photons, but instead a cavity, resonant for both signal and idler (or doubly-resonant) is used to build gain from the mid-infrared photons generated through vacuum fluctuations (see Fig. 3.1). Each successive pump pulse drives the parametric gain process for the signal and idler, which is referred to as synchronous pumping. The physics behind the operation of OPOs has been described in Sec. 2.3 and has been studied in great detail in the literature

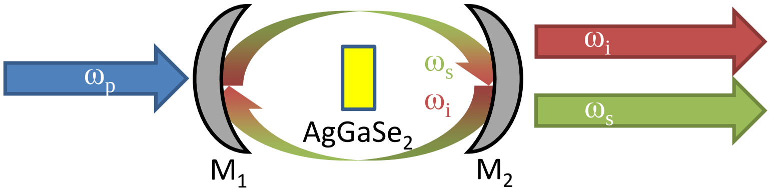

Figure 3.1: Diagram depicting the doubly-resonant optical parametric amplification process. Pump photons (ω_p) are coupled into a cavity, where signal (ω_s) and idler (ω_i) photons are produced in a nonlinear crystal (here, silver gallium selenide) and amplified in the resonant cavity enclosed by mirrors M_1 and M_2. A portion of the signal and idler are coupled out of the cavity for measurements.

[127–129]. OPOs are well-established and understood experimentally as well; OPOs have been developed as a reliable source in this spectral region previously [25, 26, 30, 130]. However, much of this earlier work implemented orientation-patterned gallium arsenide (OP-GaAs) and periodically-poled lithium niobate (PPLN) [28, 131–135], which are both more expensive and more difficult to produce, and thus less suitable for more mainstream applications.

The crystal used for nonlinear conversion in this OPO is made of silver gallium selenide ($AgGaSe_2$), a commercially available (see the appendix, in Sec. B.6) uniaxial crystal, the implementation of which only requires a broadband anti-reflective (BBAR) coating on the surfaces and for the crystal to be cut at an angle such that birefringent phase-matching (BPM) can be used [136]. $AgGaSe_2$ is also transparent for a broad range of wavelengths (0.71–18 µm) and has a high effective nonlinear coefficient ($d = 33$ pm/V) [129].

The main result of this chapter is the demonstration of broadly tunable spectra between 3–5 µm, with a peak combined signal and idler power of 50 mW. This is significant because of the broad range of wavelengths capable of being produced coherently with an inexpensive nonlinear medium. The effect of a variety of parameters were investigated, including the effect of a buffer gas and two different crystal lengths. Lastly, numerical modeling, based on the coupled equations detailed in Sec. 2.3, was used to confirm the observed behavior.

3.2 Methods

The pump source for the OPO is shown in Fig. 3.2, and was developed by Florian Adler, a previous colleague at NIST [137]. It is a hybrid Er:fiber/Tm:fiber frequency comb centered at 1950 nm, with a maximum average power of 2.0 W at its output and a pulse duration of roughly 180 fs, with a repetition rate of 100 MHz. The spectrum and interferometric autocorrelation of the pump are shown in Fig. 3.3.

A diagram of the experimental setup is shown in Fig. 3.4. The beam was shaped by three lenses; a spherical mirror focused the beam, and two cylindrical lenses (one of each orientation) re-collimated the beam into an oval shape, pre-astigmatizing it before entering the OPO. The OPO

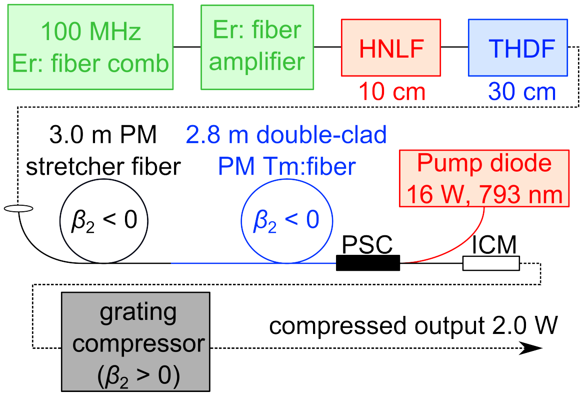

Figure 3.2: Schematic for the source used to pump the OPO. An erbium fiber oscillator generated comb light centered at 1.5 µm, which was amplified in an erbium-doped fiber amplifier. This spectrum was then broadened to 2 µm in highly nonlinear fiber (HNLF), and the remaining 1.5 µm light self-pumped the 2 µm portion of the spectrum in thulium/holmium co-doped fiber (THDF). The pulse was then stretched to avoid acquiring nonlinear phase in fiber, then amplified to 4.8 W in thulium fiber, pumped with an external diode via a pump-signal combiner (PSC). An isolator and collimator module (ICM) launched the amplified beam into free-space, where a grating compressor shortened the pulse, yielding 2.0 W of compressed output.

was contained within a box with Brewster-angled windows allowing the entry and exit of the beams. The box was closed such that a buffer gas (N_2) could flow in through a teflon tube (not shown) to reduce the effect of atmospheric CO_2 and any water vapor effects. The entry window was Brewster-angled for the pump beam and was made of silica. The pump beam was coupled into the cavity through an output coupler produced by Quality Thin Films, Inc. The output coupler was highly reflective from 3500–4500 nm while highly transmissive from 1980–2010 nm. The effective cavity length was $c/(100\text{ MHz})$, or roughly 3 m. Spherical mirrors focused the beam with an intensity of 6 GW/cm^2 on the $AgGaSe_2$ crystal (produced by Altechna), cut to the phase-matching angle of $\theta = 52.8°$, $\varphi = 45°$ for Type-I degenerate OPO operation (1.96 µm → 3.92 µm). A small fraction (< 1 %) of the cavity light passed through the output coupler and exited the OPO box through a second Brewster-angled window, which was angled such that there was no loss of the signal and idler, rather than the pump, which has the opposite polarization. Part of this exiting light was focused onto a 2 µm photodetector, while the rest passed through a long-pass filter, and the signal and idler were detected using either an infrared camera or a Fourier-transform spectrometer.

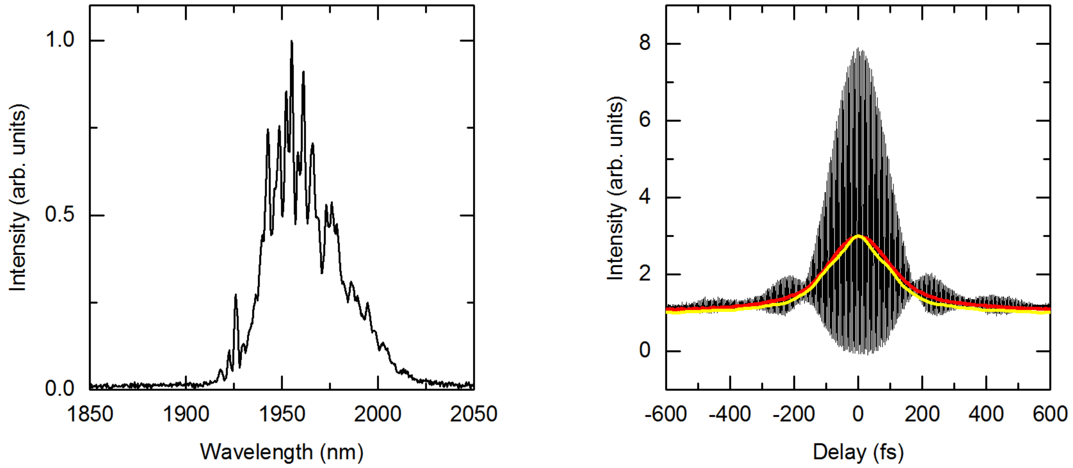

Figure 3.3: Left: Optical spectrum of the Tm:fiber amplifier output. Data were measured using a long-wave optical spectrum analyzer (OSA). Right: Interferometric autocorrelation (black), intensity autocorrelation (red), and Fourier-transformed and autocorrelated optical spectrum (yellow) of the amplified pump beam. The x-axis was calibrated by measuring how a delay introduced by a translation stage was mapped to the scope trace temporally.

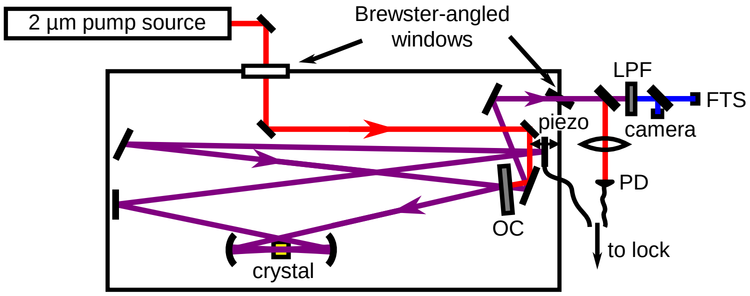

Figure 3.4: Diagram of the experimental setup. Red indicates the pump beam, purple indicates the combination of pump, signal, and idler, and blue indicates the signal and idler with the pump removed by the long-pass filter (LPF). The 2 µm pump source (detailed in Fig. 3.2) was shaped by two cylindrical lenses (not shown) before entering the oscillator box through a Brewster-angled window. The pump light was coupled into the cavity through an output coupler (OC). A piezoelectric transducer (piezo) allowed the cavity length to be locked. The residual pump light and a small fraction of the generated light escaped the cavity through the output coupler. The photodetector (PD) is used to measure the depletion of the pump as it is converted into the signal and idler. A Fourier-transform spectrometer (FTS) was used to measure the wavelength of the produced light, and an InSb camera was used to image the generated beam.

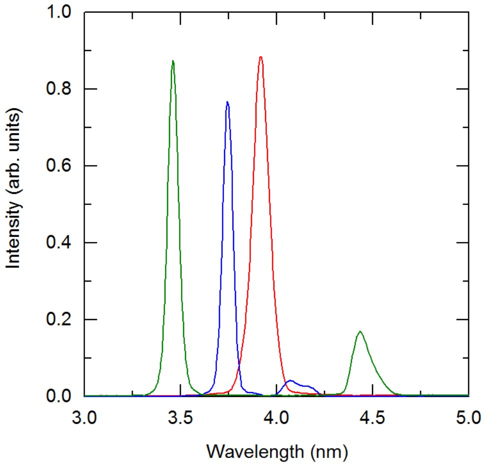

Figure 3.5: Three sample spectra produced by the 1 mm crystal, denoting the spectral coverage of different signal-idler pairs. Shown are degenerate (red), nearly degenerate (blue), and non-degenerate (green) spectra.

An initial alignment was achieved using interference of the 2 µm pump. A small fraction of the pump light was reflected off the output coupler, and, when aligned, was collinear with the exiting cavity beam. Applying a triangle wave to the piezo created fringing visible on the photodetector, and optimal alignment had the strongest contrast between the two beams. The cavity length where optical parametric oscillation was achieved was slightly different due to a difference in the index of refraction in the crystal, but occurred at roughly the same alignment. As resonant pump light was converted to signal and idler, sharp depletion peaks occur in the pump light detected at the photodetector. These occurred at discrete locations, rather than continuously, due to the double resonance condition. The piezo was locked to each of these depletion peaks using a peak lock servo. At each the spectrum of the created signal and idler were measured using a Fourier-transform spectrometer.

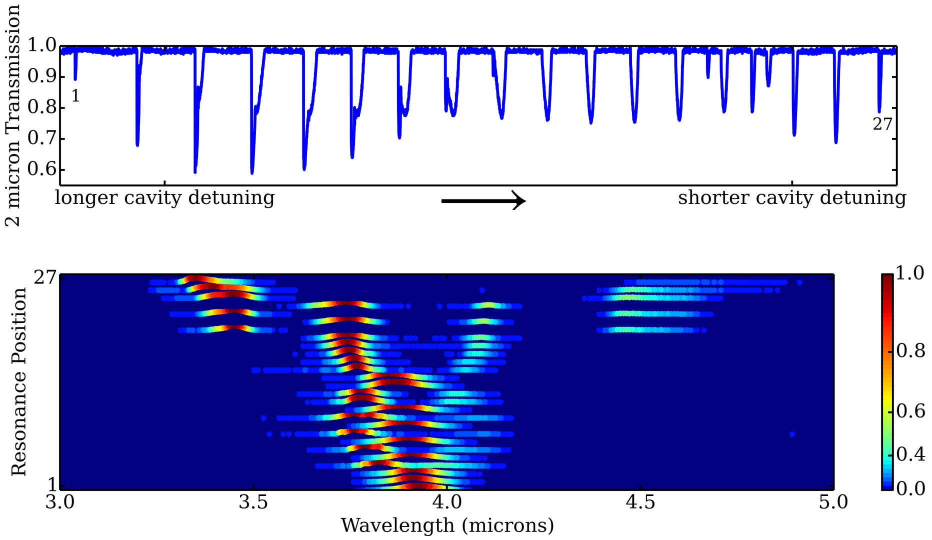

Figure 3.6: Spectra generated in a 1 mm crystal, in ambient air. Top: oscilloscope trace of pump transmission vs. cavity length, showing the position of each resonance where 2 µm light was depleted as optical parametric oscillation occurred. First and last resonance positions are marked 1 and 27. Bottom: mid-infrared spectrum produced at each resonance position, corresponding to peaks marked in the top plot. Spectra are normalized individually to 1, vertically separated for clarity, and plotted on a logarithmic scale.

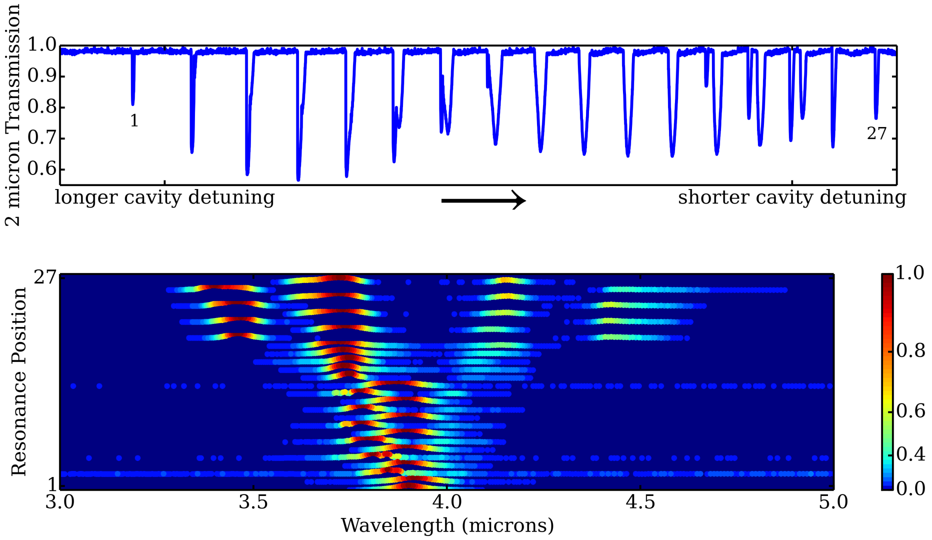

Figure 3.7: Spectra generated in a 1 mm crystal, plotted as in Fig. 3.6, with coarse cavity purging using dry nitrogen.

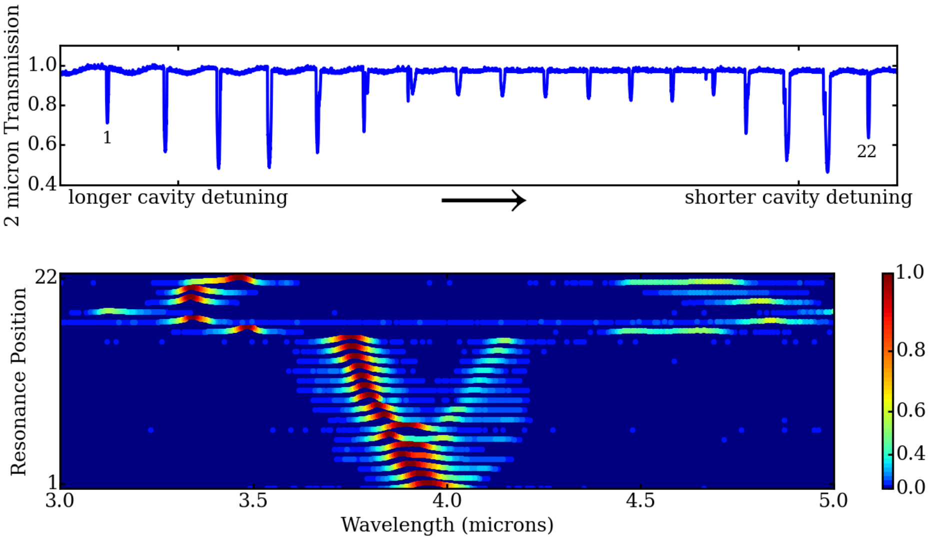

Figure 3.8: Spectra generated in a 0.5 mm crystal, plotted as in Fig. 3.6, with coarse cavity purging using dry nitrogen.

3.3 Results

Typical data are shown in Figs. 3.6 and 3.7 for 1 mm-thick crystals with the cavity in either ambient air or coarsely purged with dry nitrogen, respectively. Fig. 3.8 shows data using a 0.5 mm-thick crystal in a cavity also purged with dry nitrogen. The N_2 was used as a buffer primarily to reduce the effect of intracavity CO_2. The depletion oscilloscope trace is shown at top, with the corresponding spectra shown at bottom. Both 1 mm crystal configurations were able to resonate at 27 distinct cavity positions, whereas the shorter 0.5 mm crystal resonated at 22. These resonance positions are dictated by the synchronous pumping condition, where successive pump pulses are no longer able to drive the down-conversion process for the resonant signal and idler waves. Degenerate spectra are shown at the bottom of the color map and give way to nearly degenerate spectra interleaved with fully degenerate spectra. These become less degenerate and become interleaved with fully nondegenerate spectra. A sampling of this range of spectra is shown in Fig. 3.5. Stronger depletion occurred with the thicker crystal, as expected; however, new peaks also occurred in "doublets," partnered with pre-existing peaks and produced spectra of a different signal-idler spacing. Using the output coupling scheme shown in the schematic (Fig. 3.4), powers of

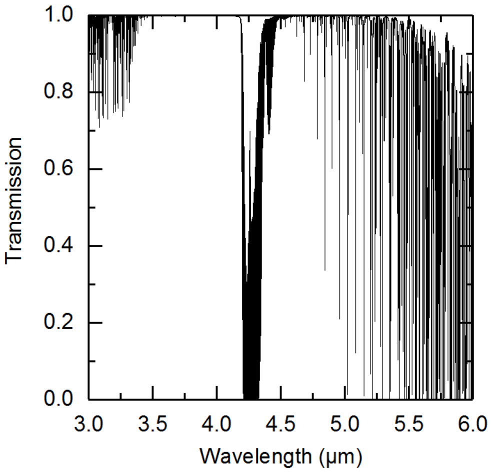

Figure 3.9: Atmospheric transmission for one round-trip around the cavity (3 meters) [55]. The prominent feature in the center, at 4.3 µm, is as a result of carbon dioxide.

roughly 3 mW were seen from the combined signal and idler at degeneracy. However, powers of up 48 mW were observed using a different output coupling scheme, where a calcium fluoride window was introduced to the cavity near Brewster's angle for the signal and idler as a pickoff optic after the pump had reached the crystal.

3.4 Discussion and Simulations

One clear result evident in the spectra shown in Figs. 3.6 and 3.7 is the gap in spectral generation between 3.5–3.6 µm and 4.2–4.4 µm. This is a signal-idler pair that appears to correspond to the strong atmospheric absorption peak from carbon dioxide, seen in Fig. 3.9. Even though the cavity in Fig. 3.7 used a flow of dry nitrogen, the cavity was not hermetically sealed, nor was it pumped out to vacuum before filling. While the concentration of carbon dioxide decreased through the use of nitrogen, the cavity still would not resonate near this strong carbon dioxide absorption feature.

However, the absorption feature seen in Fig. 3.9 is quite narrow, and the observed spectral gap, even in the purged system, is substantially broader. The behavior of the OPO was modeled

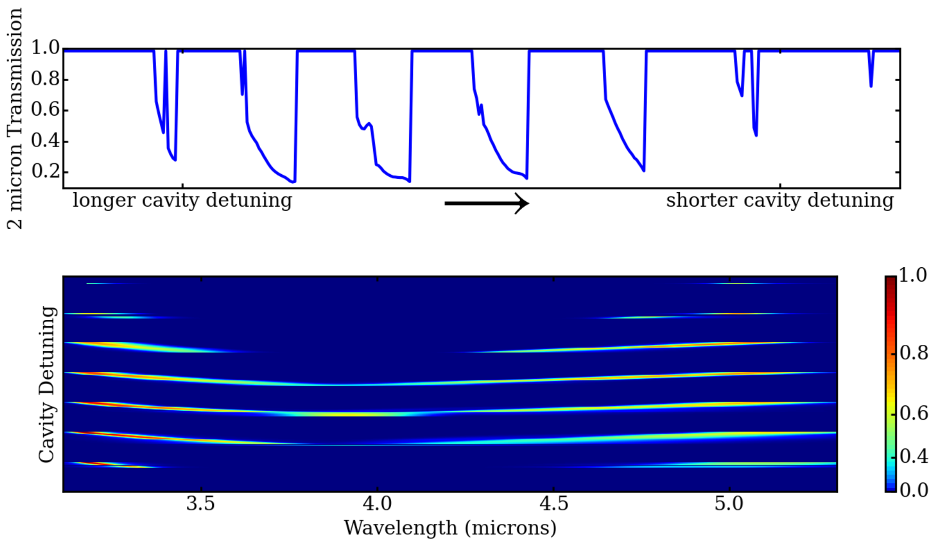

Figure 3.10: Simulation of OPO without atmospheric absorption, plotted similarly to experimental data. Depletions in the 2 µm pump as a function of cavity length are shown at top, and the generated spectra as a function of wavelength and cavity length are plotted at bottom.

to understand this behavior, using the coupled equations from Sec. 2.3 [119]:

$$\frac{\partial a_s}{\partial z} + i\kappa_s a_s = -i\frac{\omega_s d_s}{4\pi c n_s} a_p \oplus a_i, \tag{2.50}$$

$$\frac{\partial a_i}{\partial z} + i\kappa_i a_i = -i\frac{\omega_i d_i}{4\pi c n_i} a_p \oplus a_s, \text{ and} \tag{2.51}$$

$$\frac{\partial a_p}{\partial z} + i\kappa_p a_p = -i\frac{\omega_p d_p}{4\pi c n_p} a_s \otimes a_i. \tag{2.52}$$

The pump in this case is the spectrum from Fig. 3.3, and the signal and idler fields are not initially seeded. Rather than set to zero, these vectors are filled with vacuum fluctuations (10^{12} less power than the pump, and with random spectral phase) such that there exists a signal to amplify. These equations were numerically integrated through the 1 mm crystal (incorporating the phase introduced by the material), then the pulses were propagated through the cavity, incorporating the phase of the cavity length in vacuum and the phase of the output coupler. Initially, no atmospheric absorption was incorporated.

The result of this simulation is shown in Fig. 3.10. Signal and idler spectra are plotted at bottom as a function of wavelength and cavity detuning, and the corresponding pump depletions are plotted at top, also as a function of cavity detuning. Here, the typical features of a doubly-

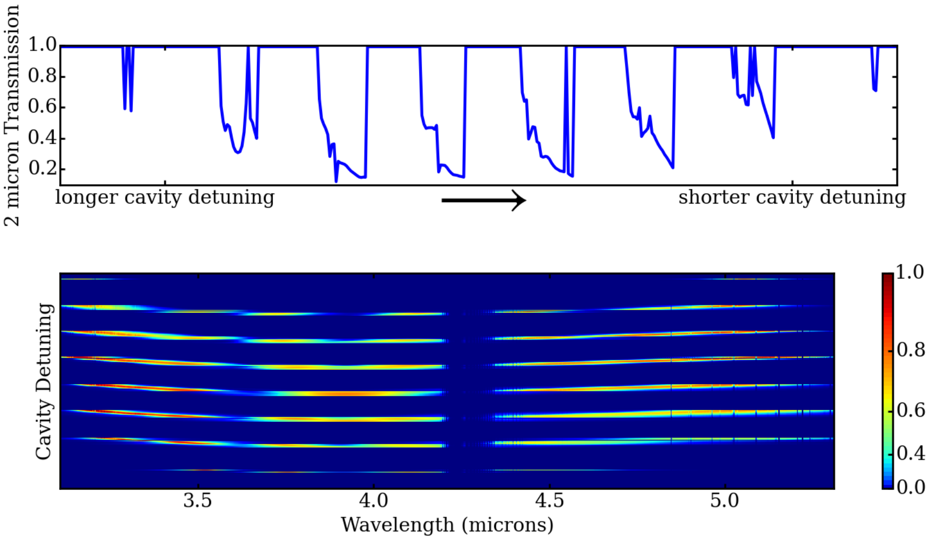

Figure 3.11: Simulation of OPO with atmospheric absorption. Generated spectra are shown at bottom, and corresponding pump depletions are shown at top. Compared to the simulation without absorption (Fig. 3.10), distinct gaps are seen in the idler spectrum at the strong carbon dioxide absorption feature near 4.2 µm, but the inclusion of absorption alone is unable to account for spectral gaps observed in experimental data.

resonant OPO are visible. Discrete bands of resonance occur, where the cavity supports an integer number of wavelengths of both the signal and idler. However, as the crystal has a varying index of refraction, a particular resonance for degenerate signal and idler can support non-degenerate signal and idler in a slightly shorter cavity. This produces the repeating rainbow pattern seen here. The absorption of the cavity, plotted in Fig. 3.9, can then also be introduced, and the result is shown in Fig. 3.11.

The strong atmospheric absorption at 4.3 µm in Fig. 3.9 is clearly visible as a vertical stripe in Fig. 3.11. However, this spectral hole is significantly narrower than that visible in the experimental data of both Figs. 3.6 and 3.7. This is because the absorption also induces strong dispersion, as a result of the Kramers-Kronig relations [138], which relates the real index of refraction (i.e., dispersion) to the imaginary index of refraction (i.e., absorption). The result of atmospheric dispersion is shown in Fig. 3.12. With the inclusion of both atmospheric absorption and dispersion, simulated spectra confirm the spectral window observed in experimental data.

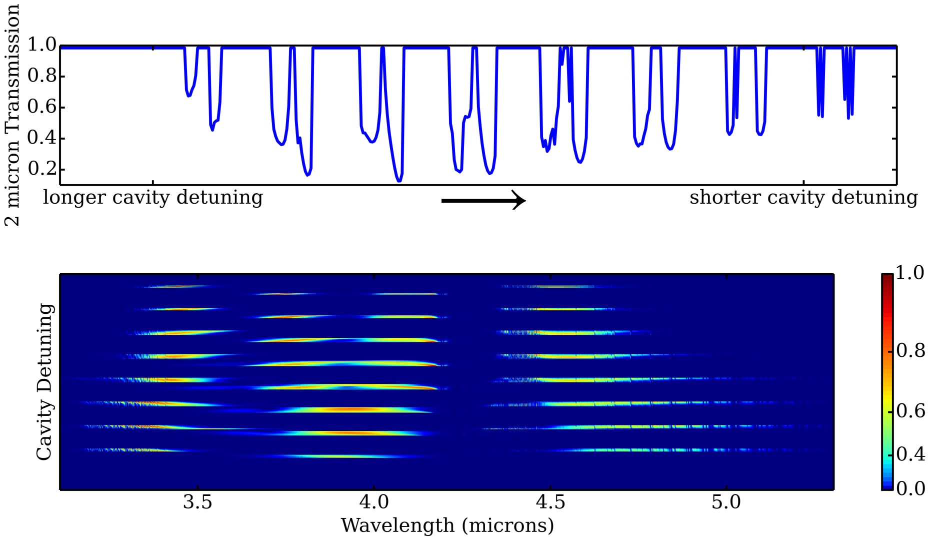

Figure 3.12: Simulation of OPO with atmospheric absorption and dispersion. Generated spectra are shown at bottom, and corresponding pump depletions are shown at top. With the inclusion of both absorption, the simulated spectral gaps match those observed in experimental data.

This agreement is more noticeable looking closely at a slice of a non-degenerate signal-idler pairing, shown in Fig. 3.13. Atmospheric dispersion narrows the spectra significantly.

3.5 Conclusions

This chapter demonstrated optical parametric generation of a broad spectrum of coherent mid-infrared light using a 2 µm fiber amplifier pump. The OPO uses an inexpensive nonlinear crystal, distinguishing it from some of the other nonlinear media used in similar work, and consequently shows potential for a commercially viable mid-infrared source. This OPO can be an incredibly useful tool as a spectrally broad mid-infrared source. More mature sources in this wavelength region can readily find applications in spectroscopy, medical diagnostics and therapies, biophysical and biomolecular research, environmental monitoring, defense and security, and optical communications [136].

However, a number of challenges presented themselves during its construction and operation. As was demonstrated in Sec. 3.4, atmospheric dispersion is a strong limiting factor in both bandwidth and spectral coverage. Additionally, the use of a 3-meter cavity required sensitive align-

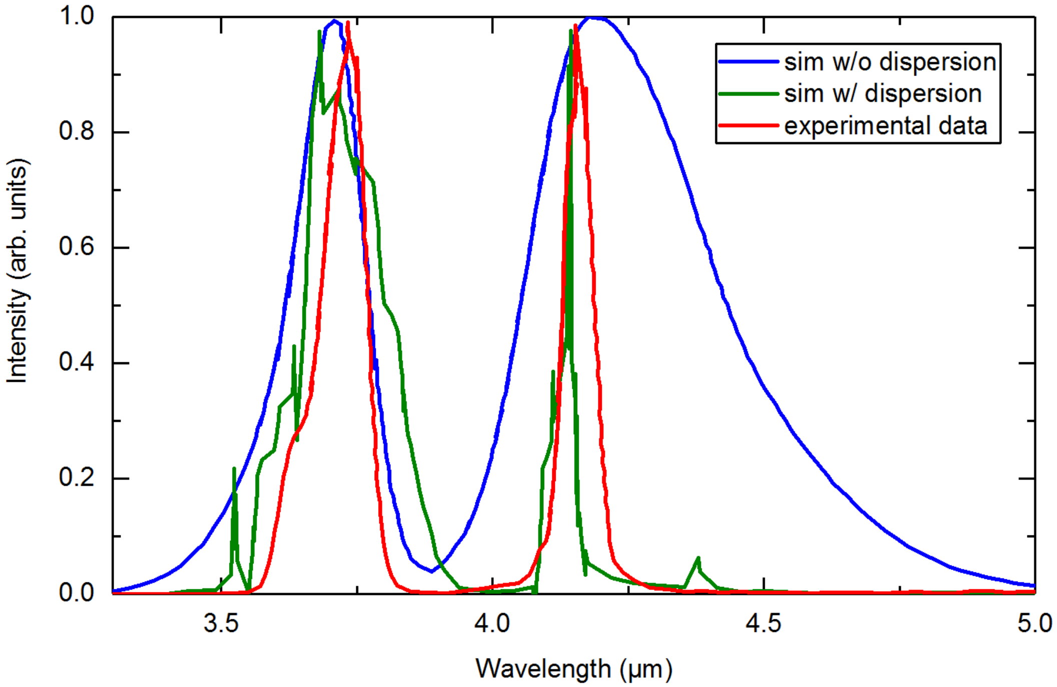

Figure 3.13: One particular resonance position, plotted for two simulated cases (with and without atmospheric dispersion, in green and blue, respectively), as well as experimental data from the same resonance position (red). The effect of atmospheric dispersion is strongly evident and causes the spectral narrowing seen in experimental traces.

ment and locking, which limited mid-infrared generation to a few minutes before cavity length drift required adjustment beyond the dynamic range of a piezoelectric mirror.

The final stability challenge arose from the use of non-polarization-maintaining fibers in the source, as described in [137]. Polarization rotation near the source caused both power and spectral fluctuations entering the high-power thulium amplifier and induced substantial instability in the system downstream. The challenges met during the project led to the search for both a more stable source and a more stable method of mid-infrared generation.

Chapter 4

Erbium-Doped Fiber Amplifier (EDFA) Development

4.1 Introduction

The stability challenges faced in the optical parametric oscillator (OPO) described in Chapter 3 led to the search for a solution to both problems: a more stable near-infrared source and a more reliable method of mid-infrared generation. This chapter describes the former: a systematic method of designing and constructing erbium-doped fiber amplifiers (EDFAs) based solely on polarization-maintaining (PM) fiber for optimally short pulses. A substantial amount of research has already been conducted in the development of short pulses and spectral broadening based on erbium-doped fiber oscillators [101, 102, 139, 140]. This chapter surveys a variety of techniques to generate high peak power pulses at 100 MHz in PM fiber in order to achieve optimal short- and long-term stability. After showing that the previously successful design at 250 MHz [102] does not work at 100 MHz, this chapter also explores several other amplifier designs (pre-chirping the pulse dispersion-compensating fiber, compression in large-mode-area fiber, compression using a pair of silicon prisms) that were ultimately also unsuccessful. Numerical modeling was then implemented in order to understand and predict pulse dynamics, which elucidated previous failed designs and, after determining that input spectral bandwidth was a critical factor, guided a more successful design strategy. Lastly, this chapter discusses two configurations that worked reliably, presented in Secs. 4.5 and 4.6. The parts used in EDFA construction are listed in Sec. B.2.

For nonlinear processes, the shortest possible pulse is important for several reasons. First, high peak power boosts nonlinear down-conversion (see Sec. 2.3), as the evolution of the idler wave

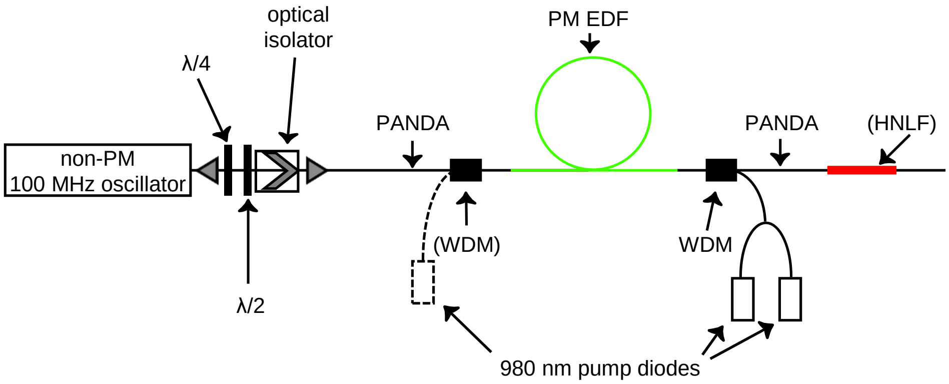

Figure 4.1: Schematic of a typical EDFA. Light from a non-PM oscillator is linearly polarized using quarter- and half-wave plates, and, after passing through an optical isolator, is coupled into PANDA (polarization-maintaining anomalous-dispersion single-mode fiber). The pulse is stretched in a short section of PANDA fiber, amplified in normal-dispersion erbium gain fiber while stretched to avoid pulse break-up, then compressed in PANDA before exiting the amplifier. Pump power is coupled into the amplifier using either one or two wavelength-division multiplexers (WDMs) using either two or three pump diodes. The output of the EDFA may be spectrally broadened to new wavelengths using highly nonlinear fiber (HNLF). Specific parts shown in Sec. B.2.

depends upon on the field strength of the pump. Second, a compressed pulse experiences nonlinear spectral broadening as seen in Fig. 2.7, allowing for broader bandwidth after down-conversion in the mid-infrared wavelength region.

4.2 EDFA Design

The objective in EDFA design is to eliminate the anomalous chirp from an oscillator in normal-dispersion erbium gain fiber at low peak power, achieve high peak power while normally chirped, then eliminate the chirp again and compress the pulse in anomalous-dispersion fiber before launching into free space. A typical schematic for an EDFA based on a commercial non-PM erbium fiber oscillator is shown in Fig. 4.1. As this particular oscillator is not PM, the light must be polarized along one of the PM fiber's axes before being coupled into PM fiber. A short section of non-PM SMF (single-mode fiber) connects the oscillator to a free-space bench where the fiber output is collimated, the polarization is made linear (using a quarter-wave plate) and rotated (using a half-wave plate) before passing through a free-space isolator (to prevent back-reflections from altering the mode-locked state). The light is then coupled into PANDA (PM, anomalous-dispersion, single-mode fiber). PANDA is spliced to 0.7–1.4 m of normal-dispersion erbium gain fiber (the range of lengths needed for maximum pump absorption without a loss of signal power), which is spliced to an additional section of PANDA. There are two possible configurations, depending on the desired output power. 200 mW of output power entails two pump diodes, with a single wavelength-division multiplexer (WDM) used to backward-pump the gain fiber. In order to achieve 300 mW of output power, three pump diodes are required, which entails two WDMs for forward and backward pumping with three total pump diodes. (The higher power configuration is shown in the figure using dashed lines.) The pulse power increases roughly linearly along the gain fiber, from low tens of mWs after the polarization optics to 200–300 mW entering free space after the amplifier. A listing of the specific parts used is shown in the appendix, in Sec. B.2.

As a result of high intensity, the contribution of the nonlinear refractive index (Sec. 2.4) becomes proportionally stronger and the pulse behaves quite differently in each section of PANDA, despite having identical anomalous dispersion. Strong nonlinearity from high peak power within fiber can cause pulse break-up, which in turn means a substantial loss of peak power. Another important reason to maintain high pulse quality is to improve the agreement of numerical modeling with experimental demonstrations. Pulse breakup precludes this.

4.3 Approaches to EDFA Pulse Compression

4.3.1 EDFA Design at Higher Repetition Rates

The input to previous amplifier designs used the direct output of the commercial erbium fiber ring oscillator, the amplitude and phase of which was measured using frequency-resolved optical gating (FROG) [141]. The comb's output is a low-power (30 mW), strongly chirped pulse (26000 fs^2 after compression in 50 cm of SMF-28), the spectral and temporal profile of which are shown in Fig. 4.2. This initial amplifier design mimicked what had previously been successful in EDFAs at higher repetition rates (200 and 250 MHz); the targeted fiber lengths were 105 cm of PANDA

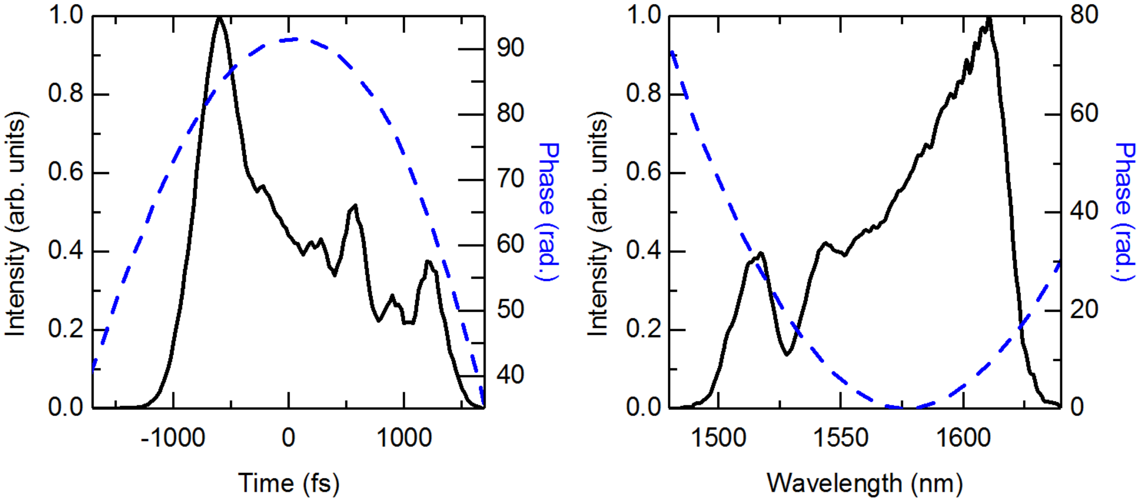

Figure 4.2: Left: temporal profile of the pulse used in numerical simulations, measured using frequency-resolved optical gating (FROG). The amplitude is shown in solid black (left axis) and the phase is shown in dashed blue (right axis). Right: spectral profile. The amplitude is shown in solid black (left axis) and the phase is shown in dashed blue (right axis).

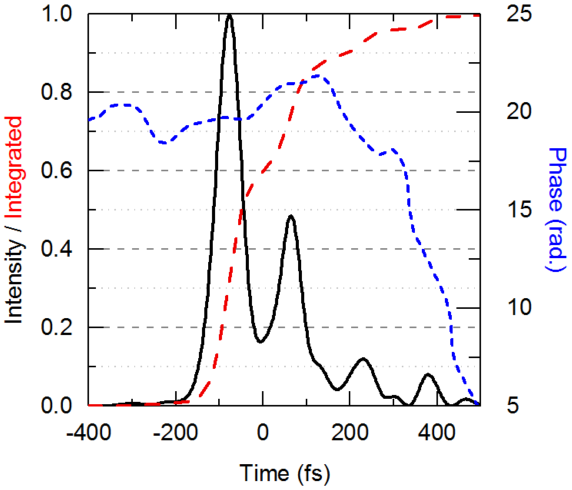

Figure 4.3: The optimal output of traditional amplifier design as shown in Fig. 4.1. The pulse is plotted in solid black as delay vs. normalized intensity, the integrated intensity is plotted in long red dashes, and the corresponding temporal phase is plotted in short blue dashes. With 350 mW of average power, this resulted in 26 kW peak power, with a duration of 70 fs FWHM and 60% of energy in main pulse.

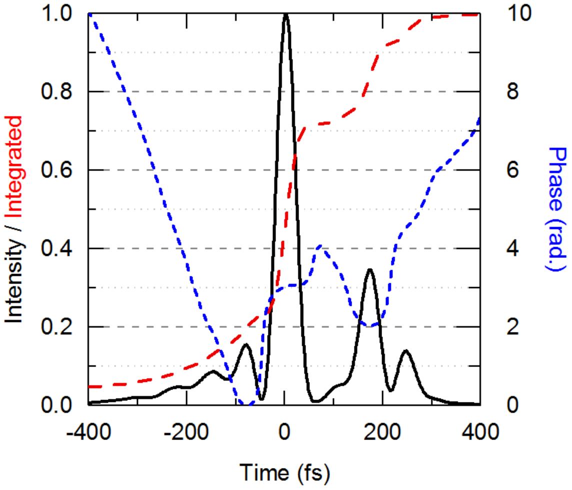

Figure 4.4: Use of 65 cm of dispersion-compensating fiber (DCF) before fiber bench and 85 cm of PANDA after in order to compensate for excess DCF. With 300 mW of average power, this resulted in 31 kW of peak power, with a duration of 40 fs FWHM and 50% of energy in the main pulse.

after the free-space polarization optics, 130 cm of PM EDF, and 50 cm of PANDA to compress the pulse before launching into free space. In order to achieve 300 mW of average power, the design implemented two WDMs with three total pump diodes, in a similar configuration to the successful designs implemented in other EDFAs at higher repetition rates.

The results of the optimized configuration are shown in Fig. 4.3. The pulse has two peaks, meaning only a fraction of its total energy is in the main peak. Since a design that reliably provided a high-energy, low-duration pulse at higher repetition rates was unable to achieve short pulse durations after optimization at 100 MHz, these results provided an indication that typical designs were insufficient at 100 MHz and a new strategy was required. This is because, for the same average power, a 100 MHz pulse will have double the pulse energy as a 200 MHz pulse, and thus the pulse dynamics will be substantially different.

4.3.2 Dispersion-Compensating Fiber

The first attempted technique to prevent the pulse breakup from the previous EDFA design was the introduction of dispersion-compensating fiber (DCF), a small-core fluoride fiber with strong normal dispersion (roughly -5 times that of SMF-28). There were two reasons for considering this solution. First, DCF was used in a previously successful design at the same repetition rate in the non-PM amplifier in the Chapter 3 design (from Ref. [137]). As the designs that succeeded at higher repetition rates did not work here, a similar design to that used at the same repetition rate might be expected to be more successful. Second, based on the breakup problems seen in Sec. 4.3.1, a chirped pulse design where high peak powers do not occur until the final compression stage might be able to avoid acquiring this undesired nonlinear phase.

Both the length of DCF used and the amount of PANDA used to compress were optimized, and the result is shown in Fig. 4.4. This design uses 65 cm of DCF, 85 cm of PANDA added before the amplifier to compensate for some of the excess DCF, and none added after the amplifier. Although the achieved pulse duration was shorter than that in Fig. 4.3, half the pulse energy remained in the central peak, with the remaining energy in secondary peaks and its broad pedestal. Despite strong chirping of the pulse during amplification, the pulse still compressed in small-core PANDA, and, as a result, enough nonlinear phase was acquired that the output pulse shape was distorted significantly from an ideal Gaussian or secant pulse.

4.3.3 Large Mode Area Fiber

The findings from the study of DCF showed that a chirped input into an amplifier will not work at 100 MHz as long as the pulse is still being compressed in traditional single-mode fiber. The pulse compression problems evident using chirped-pulse amplification indicated the need for compression in a minimally nonlinear medium. In fiber, this can be done in large mode area (LMA) fiber, which has similar dispersion properties as SMF (both are silica fibers), but, because of a larger core, the beam is less confined, and thus has a lower intensity for a given power. (The part number

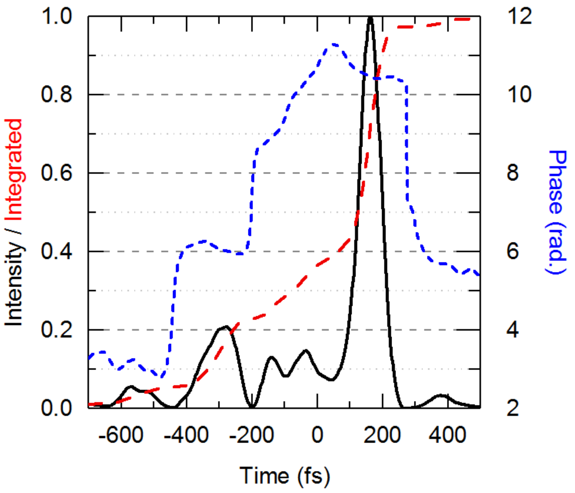

Figure 4.5: Compression using large mode area (LMA) fiber. With 270 mW of average power, this resulted in 18 kW of peak power, with a duration of 80 fs FWHM and 50% of energy in the main pulse.

is provided in the appendix, in Sec. B.2.) The pulse shape after optimizing the configuration's fiber lengths is shown in Fig. 4.5. Optimization involved splicing the amplifier output to a spool of LMA, acquiring FROG spectrographs for three different amplifier outputs (using one, two, or three pump diodes in the amplifier), cutting back fiber in 5–10 cm increments, and re-measuring until the LMA length featuring optimal compression was found. This design compressed in 2.3 m of LMA fiber, with 270 mW propagating in the LMA after splice losses to the amplifier output. An asymmetric pedestal is visible, a product of third-order dispersion, most notable after the second-order dispersion has been corrected. The output pulse here has significant power in a single-sided pedestal, and, as a result, half of the power was in the central peak, with little improvement from earlier configurations.

4.3.4 Silicon Prism Pair

Another method to remove second-order dispersion while avoiding nonlinear effects involves launching the beam into free-space and correcting the dispersion using a pair of silicon prisms.

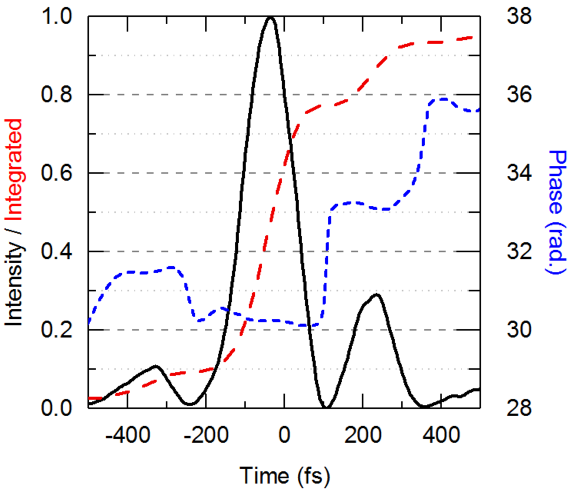

Figure 4.6: Compression using a pair of bulk silicon prisms. This resulted in a duration of 140 fs FWHM and 65% of energy in main pulse. Because compression using silicon prisms is lossy, average power and peak power were not measured.

While bulk silicon is normally dispersive at 1.5 µm, a dispersed beam from a pair of silicon prisms can experience anomalous dispersion as a function of the prism separation [142]. The group delay dispersion introduced by a prism compressor is given by:

$$GDD_{\mathrm{PRISM}} = \frac{\lambda^3}{2\pi c^2}\left[-4l\left(2\left(\frac{\mathrm{d}n}{\mathrm{d}\lambda}\right)^2\right)+4\left(\frac{\mathrm{d}^2n}{\mathrm{d}\lambda^2}\right)\left(2D_{1/e^2}\right)\right] \tag{4.1}$$

where l is the apex separation of the two prisms and D is the beam diameter at $1/e^2$ [143].

The best pulse shape achieved via this technique is shown in Fig. 4.6. The third-order dispersion mismatch was reduced compared to Fig. 4.5, but is still present. The percentage of power in the central peak was increased from 50% to 65%, but a substantial improvement from earlier techniques did not occur.

4.4 Simulation Testing

4.4.1 Design Confirmation

After a chirped input and two low-nonlinearity compression techniques were tested and did not work, the pulse behavior was numerically modeled in order to understand why these designs were unsuccessful and to guide future designs. The framework for this was established in Sec. 2.4, and shown to be successful for the more complicated interactions that pulses experience in fiber. The input was the FROG retrieval of the comb output after 50 cm of SMF shown in Fig. 4.2. Gain was modeled by incorporating a linear increase in average power through the length of EDF.

The simulation served two purposes: (i) exploring the parameter space of the original and DCF-stretched inputs with various PANDA and EDF fiber lengths, without having to rebuild the system (for varying EDF) or disconnect and re-connect fiber patch cords (for varying input PANDA), and (ii) understanding the nature of pulse breakup and to explore alternative options to see if a better output pulse was attainable.

The result of the simulation is shown in Fig. 4.7, where the pulse's spectral intensity is plotted at left as a function of wavelength and fiber length, and its temporal intensity is plotted at right as a function of delay and fiber length. This particular case uses 40 cm of PANDA before the erbium-doped fiber (EDF) and 100 cm of gain fiber; however, in the design process, a matrix varying these initial parameters was tested, ranging from 20 (the minimum amount of input fiber allowable in the initial design) to 70 cm of initial PANDA and 100 (the minimum amount required to provide adequate gain) to 180 cm of EDF in steps of 5 cm. In the simulation, the final section of PANDA was made to extend past the point of maximum compression so that the pulse would be guaranteed to reach its shortest duration and highest peak power and disperse within the simulation parameters. Where the highest peak power occurred, the resulting pulse shape and spectrum were retrieved as the optimal output fiber length for a given configuration. This "slice" for the simulation in Fig. 4.7 is shown in Fig. 4.8. This was done for the entire matrix of input lengths, each of which were studied.

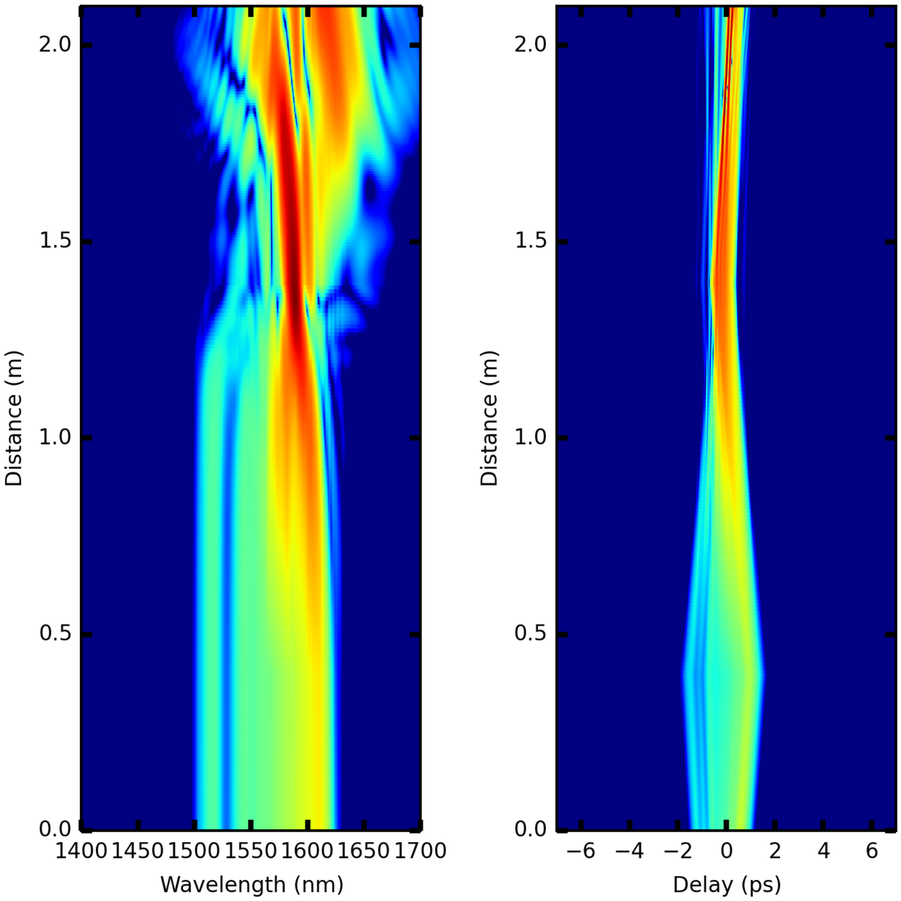

Figure 4.7: Simulation of an EDFA using the measured spectrum and phase of the fiber oscillator as the input. The pulse's spectrum as a function of propagation length is plotted at left, and the pulse's temporal shape is plotted as a function of propagation length at right. The three sections of fiber are evident in the temporal plot as the dispersion flips from anomalous in PANDA (0–0.4 m) to normal in EDF (0.4–1.4 m) and back to anomalous (1.4–2.1 m). At left, nonlinear broadening is evident beyond 1.4 m as the pulse shortens and the nonlinear refractive index strongly affects the pulse's behavior.

The pulse's evolution is evident in the temporal plot; the pulse stretches in the anomalous dispersion fiber, compresses and stretches again while being amplified in the normal-dispersion gain fiber, and compresses while experiencing strong nonlinear effects in the final section of anomalous dispersion fiber. When the pulse becomes sufficiently short and acquires enough power, the spectrum broadens beyond the initial seed spectrum, as seen at 1.4 m and beyond in the left plot.

Based on these simulations, the observed behavior was confirmed: the amplifier was unable

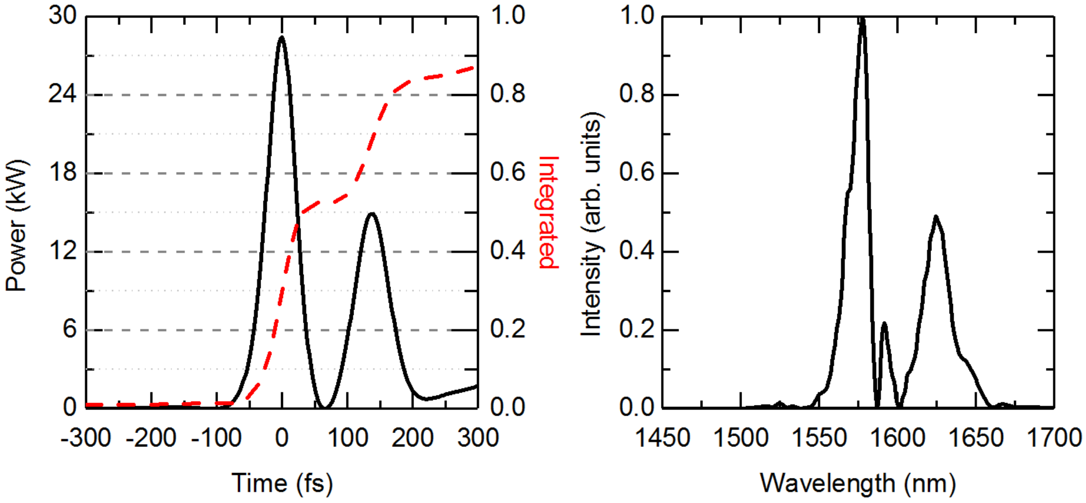

Figure 4.8: Slice of spectrum and pulse at the shortest pulse duration from the simulation in Fig. 4.7, at 1.87 m. The maximum peak power was 28 kW, and the shortest pulse duration was 67 fs (measured as the full-width at half-maximum).

to generate a pulse with a high fraction of power in the main pulse. However, since the model was able to generate behavior similar to that observed experimentally, the input could be altered to explore other design alternatives.

4.4.2 Exploring Other Options

The search for a better design was heavily driven by the work of Ref. [144], where the authors were able to achieve short pulses with high peak power and a minimal pedestal at a sub-100 MHz repetition rate. In investigating the differences between configurations, the only substantial difference between experimental setups was the input bandwidth — the Menlo oscillator used here was significantly broader. Armed with this hypothesis, our simulations were repeated while emulating a narrower input, here a chirped hyperbolic secant (sech) pulse (see Fig. 4.9).

The results of the simulation are shown in Figs. 4.10 and 4.11. Significantly higher peak power is demonstrated as compared to Figs. 4.7 and 4.8, as well as shorter pulse durations and more power in the primary peak. The deleterious effects of a broader input spectrum are counter-intuitive;

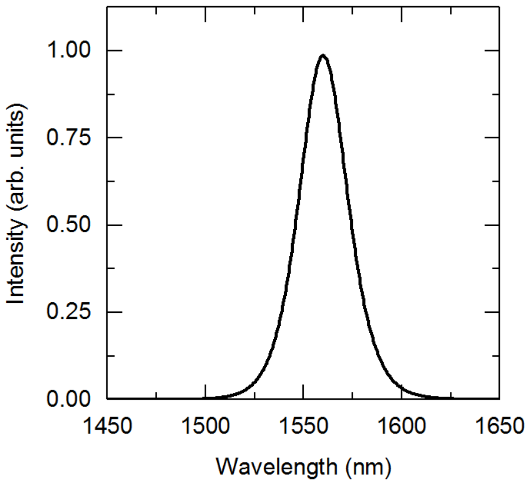

Figure 4.9: Computed spectrum of the narrower hyperbolic secant (sech) input used in modeling an alternative amplifier design.

essentially, the broad, uneven spectrum of the comb does not behave uniformly as it evolves through the amplifier, whereas the narrower spectrum of the sech pulse does. These promising results provided experimental guidance for better amplifier design.

4.5 Bandpass Filtering

As the comb output is already strongly chirped, a spectral shape similar to that seen in Fig. 4.9 could be achieved through spectral filtering. A 45 nm FWHM bandpass filter was introduced in the fiber bench, and the resulting pulse shape is shown in Fig. 4.12. With lower pump power, high peak power, short pulse duration, and a clean (minimal pedestal) shape was able to be achieved. This is the design that was implemented for much of the EDFA implementation described in later chapters; the successful experiment design featured 60 cm of PANDA and 68 cm of PM EDF before compressing in PANDA.

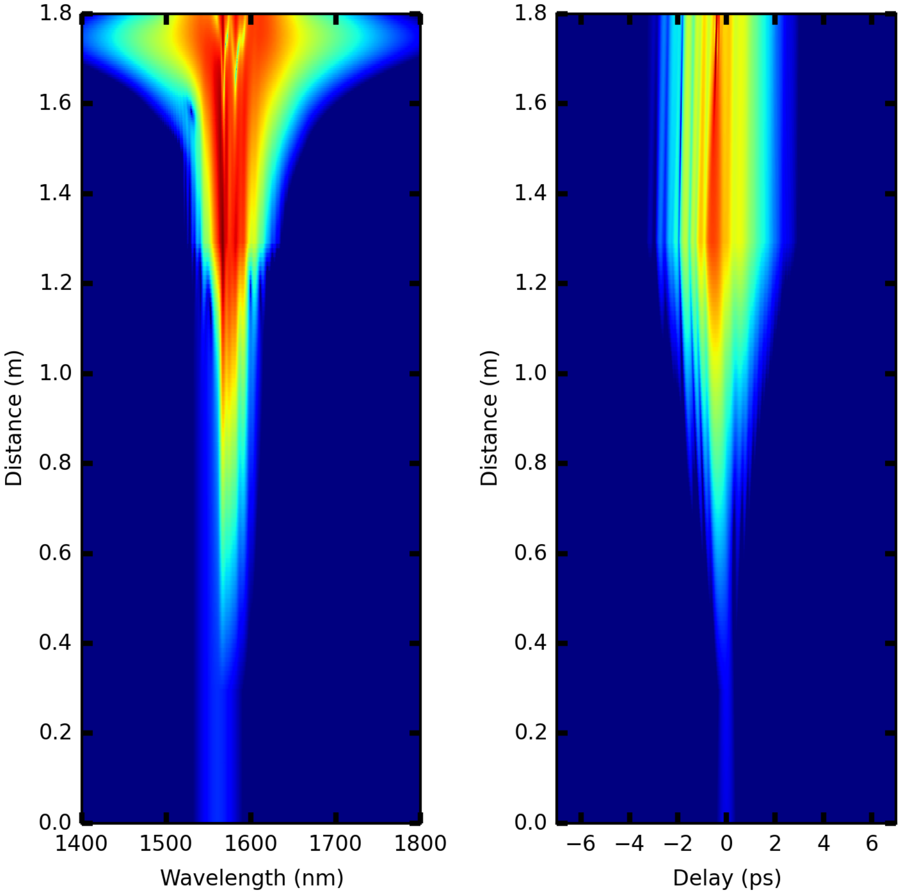

Figure 4.10: Simulation of an EDFA using a hyperbolic secant (sech) pulse with 25000 fs^2 of chirp on a 50 fs pulse. The design used 30 cm of PANDA followed by 100 cm of EDF. Despite a spectrally narrower input, the resulting short pulse has a substantially broader spectrum and a shorter pulse duration than that simulated using the FROG-measured comb input.

4.6 PANDA Minimization

An additional discovery determined via simulation was that clean, high-power pulses similar to those achieved via spectral filtering could also be realized with very short input fiber lengths. For added stability and fiber protection, all amplifiers were assembled in metal boxes, with the fiber ferrules screwed into panel-mounted mating sleeves. The mating sleeves were then connected to buffered fiber patch cords, which led to either the output of the comb, the pump, or a collimator to launch into free space. In order for this design to be achieved, the amplifier was constructed

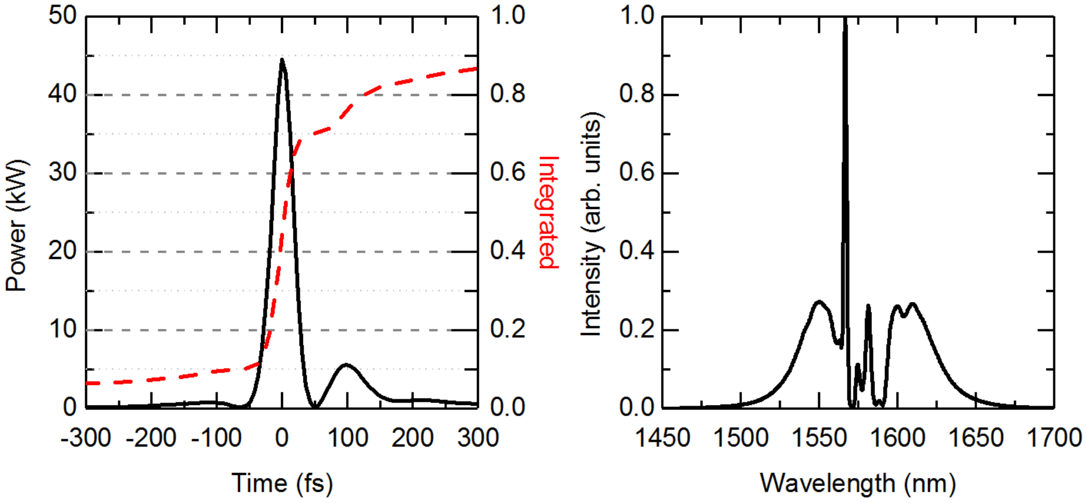

Figure 4.11: Slice of spectrum and pulse using the sech input pulse from the simulation in Fig. 4.10 at the shortest pulse duration, 1.74 m. The maximum peak power was 45 kW, and the shortest pulse duration was 37 fs.

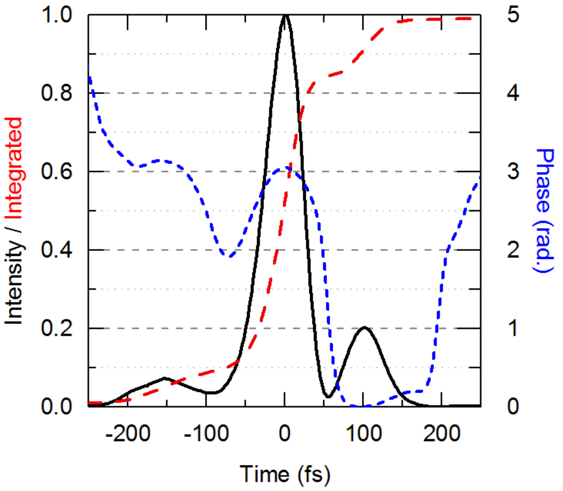

Figure 4.12: The experimental results using a bandpass-filtered comb output as the amplifier input. With an average power of 220 mW, the amplifier generated 50 fs pulses with 27 kW of peak power and 75% of energy in main pulse.

entirely in the open, so the fiber length before the EDF could be as short as possible, essentially the minimum length necessary to splice the PANDA fiber to the EDF. The results of this configuration

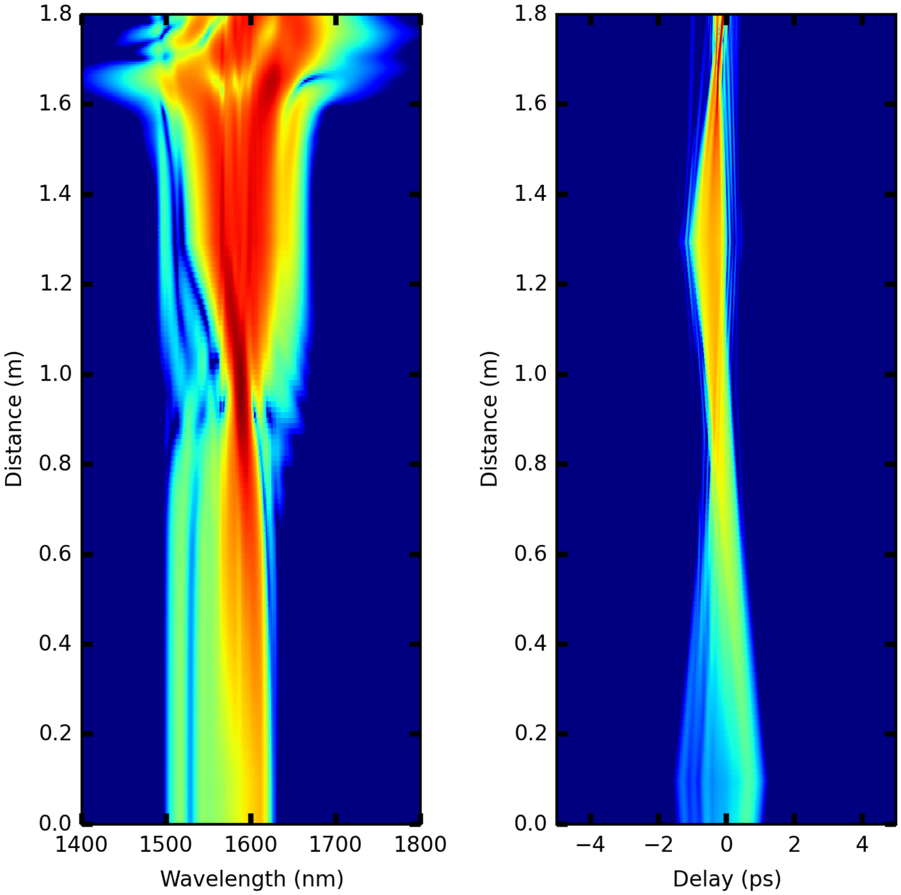

Figure 4.13: Simulation of an EDFA using the measured spectrum and phase of the fiber oscillator as the input and minimal PANDA length before the gain fiber (EDF). Only 0.1 m of PANDA was used before 1.2 m of EDF. The highest peak power occurred at 1.67 m.

are plotted in Figs. 4.13 and 4.14. This design proved to be immensely successful experimentally, in addition to a bandpass filter configuration. The successful design implemented here used 12 cm of PANDA (after 20 cm of internal fiber from the Menlo comb had been removed) and 82 cm of PM EDF before compressing in PANDA. An example of such a system is shown in Fig. 4.15.

4.7 Conclusion

This chapter has detailed the successful search for a method of generating high-power pulses to drive nonlinear processes in erbium-doped fiber amplifiers at 1.5 µm. The system implemented

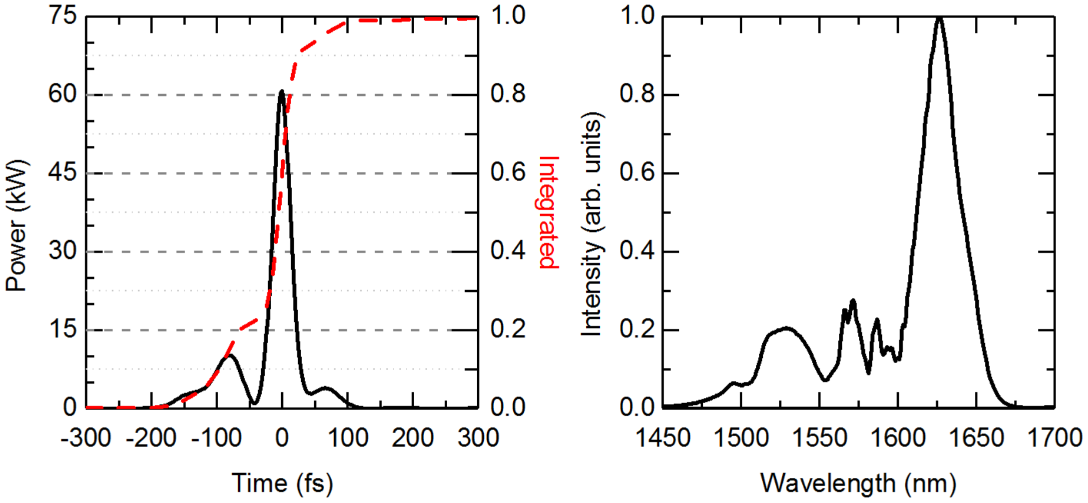

Figure 4.14: Slice of spectrum and pulse using minimal PANDA before the EDF from Fig. 4.13 at the shortest pulse duration, at 1.67 m. The maximum peak power was 61 kW, and the shortest pulse duration was 32 fs.

in subsequent chapters incorporated both successful designs; one branch of the MenloSystems difference frequency generation system used a bandpass filter, while the other featured a short initial fiber length. As a result of this careful design, the amplitude noise of these systems was quite low, and is characterized in later chapters (Secs. 5.2 and 6.4.5 in the context of comparison to mid-infrared relative intensity noise (RIN).

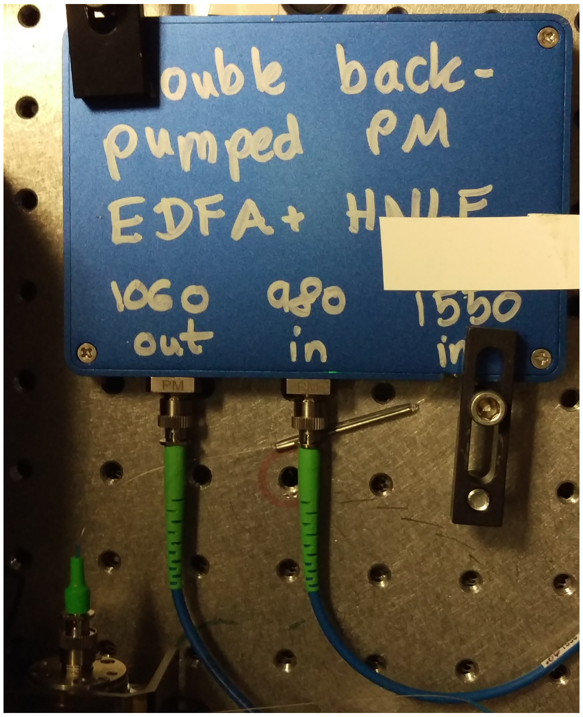

Figure 4.15: Image of a packaged EDFA with short fiber lengths. The output of the polarization optics (bottom left) is connected via a short section of PANDA fiber to PM EDF at the splice protector (barrel-shaped component, middle). This particular amplifier uses one WDM and is pumped exclusively backwards with two pump diodes; the pump light is coupled in at a connector (labeled "980 in"). The amplifier's output is spliced internally to highly nonlinear fiber (HNLF), the output of which is sent to a ytterbium-doped fiber amplifier from the "1060 out" port.

Chapter 5

Difference Frequency Generation at 3 Microns

5.1 Introduction

Using the results from Chapter 4, polarization-maintaining sources in the near-infrared region were available with substantial high peak power, suitable for free-space nonlinear optical processes. Because of the stability challenges faced in the OPO (Chapter 3), a single-pass solution was optimal, as exhibited in the cartoon in Fig 5.1. Difference frequency generation (DFG), described in Sec. 2.3, is a nonlinear process that describes single-pass nonlinear conversion using two inputs: a pump (which gets depleted), and a signal (which experiences parametric gain). This is free from the path length and alignment requirements for a cavity, and only requires that the input pulses are temporally overlapped. This chapter describes the generation of mid-infrared frequency combs, produced through DFG, near 3 µm, and their implementation in dual comb spectroscopy. This work has been detailed in Ref. [51].

The generated combs achieved powers in excess of 500 mW, the spectra of which extended from 2.8 µm to 3.5 µm. This spectrum overlaps with a relatively transparent window in the atmosphere and was well-suited to observe fundamental bands of acetylene, methane, propane, ethane, and other hydrocarbons. The DFG was characterized by strong pump depletion and significant parametric signal gain. Absorption spectra of acetylene and methane (recorded in grating spectrometers), along with interferograms obtained by heterodyning two combs, demonstrated good amplitude and phase noise properties of the combs.

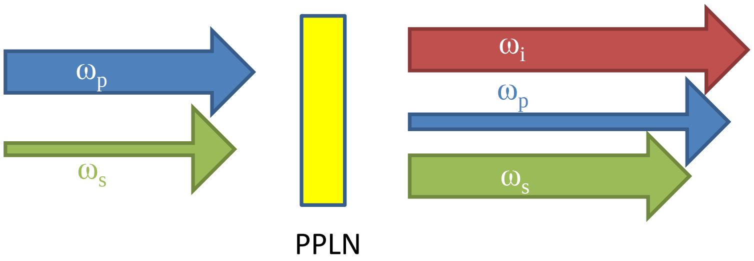

Figure 5.1: Diagram depicting the difference frequency generation process. Pump (ω_p) and signal (ω_s) photons are focused into a periodically-poled lithium niobate (PPLN) crystal, depleting the pump, generating the idler (ω_i), and creating parametric gain in the signal.

5.2 Design and Characterization

The schematic diagram of one of the MIR DFG OFCs and setup for multiple heterodyne spectroscopy are presented in Fig. 5.2, which is similar in design to those of Refs. [4, 5, 14, 24]. One advantage of DFG-generated OFCs is the cancellation of the carrier-to-envelope offset frequency (f_{ceo}) when the two wavelengths are coherently derived from the same femtosecond oscillator. The system started with a home-built Er-doped fiber femtosecond oscillator based on nonlinear polarization rotation mode-locking, providing 20 mW of average output power at a repetition rate of 100 MHz. All subsequent components employed polarization-maintaining (PM) fibers and amplifiers, which were verified to provide better stability and robustness, as compared to previous MIR comb generation systems based on non-PM fibers (Chapter 3). The laser output was split into two branches with one being amplified in two EDFAs. The amplified signal beam extended from 1510 nm to 1625 nm with up to 140 mW of average power and pulses of 60 fs, measured using an autocorrelator and FROG [141]. The fiber lengths used in this EDFA are described in Chapter 4. The other branch was spectrally broadened to produce a few milliWatts of light around 1050 nm (50 nm bandwidth) using 3 cm of PM highly nonlinear fiber (D = 5.6 ps/nm/km at 1550 nm) [101, 102]. These pulses were pre-amplified in a Yb-doped fiber amplifier (YDFA) and temporally stretched to near 50 ps using a few meters of fiber with negative third-order dispersion. The pulses were then sent to a high power YDFA, which used a double-clad Yb PM fiber, pumped

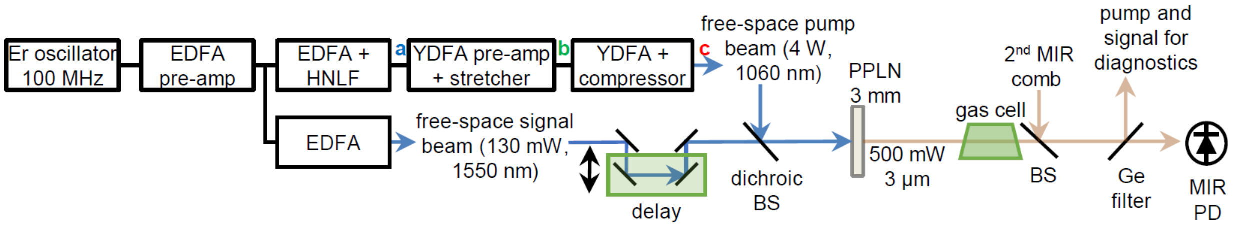
Er oscillator
100 MHz
EDFA
pre-amp
EDFA +
HNLF
a
YDFA pre-amp
+ stretcher
b
YDFA +
compressor
c
free-space pump
beam (4 W,
1060 nm)
EDFA
free-space signal
beam (130 mW,
1550 nm)
delay
dichroic
BS
PPLN
3 mm
500 mW
3 µm
gas cell
2nd MIR
comb
BS
pump and
signal for
diagnostics
Ge
filter
MIR
PD

Figure 5.2: Schematic diagram of the MIR DFG comb and heterodyne spectroscopy setup. Boxes are connected via fiber and the color lines represent free-space beams. Lenses (not shown) are used to expand the beams and focus them into the PPLN crystal. EDFA: erbium-doped fiber amplifier, YDFA: ytterbium-doped fiber amplifier, MIR PD: mid-infrared photodetector, Ge filter: germanium window, acting as a low pass optical filter, BS: beamsplitter, PPLN: periodically-poled lithium niobate crystal, HNLF: highly nonlinear fiber. Specific part numbers are provided in Appendix B.

by two diode lasers (976 nm) with up to 8 W each, followed by a fiber-coupled optical isolator. A free-space pulse compressor with two transmission gratings produced a pump beam which extended from 1025 nm to 1070 nm, with 210 fs minimum duration pulses and average power up to 4 W. Part numbers for the aforementioned parts are listed in the appendix in Secs. B.3 and B.4. The signal (centered at 1567 nm) and pump (centered at 1048 nm) beams were spatially expanded, and focused in a 3-mm-long MgO-doped periodically-poled lithium niobate (MgO:PPLN) crystal. The crystal length was chosen because it was the longest crystal length commercially available at the time of experimental design. A delay line stage was used to adjust the temporal overlap of the two pulses, but it was not actively controlled.

The MgO:PPLN crystal (details provided in the appendix, in Sec. B.6) was AR-coated for the pump, signal and idler beams; and had five gratings with periods varying from 29.98 µm to 31.59 µm. Each period can generate DFG but with different central wavelength, spectrum and power. The PPLN crystal, placed in an oven, was operated near 150 °C in order to optimize phase-matching and minimize the photorefractive effect. However, the MIR generation was not critically sensitive to temperature. Phase matching was achieved for $e + e \to e$ polarizations with effective nonlinear coefficient $d_{\text{eff}} = 14.9$ pm/V. Non phase-matched colors in the green (523 nm — second harmonic generation of the pump), red (628 nm — sum frequency generation: $f_{\text{pump}} + f_{\text{signal}}$), and

UV (393 nm — $2f_{\text{pump}}+f_{\text{signal}}$; 349 nm — third harmonic generation of pump) were also generated, and the red beam was used as a guide for initial mode-matching and temporal overlap of the signal and pump pulses. The pump and signal waist sizes in the crystal were adjusted to near 50 µm and 70 µm, respectively, leading to confocal parameters larger than the crystal length, which was close to optimum, as was determined in the subsequent group velocity walkoff calculation. The beam waist sizes were chosen to keep the intensity below the manufacturer's stated damage threshold limit of about 4 GW/cm^2, and at the same time allow the use of most of the available pump power. A second MIR OFC was constructed with a similar design and was based on a commercial Er-doped fiber oscillator. The pump and signal beams were filtered out either after the PPLN or the gas cell using a germanium filter that transmits 90 % of the MIR idler beam, which was then combined in a 50/50 CaF_2 beamsplitter with the beam from the other comb. The combined beams from one beamsplitter port went to a MIR Peltier-cooled pre-amplified HgCdTe photodetector (100 MHz bandwidth) and the other was used for diagnostics. Commercially available gas cells were placed in the path of one of the MIR DFG combs for spectroscopy (Fig. 5.2).

Fig. 5.3 shows the MIR power of the first comb built as a function of pump power at 1050 nm for a signal input power of 130 mW. Over 500 mW was generated in the MIR, a power more than three times higher than what has been previously reported for DFG combs [14, 24]. This was a result of tight focusing, careful mode overlap optimization, and higher available pump power. Relatively good power stability was verified for periods of a few hours, with a fractional standard deviation of 3.5 % (Fig. 5.4). This was determined by measuring the average power every minute over several hours and computing the standard deviation. To our knowledge, this is the first power stability measurement performed over this time span for a DFG comb system. The variation arose from temperature- and pressure-driven changes in the optical path lengths, neither of which were environmentally isolated. Data from the previous comb based on non-PM fibers shows considerably higher power instability over a few minutes due to drift on the temporal overlap between the pump and signal pulses. Fig. 5.5 shows an autocorrelation trace of the higher power MIR pulses, from which a duration of 70 fs is estimated.

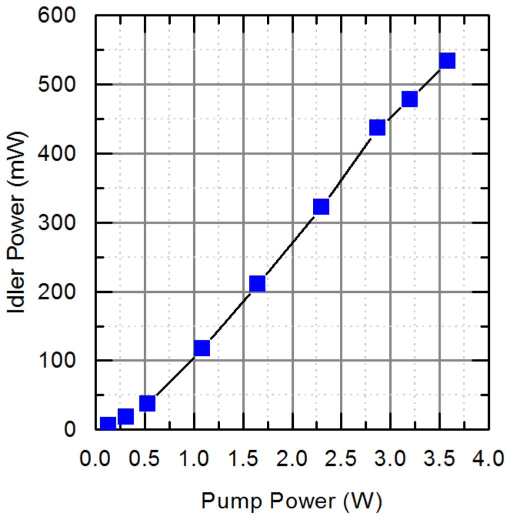

Figure 5.3: MIR power (corrected for 90 % transmission of the Ge filter) as function of pump power at 1050 nm, for a signal input power of 130 mW at 1567 nm.

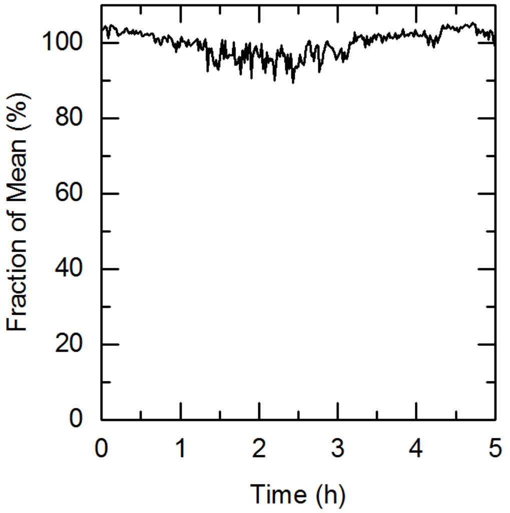

Figure 5.4: MIR power stability plot, for PM-fiber-based MIR comb without environmental noise isolation.

Fig. 5.6 shows the relative intensity noise (RIN), which can severely impact the SNR of the interferograms in dual-comb spectroscopy, measured for the pump, signal and idler beams. RIN from the oscillators can be increased by the several stages of amplification and by supercontinuum

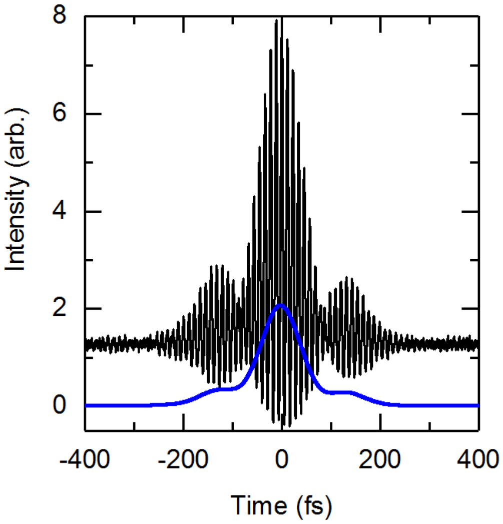

Figure 5.5: Interferometric (black) and intensity (blue) autocorrelation traces for the MIR pulses.

generation. The fiber lengths in the amplifiers were optimized to minimize both the RIN and the pulse duration, as a short pulse provides optimum broadening and maximizes the power at the relevant wavelengths. In Fig. 5.6, RIN for the pump and signal beams was measured before and after the PPLN crystal. RIN for the pump beam, measured before the PPLN crystal, was in fact quite higher than for the signal beam. After the crystal, RIN for the signal beam, the parametric amplification of which under DFG can be seen as from mixing of the idler and pump beams, increased by acquiring the noise from the pump beam. RIN for the idler beam shows a similar level, which is therefore presently determined by the supercontinuum generation and amplification stages that produced the pump beam. The roll-off is due to the 500 kHz bandwidth of the amplifier used with the MIR photodetector. RIN for the previous comb based on non-PM fibers was higher, although this was not investigated in detail.

An indirect measurement of the coherence of the combs was also obtained by heterodyning both pump and signal pulses with narrow-linewidth ($\approx$ 1 kHz), single-frequency cw lasers at 1.0 µm and 1.5 µm. Beat notes with SNR near 40 dB and 10 kHz width were obtained (recorded at a resolution bandwidth (RBW) of 1 kHz and a sweep time of 0.2 s), indicating good coherence for

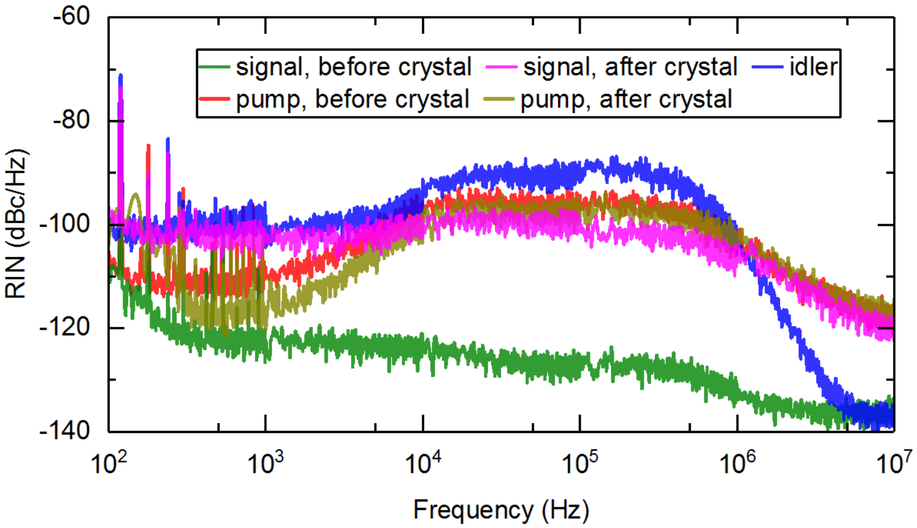

Figure 5.6: Relative intensity noise (RIN) for the pump, signal and idler beams. RIN for the pump and signal beams has been measured before and after the PPLN crystal (under DFG).

those beams after amplification.

Spectra obtained for one of the MIR combs are presented in Figs. 5.7 and 5.8. Some absorption peaks seen in the spectrum of Fig. 5.7 were due to atmospheric absorption in a 1.5 m path length. The spectra in Fig. 5.8 show that the comb bandwidth was preserved as power was increased, therefore supporting the generation of ultrashort pulses. The MIR idler power was changed by tuning the current of the YDFA's pump in Fig. 5.2. The observed differences in the spectral envelopes on the right plot came from maximizing the power by readjusting the delay between signal and pump pulses after changing the YDFA current. Considering, for example, the bandwidth defined from 2900 to 3200 nm in Fig. 5.7, which concentrated 74 % of the power, the average power per mode was estimated to be 4 µW. For the higher power spectrum in Fig. 5.8, considering the full bandwidth defined from 2800 to 3500 nm, the average power per mode was estimated to be 2.5 µW.

Figs. 5.9 and 5.10 show spectra for the pump and signal beams, measured after the PPLN both in the presence and absence of nonlinear conversion, at the conditions of the maximum power curve in Fig. 5.8. DFG was switched off either by blocking one of the beams or by adjusting

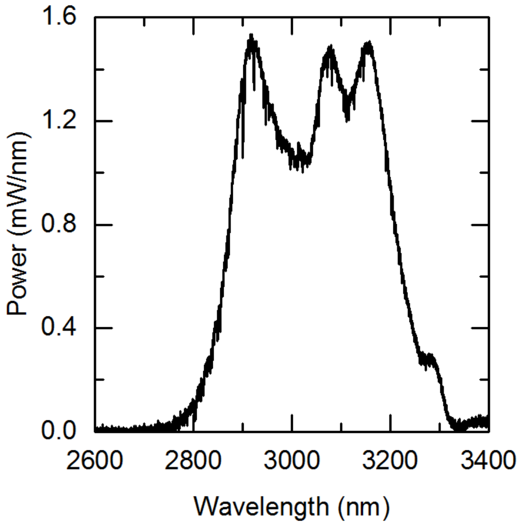

Figure 5.7: MIR spectrum generated by DFG in a single PPLN grating, recorded in a high-resolution grating-based optical spectrum analyzer (RBW = 0.2 nm). Absorption lines due to atmospheric propagation in a 1.5 m path length can be seen.

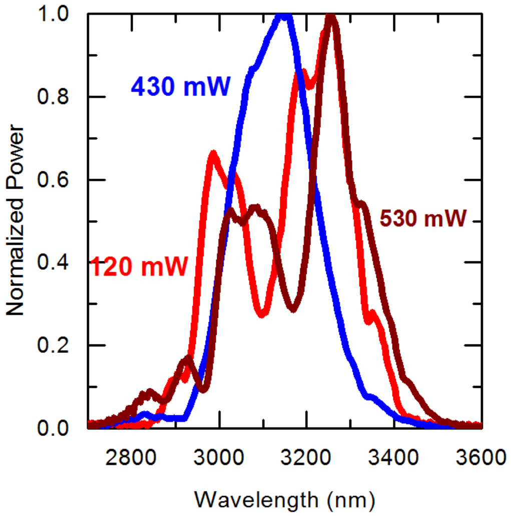

Figure 5.8: MIR comb spectra recorded in a low-resolution FTIR spectrometer (RBW = 4 nm) for different powers, showing that the combs bandwidth was preserved at high powers. Different spectra can be obtained as the temporal overlap between the pump and signal pulses is adjusted.

the delay stage in order to avoid temporal overlap at the crystal. The MIR spectral bandwidth was expected to reflect the combined spectra of the pump and signal. The pump input spectrum

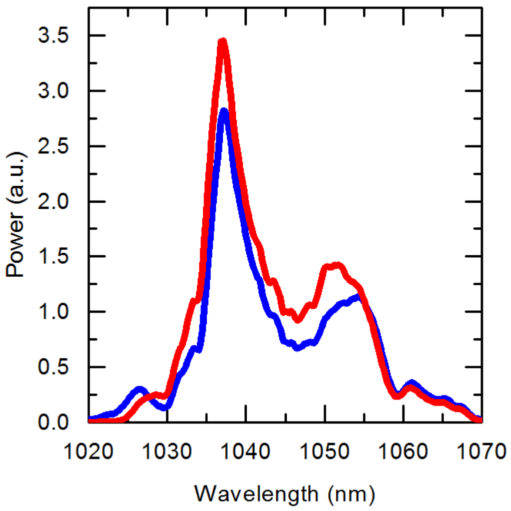

Figure 5.9: Pump spectra measured after the PPLN crystal when both beams were present (DFG on, blue trace) and when one of them was blocked (DFG off, red trace). The red side of the pump spectrum underwent less depletion. The DFG was correspondingly less efficient on the red side of the idler spectrum.

extended approximately from 1025 nm to 1070 nm and the signal spectrum extended from 1510 nm to 1625 nm, and thus the idler was expected to extend from 2770 nm to 3670 nm, which are the phase-matched wavelengths for one of the PPLN gratings (29.98 µm period). However, while the MIR spectra for all the PPLN gratings started at the expected lower limit (as seen in Figs. 5.7 and 5.8), they extended only up to 3500 nm, indicating that DFG was less efficient on the red side. The varying efficiency observed was not able to be explained.

The spectra in Figs. 5.9 and 5.10 also show that DFG in the 3-mm-long PPLN crystal occurred with considerable pump depletion and high parametric gain for the signal beam. For example, a pump beam with 3.6 W had its power depleted to 2 W after the crystal (2.5 dB attenuation), while the signal beam was amplified from 130 mW to 1.12 W, corresponding to a power gain of 8.6 (9.4 dB or 7.2 cm^{-1}). These beams generated 530 mW of MIR power. Figs. 5.11 and 5.12 show autocorrelation traces for the pump and signal beams (measured before the crystal). From those, the FWHM pulse durations associated with the narrow features are estimated as 210 fs and 60 fs, respectively.

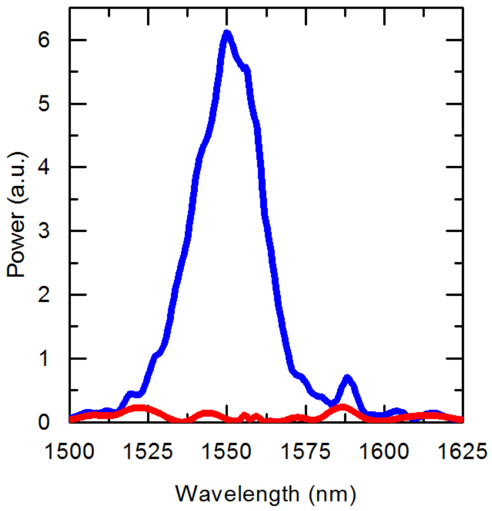

Figure 5.10: Signal spectra measured after the PPLN crystal when both beams were present (DFG on, blue trace) and when one of them was blocked (DFG off, red trace). The blue side of the signal spectrum underwent less amplification.

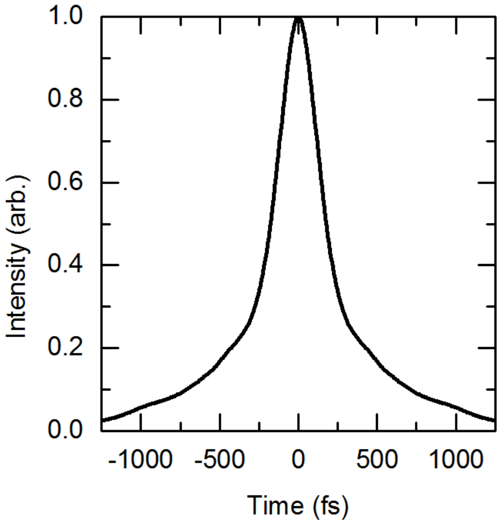

Figure 5.11: Autocorrelation trace for the pump beam, measured before the PPLN crystal. The pedestal was a result of higher-order dispersion unable to be corrected using the pair of transmission gratings.

A simplified analysis of the DFG, which does not initially take into account the broad spectral bandwidth of the pulses or the Gaussian profile of the input beams, was performed by numerically

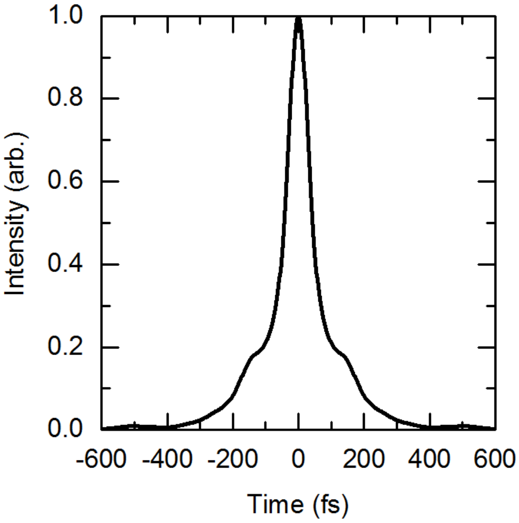

Figure 5.12: Autocorrelation trace for the signal beam, measured before the PPLN crystal.

integrating the coupled equations for the pump, signal, and idler field amplitudes (A_p, A_s, A_i) from Sec. 2.3 in the time domain. The coupled equations, in which the peak field amplitude of the pulses is considered, are given as

$$\frac{\mathrm{d}A_p}{\mathrm{d}z} = \frac{8\pi i d_{\text{eff}}\omega_p^2}{k_p c^2} A_s A_i e^{-i\Delta k z}, \tag{5.1}$$

$$\frac{\mathrm{d}A_s}{\mathrm{d}z} = \frac{8\pi i d_{\text{eff}}\omega_s^2}{k_s c^2} A_p A_i^* e^{i\Delta k z}, \text{ and} \tag{5.2}$$

$$\frac{\mathrm{d}A_i}{\mathrm{d}z} = \frac{8\pi i d_{\text{eff}}\omega_i^2}{k_i c^2} A_i A_s^* e^{i\Delta k z}, \tag{5.3}$$

where d_{eff} is the effective nonlinear crystal coefficient, $k_j = 2\pi/\lambda_j$, and Δk is the phase mismatch. The calculated average powers, which can be compared to the measured ones, are related to the peak field amplitudes by $P_{\text{avg}} = \sqrt{\pi}/(2\pi)|A|^2(\pi\omega_0)^2 t_{\text{pulse}} f_{\text{rep}}$, where ω_0 is the laser waist size at the crystal, t_{pulse} is the pulse duration, and f_{rep} is the repetition rate. Fig. 5.13 shows the calculated average powers for pump, signal, and idler, obtained by assuming the experimental parameters of the plots in Figs. 5.9 and 5.10: pump and signal central wavelengths λ_p = 1048 nm, λ_s = 1568 nm; pump and signal average input powers $P_{\text{avg}}^{\text{pump}}$ = 3.6 W, $P_{\text{avg}}^{\text{signal}}$ = 130 mW; repetition rate

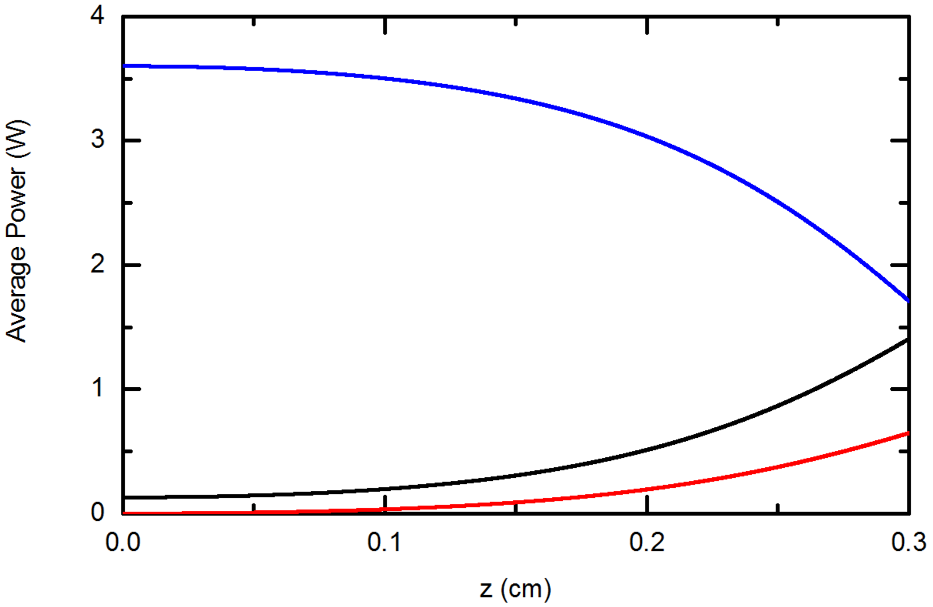

Figure 5.13: Simulated average powers for pump (blue), signal (black) and idler (red) beams as a function of propagating distance inside the 3-mm-long PPLN crystal.

$f_{\text{rep}} = 100$ MHz; pulse durations $t_p = 210$ fs, $t_s = 100$ fs (considering the structure of the signal pulses, Fig. 5.12); waist sizes $\omega_{0p} = 50$ µm, $\omega_{0s} = 70$ µm; polarizations $e + e \rightarrow e$; PPLN nonlinear coefficient $d_{\text{eff}} = 14.9$ pm/V; and perfect phase-matching ($\Delta k = 0$). The pump depletion is 2.4 dB and the signal amplification is 9.3 dB. As discussed below, other factors not taken into account, such as the spectral structure of the pulses or group velocity mismatch (GVM) between them, can explain the difference between the values from this simplified simulation and the experimental ones. Despite these additional factors, the simulated idler power at 3 mm (646 mW) does not substantially overestimate the measured idler power (533 mW after correcting for filter losses).

From Fig. 5.13, one can also ask if a longer crystal could be used to increase the idler power further. The DFG efficiency will be limited by GVM, which causes temporal walk-off between the pulses, and group velocity dispersion (GVD), which can broaden the pulses, reducing their intensities and the DFG efficiency. Both effects are characterized by effective lengths, which are useful to estimate the maximum crystal length over which GVM and GVD could be neglected.

The GVM length is given by $L_{\mathrm{GVM}} = t_p/\mathrm{GVM}$, where t_p is the pulse duration and $\mathrm{GVM} = (1/v_{gp} - 1/v_{gs})$, where v_{gp} and v_{gs} are the group velocities for pump and signal pulses. Using $t_p = 210$ fs, measured for the pump pulse, and the group velocities for the signal and pump beams for PPLN, $L_{\mathrm{GVM}} = 1.92$ mm. Therefore, in the 3-mm crystal, the pump-signal temporal walk-off was 2×210 fs, indicating that GVD is the limiting factor in more efficient MIR generation with the present crystal. The pump and idler pulses, which in turn amplify the signal, had more similar group velocities and could propagate together in the PPLN crystal over a GVM length of 5 mm, assuming 210 fs pulses. The dispersion length associated with GVD is given by $L_D = t_p^2/\mathrm{GVD}$, where $\mathrm{GVD} = \mathrm{d}^2k/\mathrm{d}\omega^2 = 254\ \mathrm{fs}^2/\mathrm{mm}$ for the pump pulses. Then, $L_D = 17$ cm at 1050 nm, indicating that a much longer crystal would still preserve the duration of the pump pulse, and therefore also its intensity and parametric gain. The dispersion lengths for the signal and idler pulses (assumed to be 60 fs and 70 fs respectively) were 3.6 cm and 8 mm respectively, indicating that neither one was significantly broadened by propagation in the 3-mm crystal.

The poor conversion efficiency on the red side of the MIR spectrum that was discussed in the context of Figs. 5.7, 5.8, 5.9, and 5.10 may also be related to temporal walk-off due to GVM between the pulses. For example, if the pump and signal pulses had some amount of residual chirp and separate as they propagate into the crystal, a better temporal overlap could happen between higher frequencies of the pump pulse and the lower frequencies of the signal pulse, which generate higher frequencies in the idler pulse. On the other hand, lower frequencies of the pump pulse could quickly separate from the higher frequencies of the signal pulse, preventing the generation of lower frequencies in the idler spectrum. In such a case, spectral shaping of the input pump and signal pulses could be used to shape the MIR spectrum.

5.3 Application to MIR Molecular Spectroscopy

The broad-bandwidth MIR spectra can be applied to the spectroscopy of molecular gases using a variety of detection techniques. As a first illustration, Figs. 5.14 and 5.15 show absorption spectra of the ν_3 band of methane (CH_4) and acetylene ($^{12}C_2H_2$ and $^{13}C_2H_2$) in sealed gas cells,

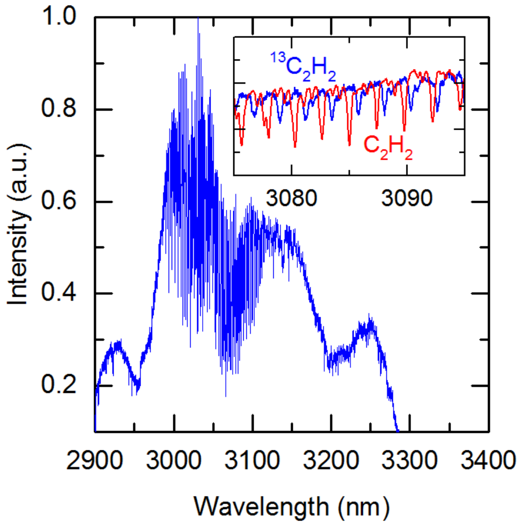

Figure 5.14: Absorption spectra (without subtraction of the comb spectra) of two gas cells of $^{12}C_2H_2$ and $^{13}C_2H_2$ (75 mm long, 50 Torr). Inset: zoomed region shows isotope shifts of individual lines when each gas component is measured separately.

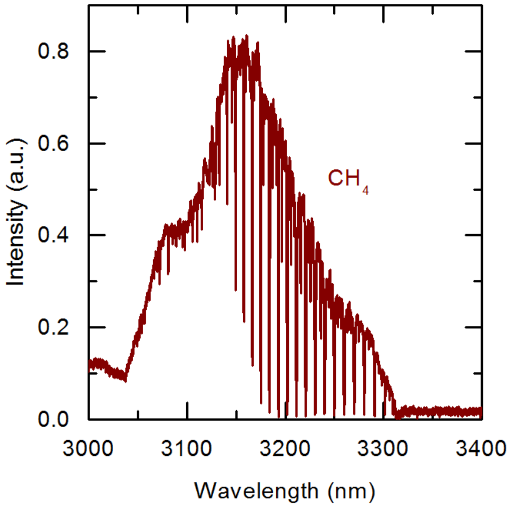

Figure 5.15: Spectrum of a CH_4 cell (75 mm long, 200 Torr).

which were obtained directly from one of the MIR combs with a grating-based optical spectrum analyzer (OSA). These single-trace spectra, recorded with 0.2 nm resolution (0.2 cm^{-1} or 6.0 GHz, comprising 60 comb modes), show good SNR and sensitivity, indicating low comb intensity noise.

Ultimately, higher resolution spectra with the full amplitude and phase information of the absorbing media can be obtained via a multi-frequency heterodyne (dual-comb) between two MIR combs. This requires high mutual coherence between the combs, which can be obtained by locking their repetition rate difference to a stable RF reference or by locking each comb to a common optical frequency reference. Even without fully implementing those techniques, good coherence was demonstrated between the MIR combs by recording the time-domain interferogram obtained by heterodyning them. Fig. 5.16 shows an interferogram obtained with the setup of Fig. 5.2 using a C_2H_2 cell (75 mm long, 50 Torr) in the path of one of the MIR combs. The interferogram is an average of five traces, and shows a central burst followed by the free-induction decay of the C_2H_2 molecules [145]. In this experiment, the repetition rate difference Δf_{rep} between the combs was loosely stabilized to 96 Hz using a low-bandwidth servo system to lock the repetition rate of one Er:fiber laser to a microwave signal synthesized from the second Er:fiber laser ("local oscillator"). For these data, the local oscillator was free-running. Its stabilization can be implemented in future experiments, but here the offset frequency of the MIR comb was eliminated in the DFG process, such that absolute frequency information can be obtained with only f_{rep} stabilized. The interferograms repeat at $(96\ \mathrm{Hz})^{-1} = 10.4$ ms, and a shorter 42 µs section is shown in Fig. 5.16. The x-axis is the "laboratory time" (real time) as given by a fast acquisition oscilloscope, which recorded the output of the MIR photodetector after passing through a 50 MHz low-pass filter. The optical power incident on the C_2H_2 cell was 50 mW, but an optical attenuator was placed before the MIR photodetector in order to avoid saturation by light from both combs.

Fig. 5.17 shows an FFT of the interferogram, showing absorption lines of the ν_3 band of C_2H_2. The spectral resolution is estimated to be 0.8 cm^{-1} (25 GHz or $\Delta\nu/\nu = 2.5 \times 10^{-4}$), limited by the 42 µs "lab time" duration of the interferogram, which corresponds to an "effective time" (rescaled from radio frequency domain) of 42 µs $\times \Delta f_{\mathrm{rep}}/f_{\mathrm{rep}} = 40$ ps.

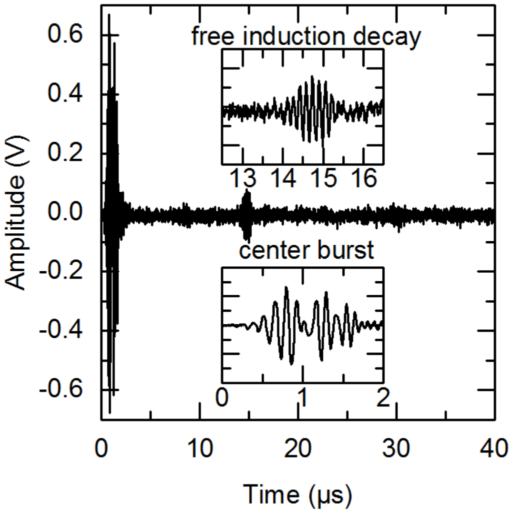

Figure 5.16: Average of five interferograms from heterodyning two combs, with a C_2H_2 gas cell (75 mm long, 50 Torr) in the path of one of them. The central burst corresponds to the comb pulses crossing at the detector, and is followed by revivals due to molecular free-induction decay. The x-axis is the laboratory time.

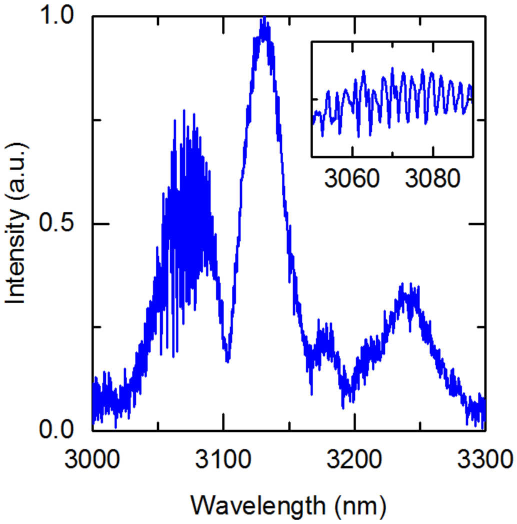

Figure 5.17: Fast Fourier transform of the interferogram, revealing absorption lines of the ν_3 band of $^{12}C_2H_2$.

5.4 Conclusion

In conclusion, 100 MHz MIR optical frequency combs based on PM fiber amplifiers and difference frequency generation (DFG) were developed. MIR spectra extended from 2.8 µm to 3.5 µm with average powers above 500 mW, corresponding to about 3 µW/mode. The use of PM fibers provided reduced amplitude noise compared to our previous comb based on non-PM fibers. MIR absorption spectra show good SNR and sensitivity. Simulations of the DFG power show good qualitative agreement with our experimental data. Mutual coherence between two similar, weakly-locked combs with slightly different repetition rates was demonstrated by examining the time-domain interferogram obtained from heterodyning them. An FFT of this interferogram reveals absorption lines of the ν_3 band of acetylene. The high powers and long-term stability demonstrated by this system indicate strong potential in implementing this style configuration to reach new wavelengths (Chapter 6) and as a pump source to drive nonlinear broadening in waveguides (Chapter 7).

Chapter 6

Extending Difference Frequency Generation to 5 Microns

6.1 Introduction and Overview

This chapter discusses the use of difference frequency generation, as in Chapter 5 at 3 µm, but instead in a pair of systems in order to generate light spanning 2.6–5.2 µm. Rather than implementing a high-power 1.5 µm signal for DFG as in Chapter 5, this chapter used a broadened spectrum spanning 1.3–1.6 µm in order to access over an octave of the mid-infrared spectrum. Additionally, this chapter aims to characterize the coherence and noise properties of these mid-infrared sources and optimize the sources to enable their future implementation in precision dual-comb mid-infrared spectroscopy.

The method of spectral generation described here centers around a robust 1.5 µm erbium fiber oscillator. Through nonlinear broadening in silica fiber [101], a 1.5 µm mode-locked laser generated spectra ranging from 1 µm to 2 µm (see Fig. 6.1, at left). The difference frequency generation between portions of the spectrum around 1 µm and some of the original 1.5 µm light then occurred in a single pass through millimeter-lengths of periodically-poled lithium niobate (PPLN) [146]. By tuning the period of the PPLN crystal, spectra were generated spanning from 2.6 µm to 5.2 µm, limited by the PPLN transparency at long wavelengths [56]. Across this range, single tuning bandwidths of 1–7 THz were achieved, as determined by a combination of phase-matching and input spectral bandwidth. Additionally, for the specific choice of parameters chosen, average powers ranging from 100 µW to 20 mW were generated. The residual intensity noise was characterized to be sufficiently low such that high signal-to-noise ratio (SNR) interferograms were

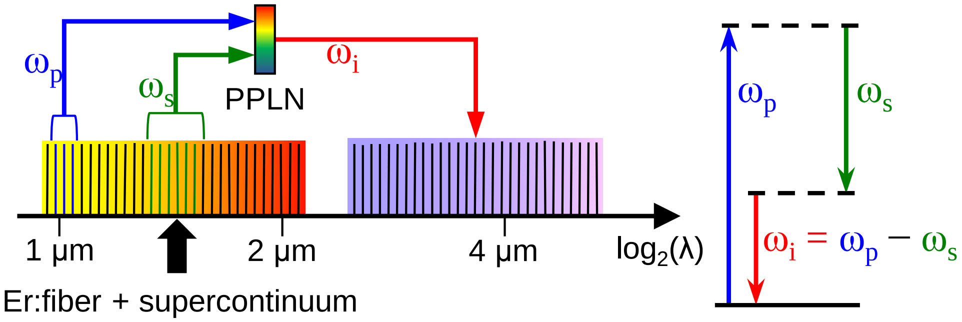

Figure 6.1: Left: Overview of mid-infrared difference frequency generation using a 1.5 μm erbium fiber laser. A supercontinuum was generated and was centered about the 1.5 μm source, portions of which were used in difference frequency generation in periodically-poled lithium niobate (PPLN). The details of this procedure are described in Sec. 6.3.1. Right: Energy level diagram of the difference frequency generation process. Pump photons (ω_p) at 1 μm drive the down-conversion process, which is seeded by 1.5 μm signal photons (ω_s), leading to parametric gain in the signal and also generating idler photons (ω_i).

achieved in the heterodyne between two such combs, thus demonstrating their utility for dual comb spectroscopy.

6.2 Theory

Difference frequency generation (DFG) has been well-described in the literature [119, 147–149]. Here a brief overview of the theory is presented behind the modeling shown in Sec. 6.4.4. The goal in doing so is to present a simple model that allows insight into and to compare with the main features observed in the experimental data. In particular, the physical and experimental parameters of the DFG process that constrain the achievable power and bandwidth are focused upon.

The process of DFG is a three-wave mixing nonlinear process between pump (p), signal (s) and idler (i) waves, also conveniently understood in the photon energy picture of Fig. 6.1 (at right). In the time domain, DFG can be described by three coupled differential equations [148]:

$$\frac{\partial A_s}{\partial z} = -\sum_{m=1}^{\infty} \frac{(-i)^{m-1}}{m!} k^{(m)} \frac{\partial^m A_s}{\partial t^m} - i\frac{\chi^{(2)}\omega_s}{2n_s c} A_p A_i^* e^{-i\Delta k \cdot z}, \tag{6.1}$$

$$\frac{\partial A_i}{\partial z} = -\sum_{m=1}^{\infty} \frac{(-i)^{m-1}}{m!} k^{(m)} \frac{\partial^m A_i}{\partial t^m} - i\frac{\chi^{(2)}\omega_i}{2n_i c} A_p A_s^* e^{-i\Delta k \cdot z}, \tag{6.2}$$

and

$$\frac{\partial A_p}{\partial z} = -\sum_{m=1}^{\infty} \frac{(-i)^{m-1}}{m!} k^{(m)} \frac{\partial^m A_p}{\partial t^m} - i\frac{\chi^{(2)}\omega_p}{2n_p c} A_s A_i e^{i\Delta k \cdot z}, \tag{6.3}$$

where $A = A(t)$ and $A^*(t)$ are the electric field amplitudes of each wave (signal, idler, pump) in the time-domain and their complex conjugates, $k^{(m)}$ is the m^{th} order dispersion coefficient, $\chi^{(2)}$ is the second-order nonlinearity of the nonlinear medium (in this case, PPLN), ω is the angular frequency of each wave, n is the refractive index of each wave, and $\Delta k = k_p - k_s - k_i - \frac{2\pi}{\Lambda}$ is the magnitude of the wave-vector mismatch, where Λ is the poling period of the PPLN crystal. For these simulations, only $m = 1$ and 2 were used; that is, only first- and second-order dispersion were incorporated. The amplitudes of the input fields A_p and A_s were created using measured values of average power, pulse duration, and beam waists. These simulations assumed plane waves with no diffraction, which is valid when the crystal length is within the confocal parameter of the focused beam (accurate for both the 1 mm and 3 mm crystal lengths used here), and the electric field amplitudes $A(t)$ assumed Gaussian envelopes. The simulations also incorporated PPLN material absorption [56], not shown in the above equations. These coupled equations were then numerically integrated through the PPLN crystal along the z-axis. The results of these simulations were used to confirm observed bandwidth and power measurements, discussed later in Sec. 6.4.4.

The dynamics of the pulse propagation in the PPLN crystal are dictated by the optical nonlinear interaction among the pulses and their dispersion through the crystal. For a pump beam centered at 1074 nm, the group velocity of the signal pulse at 1.3 µm is 1 % higher than the pump, while the idler group velocity at 5 µm is 4.4 % smaller. For the input pulse durations used in the simulations (400 fs for pump and 60 fs for signal), the group velocity mismatch (GVM) length for pump and signal is 4.65 mm, meaning that they propagate overlapped within each crystal, with the

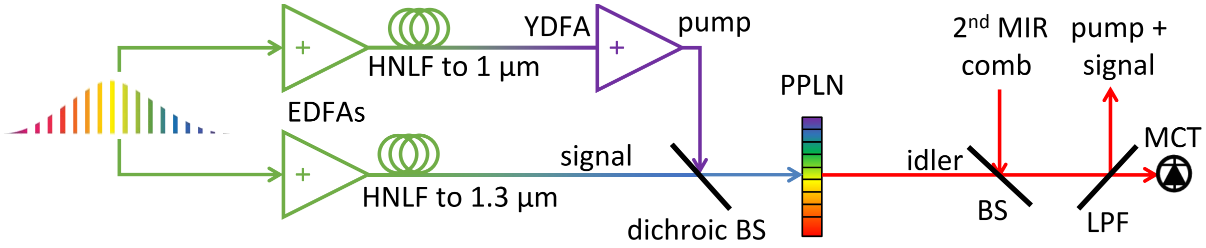

Figure 6.2: Schematic of one of the two difference frequency generation (DFG) apparatuses. An erbium fiber oscillator was split into two branches. The pump branch (top) was amplified to roughly 200 mW in an erbium-doped fiber amplifier (EDFA) before launching into highly nonlinear fiber (HNLF) to broaden the spectrum to 1 µm. This served as the seed for a ytterbium-doped fiber amplifier (YDFA), which provided 1 W of power after compression using a pair of transmission gratings. The signal branch (bottom) was also amplified to roughly 200 mW in an EDFA and launched into a HNLF of different dispersion to broaden the spectrum to 1.3 µm. The output of these two branches were combined using a dichroic beam-splitter (BS), focused into to a periodically-poled lithium niobate (PPLN) crystal. This generated idler spectra spanning 2.6–5.2 µm, the center wavelength of which was adjusted by choosing different poling periods. The generated mid-infrared light was combined with a second DFG system for dual-comb interferometry (discussed in Sec. 6.4.5), and a long-pass filter (LPF) filtered out the pump and signal beams for diagnostic purposes and to isolate the idlers, which were detected on a mercury cadmium telluride (MCT) detector.

signal leading the pump pulse. As the pump and signal propagate, the continuously generated idler propagates with smaller group velocities for longer wavelengths. For 5 µm pulses and sufficiently longer crystals, the idler leaves a long tail behind the pump and signal, which can make this pulse much longer and spectrally narrower.

6.3 Experimental Design and Results

6.3.1 Experimental Setup

The near-infrared frequency combs used to generate the two mid-infrared combs were modified from those described Chapter 5 and [51] to allow for tunability from 2.6 µm to 5.2 µm. Each frequency comb was based on an erbium fiber ring oscillator, which generated a 1.5 µm frequency comb at 100 MHz (see Fig. 6.2). The generated comb light was split into two branches, which produced the pump and signal used in DFG. Most of the fiber-based portions of the systems were made from polarization-maintaining components, which contributed to the long-term stability.

In the pump branch, a normal-dispersion erbium-doped fiber amplifier (EDFA) (top, in Fig. 6.2) was used to generate short pulses with high peak power (roughly 200 mW and 70 fs) at 1.5 µm. The fiber lengths in the Menlo oscillator system were 12 cm of PANDA (after 20 cm of internal fiber from the Menlo comb had been removed), 82 cm of PM EDF, and 39 cm of PANDA, and the fiber lengths in the home-built system were 82 cm of PANDA, 94 cm of PM EDF, and 63 cm of PANDA. The generated pulse was launched into a short length (8 cm in the Menlo-based system, 15 cm in home-built oscillator system) of PM highly nonlinear fiber (HNLF) with a zero dispersion wavelength (ZDW) of roughly 1350 nm to create a low-noise dispersive wave at 1 µm [102, 150]. This was the seed for a high-power ytterbium-doped fiber amplifier (YDFA), which produced 2 W at 1 µm and was the pump source in DFG. Both systems stretched the pulses using either fiber Bragg gratings or negative third-order dispersion fibers to roughly 50 ps before launching into either highly-doped double-clad ytterbium gain fiber or a commercial high-power ytterbium amplifier. The pump pulse was compressed using a pair of transmission diffraction gratings (1600 grooves/mm, not shown in figure). The pump power that reached the crystal after compression and beam-shaping optics was 735 mW. Part numbers are provided in the appendix, in Secs. B.3 and B.4.

The signal branch (bottom, in Fig. 6.2) also featured an EDFA with similar characteristics to that described previously. The fiber lengths in the Menlo-based system were 60 cm of PANDA, 68 cm of PM EDF, and 48 cm of PANDA, and the fiber lengths in the home-built oscillator system were 132 cm of PANDA, 102 cm of PM EDF, and 60 cm of PANDA. The output of this amplifier was launched into a short section of PM HNLF (7 cm of HNLF in the Menlo-based system, 3.5 cm in the home-built oscillator system) with a ZDW of roughly 1520 nm; the pulses' chirp and peak power were catered towards generating spectral power between 1.3 and 1.5 µm (see Fig. 6.4 and description in Sec. 6.3.2). This was the signal source in DFG. The total signal power across the entire spectrum was 81 mW, 6 mW of which was in the 1.3 µm phase-matching bandwidth for 5 µm production.

Focusing both beams to the same position with similar waists and confocal parameters is important for strong mode overlap, and thus idler generation. The HNLF used in the signal

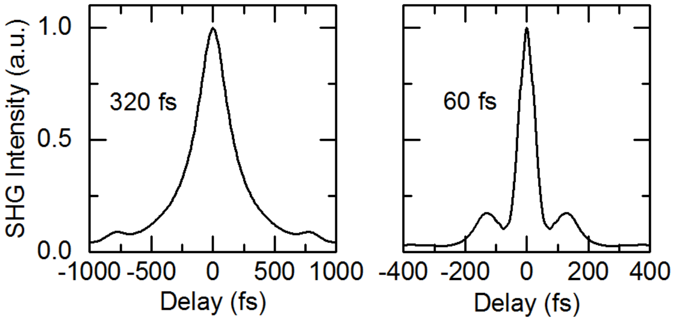

Figure 6.3: Second harmonic generation autocorrelation of the 1 µm pump beam (left) and 1.3 µm signal beam (right). Delay vs. second harmonic intensity is plotted, and the autocorrelation width of each is shown adjacent to the plot.

branch has a small core, and a collimator with a high numerical aperture was used to collect and collimate the most light. This beam was minimally shaped thereafter to avoid possible chromatic aberrations due to its broad bandwidth. The pump, therefore, was tailored to match the signal. The pump beam implemented a telescope of two achromatic lenses, the spacing of which had fine adjustment. The pump and signal beams were focused into a PPLN crystal using a 40 mm focal length achromatic lens, and the telescope in the pump branch was adjusted so the two beams focused to the same plane. The beam waists of the pump and signal beams were 15 µm and 19 µm, respectively, measured using integrated power measurements with a translation stage and a razor blade. These were chosen so the two beams' confocal parameters would match while also containing both beams' Rayleigh lengths within a 3-mm crystal. The beam waists corresponded to average intensities of 200 kW/cm^2 for the pump and 15 kW/cm^2 for the signal. The PPLN crystal was either 1 or 3 mm in length, with poling periods that allowed for the quasi phase matching of 1 and 1.3–1.5 µm pump-signal pairs. The resulting output spectra, powers, and other characteristics are described in detail in later sections.

6.3.2 Pump and Signal Characterization

Maximal pulse compression is essential for optimal DFG in order to obtain the most peak power that drives the nonlinear process. The pump pulse duration was optimized using a free-space

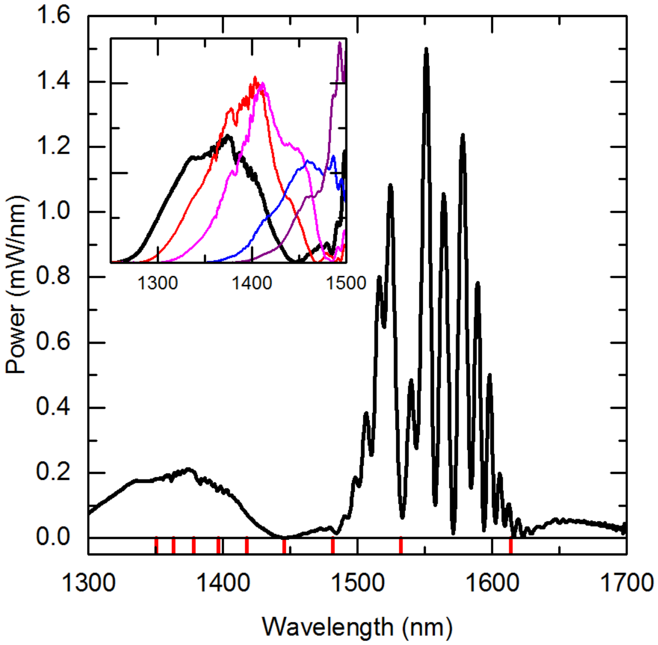

Figure 6.4: Main figure: the broadened output of the EDFA used as the signal in the DFG process is shown (black, thick). This spectrum was measured using a grating-based optical spectrum analyzer (OSA). The phase-matching wavelengths for different poling periods present in the PPLN crystal for a fixed 1074 nm pump are also indicated (red, short sticks). Inset: the signal spectrum can be tailored for maximum signal power at a given poling period phase-matching wavelength by varying the pump current (original spectrum in black, thick; other spectra are thin and in color).

grating compressor, as in Chapter 5, and the signal pulse duration was optimized via compression in polarization-maintaining, anomalous-dispersion, single-mode fiber, as in Chapter 4, before launching into HNLF. Second harmonic generation autocorrelations of both the pump and the 1.3–1.4 µm portion of the signal are shown in Fig. 6.3 at left and right, respectively. The autocorrelation widths of the pump and signal were 320 fs and 60 fs, respectively. If hyperbolic secant (sech^2) pulses are assumed, these correspond to minimum pulse durations of 210 fs and 40 fs. While clear evidence of incomplete compression is seen in the wings of these autocorrelations, the achievable pulse durations were not limiting factors in the subsequent DFG generation.

The spectrum of the signal used in 5 µm generation is shown in Fig. 6.4 in black, and the corresponding poling periods' phase-matching wavelengths for a 1074 nm pump are shown as short red sticks along the wavelength x-axis. The poling periods corresponding to the longest idler wavelengths correspond to the shortest signal wavelengths. The poling periods are (from left to right in Fig. 6.4): $\Lambda = 24.63$ µm, 25.23 µm, 25.86 µm, 26.53 µm, 27.22 µm, 27.96 µm, 28.74 µm, 29.56 µm, 30.43 µm, and 31.35 µm (off-scale right). This spectrum was tailored specifically to generate optical power at the shortest phase-matchable signal wavelengths in order to generate long-wavelength idlers. However, the spectral peak between 1.3–1.4 µm can be moved to the red by reducing the pump power feeding the EDFA. These changes are shown in the inset in Fig. 6.4 as the thinner, colored lines, and these spectral choices allow for more efficient production of idler power between 3.5 and 4.5 µm.

6.4 Results and Analysis

6.4.1 Spectral Coverage

The attainable MIR spectral coverage using both 1 mm and 3 mm PPLN crystals was measured using a Fourier transform spectrometer, and is shown in Fig. 6.5. A fixed pump and signal were able to produce a tunable octave from 2.6–5.2 µm by simply changing the poling period of the PPLN crystal. Finer tuning can be achieved by changing the temperature of the PPLN crystal. The long-wavelength limit of the spectra shown is a result of the transparency window of PPLN; published values indicate that the absorption increases from roughly 10^{-2} cm^{-1} at 3 µm to 10^{-1} cm^{-1} at 4 µm and 1 cm^{-1} at 5 µm [56]. The peaks here are normalized to the measured integrated power (plotted in Fig. 6.7) and normalized to the maximum peak in each set. The spectral shapes are verified via simulation and will be explained in greater detail in Sec. 6.4.4.

6.4.2 Beam Characterization

One useful metric for determining the suitability of a laser beam for heterodyne detection, collimation, and both fiber and waveguide coupling is its mode quality. This was evaluated by collimating the 5 µm idler from one of the DFG systems, propagating it 2 m, then imaging it on an indium antimonide (InSb) camera array, shown in Fig. 6.6. Each axis of the beam profile was

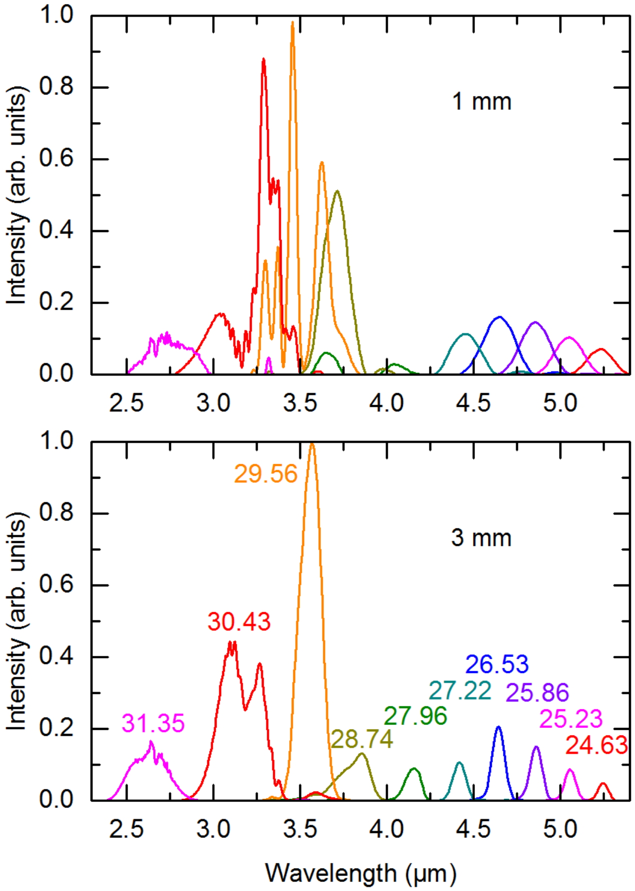

Figure 6.5: The attainable spectral coverage using both 1 mm (top) and 3 mm (bottom) PPLN crystals. Spectra are scaled according to their measured integrated power. Each colored curve corresponds to a different poling period, shown in color-coded text (in microns) on the bottom plot. The gap seen near 4.2 µm results from weak power at the corresponding signal wavelength, as seen in Fig. 6.4. The longer of the two crystals has a narrower phase-matching bandwidth, and thus the spectra shown at bottom are narrower.

integrated and fitted with a Gaussian, shown in the axes above and to the right of the camera image. Good modal quality is demonstrated and enables the heterodyne detection described in Sec. 6.4.5. The full-width at half-maximum (FWHM) of the beam in the x-direction is 1.4 mm, and 1.3 mm in the y-direction.

6.4.3 Power Measurements

DFG produced powers over a wide band of wavelengths ranging from roughly 100 µW (1 mm crystal, 5.2 µm) to over 20 mW (3 mm crystal, 3.5 µm). Powers using a 40 mm achromatic lens

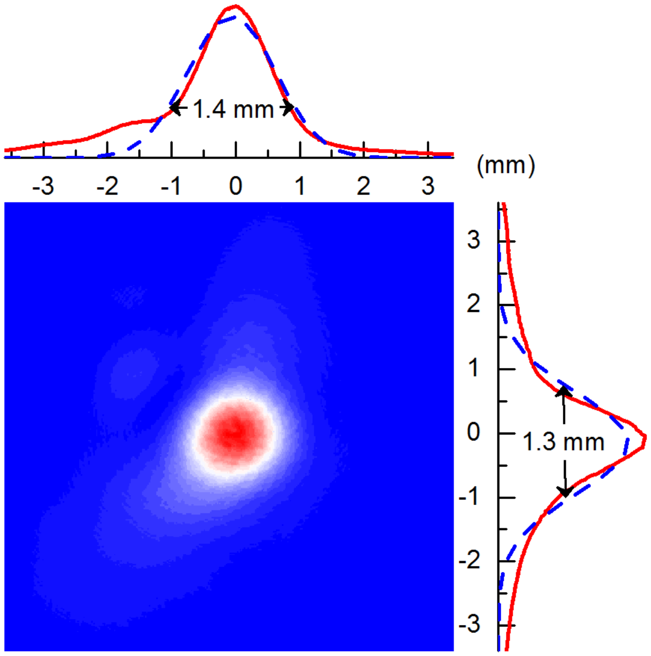

Figure 6.6: Indium antimonide (InSb) camera image of collimated 5 µm beam, with line plots above and to the right showing the integrated x- and y-axes (solid red) and Gaussian fits to each (dashed blue).

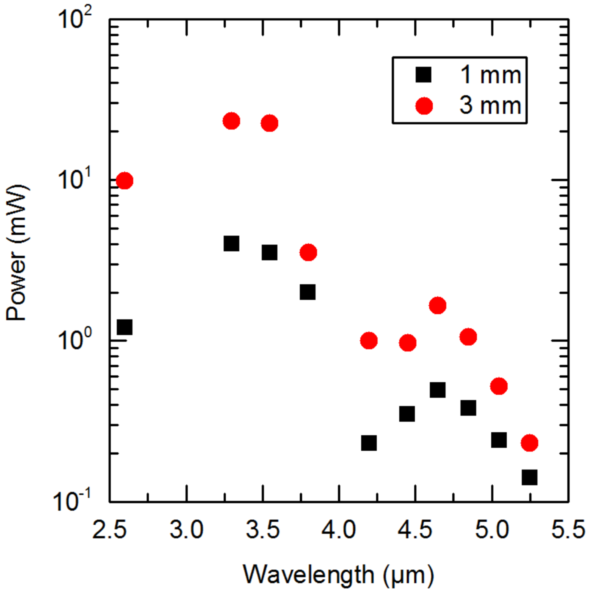

Figure 6.7: Optical power as a function of wavelength for 1 mm (black square) and 3 mm (red circle) PPLN crystals, plotted on a logarithmic scale. As PPLN absorption increases at longer wavelengths [56], the generated idler power decreases.

to focus beams into the crystal are plotted in Fig. 6.7. The focus positions, alignment, and delay between the two input pulses were optimized for the 5.05 µm points; all other data points were taken after changing only the poling period and optimizing the delay. These were measured using a thermal power meter. At 5.05 µm, this 40 mm lens generated 280 µW in a 1 mm crystal and 520 µW in a 3 mm crystal. Powers were also measured at this wavelength using a 100 mm lens to focus; this yielded 175 µW in a 1 mm crystal, 860 µW in a 3 mm crystal, and 1.37 mW in a 10 mm crystal. In the 1 mm crystal, the reduction in power is attributed to a larger beam waist, and thus lower input intensities. In the 3 mm crystal, the increase in power is attributed to the longer confocal parameter, which keeps the intensity more uniform throughout the crystal than the 40 mm lens. In fact, the 100 mm lens produces a confocal parameter of 92 mm, which is comparable to the 10 mm crystal length. This assures that the simulated powers, which did not account for beam diffraction, should approximate the experimental values well. Further gains can be achieved by increasing the pump power at 1 µm, optimized beam focusing at the crystal, and more careful tailoring of the broadened signal spectrum. (In a similar system, 0.5 W was achieved at 3 µm [51].)

Extensive numerical simulations were performed in an effort to verify the observed 5 µm idler power. In these simulations, strong sensitivity was seen to exact parameters of pump and signal intensity and relative temporal overlap (delay), which are challenging to precisely realize in the experiments. However, the model systematically predicted higher powers than were observed at the longest idler wavelengths. The source of this discrepancy is not known, but would be explained by stronger mid-infrared material absorption than what is expected for PPLN [56]. The possibility of nonlinear or multiphoton loss [151] due to the generation of parasitic green light was not explored. Reduced power at longer idler wavelengths was also observed in earlier work [16]. Despite the lower than expected powers, the 5 µm light should be sufficient for lab spectroscopy, as detailed below.

6.4.4 Bandwidth Comparison to Simulations

The spectral profile of the generated idler from this experiment was modeled and verified through numerical simulation. Fig. 6.8 confirms the bandwidth of the idler in each crystal and

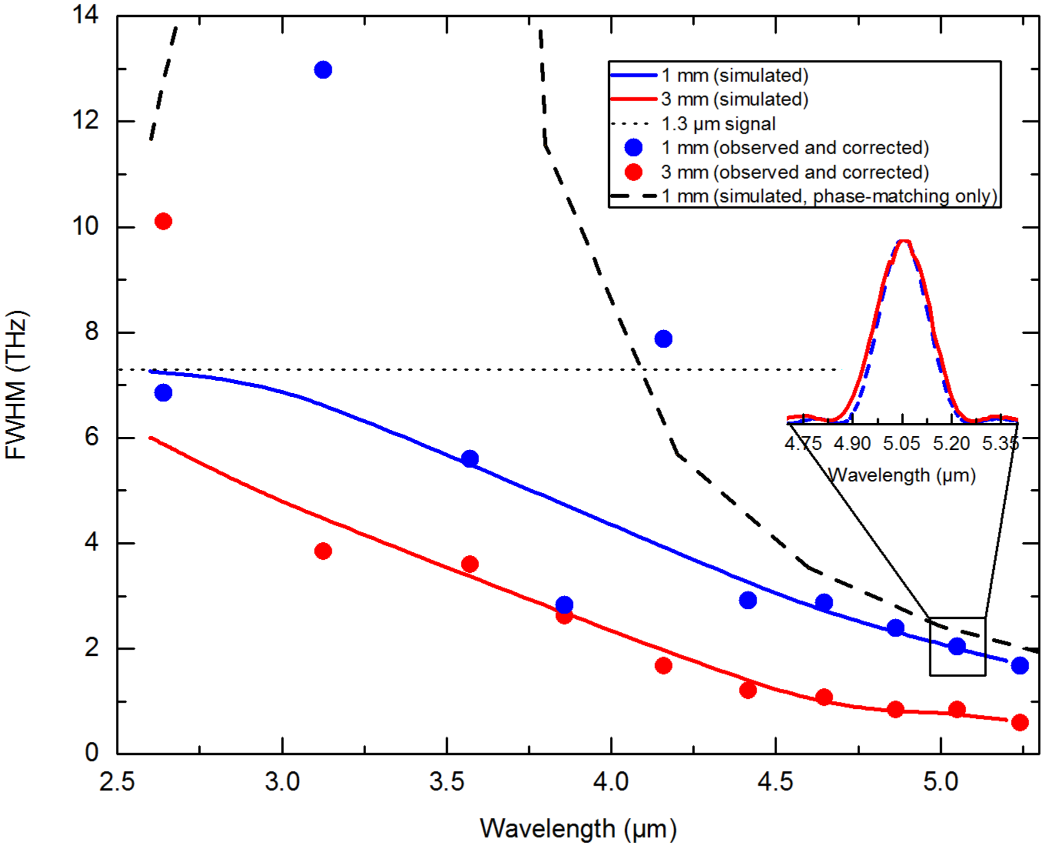

Figure 6.8: Simulated and observed bandwidth in 1 and 3 mm PPLN crystals. Dots signify the corrected observed full-width at half-maximum (FWHM) measurements for the two different crystal lengths. The correction divides the observed FWHMs by the convolution of the input pump and signal, which allows for the removal of the effect of the signal's spectral features. The solid lines show the simulated bandwidth of the idler, assuming a Gaussian pump and signal of durations as determined via the autocorrelations shown in Fig. 6.3. Dashed lines show the bandwidth of the input signal and the phase-matching bandwidth of a 1 mm crystal solely via ΔkL walk-off. Inset: simulated (dashed, blue) and experimental (solid, red) spectral widths for the 5.05 μm poling period.

poling period, from Fig. 6.5. The observed data points are shown as solid circles. These are not plotted as the full-width at half-maximum of the measured spectra directly, but divided by the convolution between the input pump and signal spectra to correct for some of the unusual spectral features found in the signal spectrum. (See the top panel of Fig. 6.5 between 3–4 μm for examples of idler spectral distortion.) Simulated bandwidths using Gaussian inputs are shown as solid lines, and, where the convolution correction is able to accurately recover a spectral shape, these agree quite well. At shorter wavelengths, the mid-infrared spectral width is limited by the spectral width of the signal (short dashes, horizontal line); at longer wavelengths, the mid-infrared spectral width is limited by the phase-matching bandwidth of PPLN (long dashes, plotted for a 1 mm crystal).

As can be seen from Fig. 6.8, the spectral bandwidth of the MIR comb, particularly at longer wavelengths, decreases as function of the crystal length. This is due to a corresponding decrease in the phase matching bandwidth, which the model predicts well. The same model allows the prediction of the MIR pulse durations. For example, the pulse durations for the two cases of $z = 1$ mm and $z = 3$ mm are approximately 250 fs and 450 fs, respectively. The pulses are slightly chirped due to the group velocity mismatch in PPLN, which makes the pump and signal pulses travel faster than the idler. The modeling shows that the idler pulse is continuously generated as it walks away from the pump and signal, leading to an asymmetric time duration.

6.4.5 Coherence and Noise Measurements

With the source power and spectrum now evaluated, the properties of this MIR DFG source can be studied for dual comb spectroscopy. This was assessed by performing multi-heterodyne measurements between the two combs. Interferograms of the combined MIR combs were recorded using a high-bandwidth (>100 MHz) liquid nitrogen-cooled mercury cadmium telluride (MCT) detector (see Fig. 6.2). A sample interferogram from the overlapping of the two 5 µm combs is shown in Fig. 6.9, along with the resulting transformed spectra. Here, the two combs' repetition rates were roughly 99.84 MHz, with a repetition rate difference of 290 Hz. The interferogram was a single shot, unaveraged, with both combs free-running and without any active stabilization. The inset shows the resulting spectrum from one unaveraged interferogram, and the noise reduction of 16 interferogram averages. The time-domain signal-to-noise ratio of the interferogram is estimated to be approximately 25, within the 50 MHz Nyquist filtered bandwidth of the digital sampling system. With a repetition rate difference of 290 Hz, interferograms occur every 3.4 ms. The averaging of 16 of these in succession, without stabilization or correction, demonstrates that the two mid-infrared

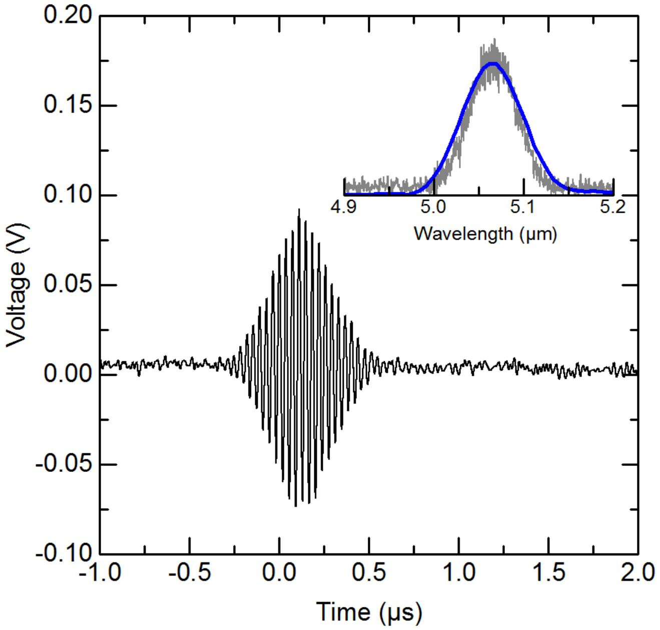

Figure 6.9: Main figure: interferogram of free-running (unstabilized) 5 μm multi-heterodyne. Inset: Fourier transform, re-scaled, of unaveraged interferogram (gray) and 16 averaged interferograms (blue).

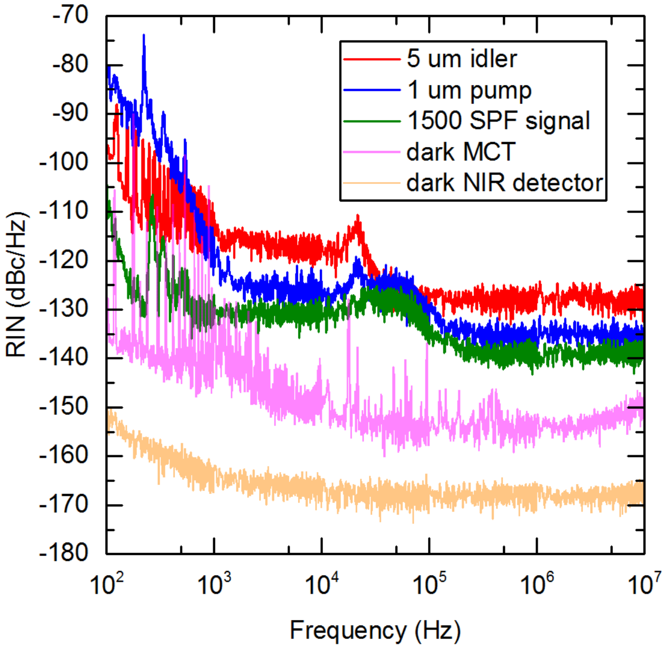

Figure 6.10: The relative intensity noise (RIN) of the 1 μm pump, broadened portion of the 1.5 μm signal after passing through a 1500 nm short pass filter (SPF), the generated 5 μm idler, and both the near-infrared and mid-infrared detector backgrounds.

combs exhibit coherence over at least 55 ms.

The RIN is shown in Fig. 6.10. Electronic noise is seen at low frequencies, but is native to the measurement setup and not the MIR source or the MCT detector, as indicated by the electronic background. One can see that the mid-infrared RIN is greater than that of the pump and the signal, having acquired RIN from the pump. This is most evident at 10^4 Hz, where a peak is visible in both plots.

The mid-infrared RIN plotted here is not significantly higher than that typical of near-infrared fiber sources; depending on amplification, detector noise, dynamic range, and spectral broadening, RIN from an erbium-based fiber laser can range from -145 to -125 dBc/Hz [152]. Additionally, previous work using HNLF to broaden EDFA light from 1.5 µm to 2 µm produces comparable RIN to what is shown here [74].

6.5 Conclusions

Using the design from Chapter 5, this chapter described the development of two widely tunable mid-infrared optical frequency combs with spectral coverage ranging from 2.6–5.2 µm. As in Chapter 5, the use of polarization-maintaining fiber and a single-pass nonlinear process provides a path towards a reliable, stable source with the ability to cover a broad spectral region of great interest in molecular spectroscopy. In particular, the strong coherence and low RIN of this system show potential for immediate implementation in robust, high-sensitivity mid-infrared dual comb molecular spectroscopy. The spectral shapes observed were explained and understood through numerical simulation. This particular system is limited by the transmission of PPLN, as seen in Ref. [56], but a similar scheme implementing a more transmissive nonlinear crystal at longer wavelengths such as gallium arsenide (GaAs) or gallium phosphide (GaP) would allow for much broader tunability and access to new spectral regions.

Chapter 7

Spectral Broadening in the Mid-Infrared Using Waveguides

7.1 Introduction

This chapter details the implementation of chip-scale waveguides pumped by the high-power 3 µm source from Chapter 5. This marks the early stages in the development of an integrated photonics platform to put different components of frequency combs on chip for robust, integrable, and small footprint mid-infrared sources [153]. The waveguides tested are made of silicon (fabricated by Nima Nader, of NIST) and silicon nitride (SiN) (fabricated by colleagues at École Polytechnique Fédérale de Lausanne, or EPFL). This chapter will discuss the design of the waveguides, the simulated dispersion of various designs, the generated spectra of the waveguides, and, lastly, for the silicon devices, heterodyne spectroscopy performed using the waveguide output and the output of one of the sources from Chapter 6. Experimental testing of waveguide designs was performed, and, while device modeling and fabrication was conducted by collaborators, these details are included in addition for completeness.

7.2 Motivation

Thus far in this thesis, the only material implemented in four-wave mixing for spectral broadening has been silica fiber, used in either polarization-maintaining single-mode fiber (PANDA) or highly nonlinear fiber (HNLF), a smaller-core fiber that yields higher intensities. However, the nonlinear coefficient of silica is low compared to that of other materials transmissive in the near- and mid-infrared regions; n_2 of silica is on the order of 10^{-16} cm^2/W. In comparison, that of silicon nitride is on the order of 10^{-15} cm^2/W, and that of silicon is on the order of 10^{-14} cm^2/W. Both silicon and silicon nitride are also transmissive beyond 2 µm, where silica fiber begins to absorb light, to roughly 7 µm [48]. Thus, both of these materials demonstrate strong potential in broadening mid-infrared spectra. Additionally, waveguides provide tight confinement, and thus high intensities, typically more so than a single-mode fiber. Lastly, waveguides allow for dispersion engineering through geometry.

7.3 Dispersion Engineering

7.3.1 Bulk Dispersion

In bulk material, the group velocity dispersion is simply a property related to the index of refraction of the material, namely:

$$D = -\frac{\lambda}{c}\frac{\mathrm{d}^2 n}{\mathrm{d}\lambda^2} \text{ and} \tag{7.1}$$

$$GVD = -\frac{D\lambda^2}{2\pi c} \tag{7.2}$$

where D is typically given in ps/(nm·km) and GVD is typically given in fs^2/mm. The dispersion of bulk silicon is plotted in Fig. 7.1 [57], and that of bulk silicon nitride is plotted in Fig. 7.2 [48]. The two plots are given in different units in order to match the later simulated waveguide dispersion plots provided by the waveguide designer.

7.3.2 Dispersion Control

However, for tightly confined beams, the beam is no longer fully confined to the core material (see Fig. 7.3). In this scenario, an effective mode index must be used in order to calculate the dispersion of the waveguide, incorporating the index of refraction of the cladding and the portion of the beam in the cladding. In addition to the how this affects the index's dependence on wavelength, the mode area also depends on the wavelength, and will typically be larger for longer wavelengths, incorporating more of the cladding in its effective index.

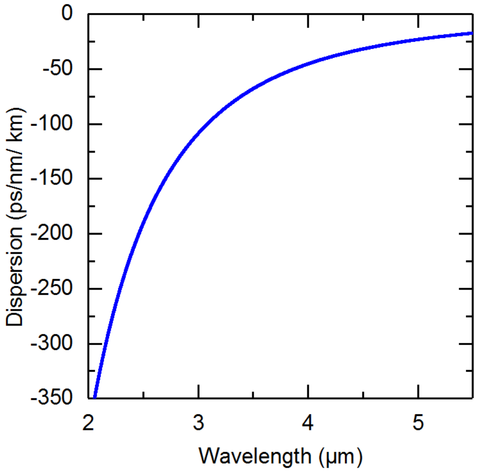

Figure 7.1: Plot of the dispersion of bulk silicon in the mid-infrared. The calculated dispersion is based on the Sellmeier equation, the coefficients of which are from Ref. [57].

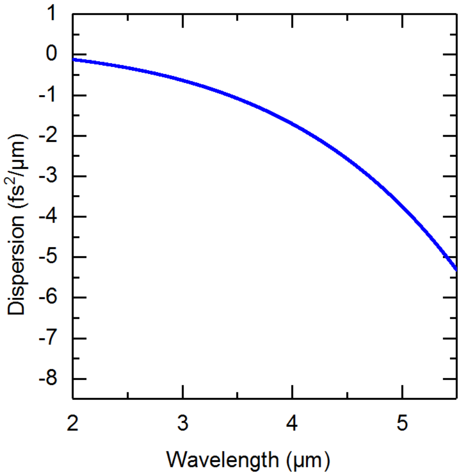

Figure 7.2: Plot of the dispersion of bulk silicon nitride in the mid-infrared. The calculated dispersion is based on the Sellmeier equation, the coefficients of which are from Ref. [48].

Thus, through wavelength dependence on effective index, the geometry of a waveguide can be used to control its dispersion. This will, in turn, determine the spectral generation of the waveguide, either through soliton generation (if the dispersion is anomalous and cancels the nonlinear phase) or through dispersive wave generation. The phase-matching condition for dispersive wave generation has been detailed more thoroughly elsewhere [154], but essentially the generated dispersive wave will form in the vicinity of the zero-dispersion wavelength (ZDW), across the ZDW from the pump.

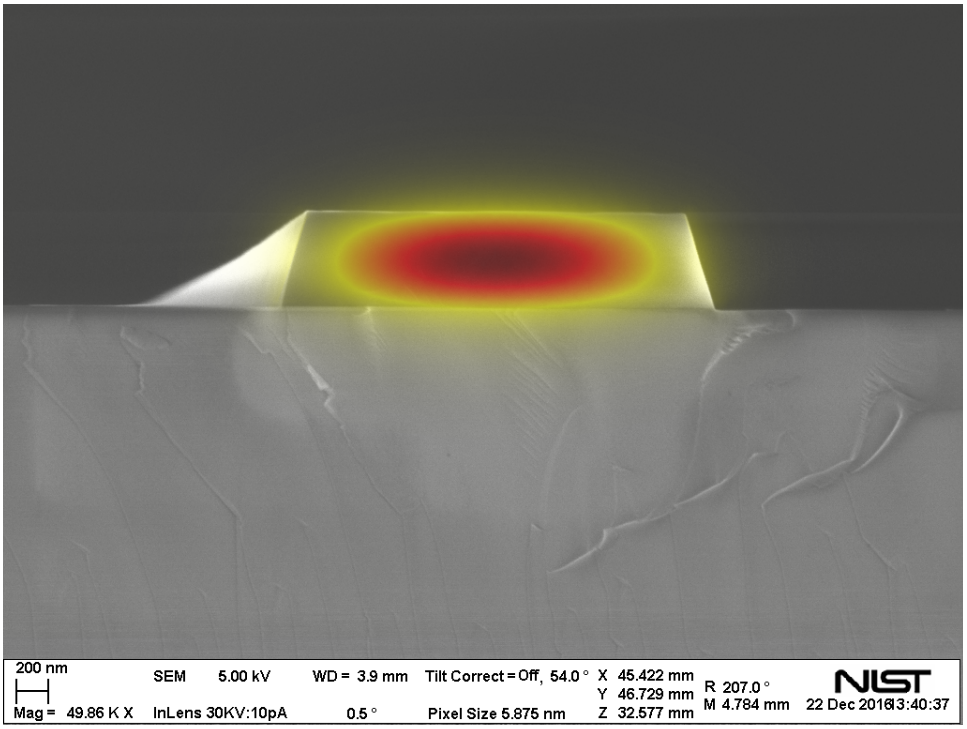
200 nm
Mag = 49.86 K X
SEM 5.00 kV
InLens 30KV:10pA
WD = 3.9 mm
0.5 °
Tilt Correct = Off, 54.0 °
Pixel Size 5.875 nm
X 45.422 mm
Y 46.729 mm
Z 32.577 mm
R 207.0 °
M 4.784 mm
NIST
22 Dec 2016 13:40:37

Figure 7.3: SEM image of a 2.71 µm by 600 nm ridge waveguide design in silicon, overlaid with the simulated mode profile of the waveguide. The mode profile is visibly present in both the top cladding (air) and the bottom cladding (sapphire).

Here, the pump wavelength will be centered at 3 µm, so a dispersive wave would be expected beyond the ZDW from 3 µm.

7.3.3 Waveguide Design

The waveguide designs for each material are guided by fabrication challenges and limitations. The basic design is essentially a trapezoidal slab of the core waveguide material, either etched or deposited, surrounded by a substrate that behaves as the cladding for the waveguide.

7.3.3.1 Silicon Nitride Waveguide Design

The silicon nitride waveguides used in spectral generation in this chapter were provided by Tobias Kippenberg's group at EPFL. A cross-section of the waveguide design for silicon nitride is shown in Fig. 7.4. The waveguides were fabricated using the photonic Damascene process, in

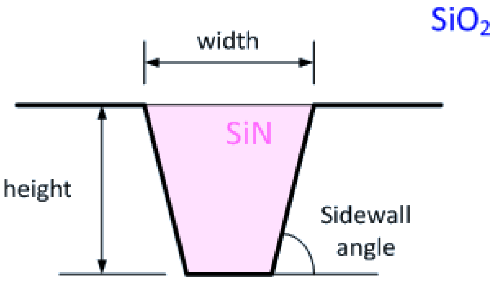

Figure 7.4: Diagram of the cross-section of a silicon nitride waveguide [58]. The core is comprised of silicon nitride, on a silica substrate. The core height is 2500 nm, the width varies from 1000 to 1600 nm, and the sidewall angle is 85°. The sidewalls are not a dispersion-oriented feature, but rather as a result of the Damascene process used in fabrication.

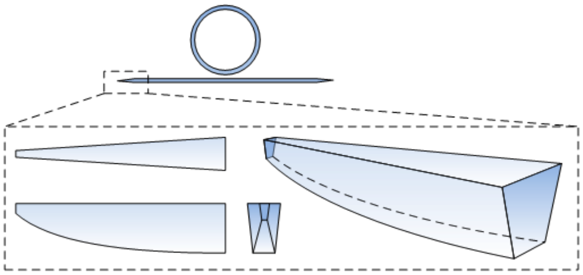

Figure 7.5: Design of the inversed taper in silicon nitride [58]. The tapers have a width of 560 nm, with the same waveguide height of 1900 nm.

which silicon nitride is deposited on a prestructured silica substrate using low-pressure chemical vapor deposition, and, after the surface of the silica is polished to remove excess silicon nitride, the top surface of the waveguide is deposited with silica to form the top cladding.

In the longitudinal direction, the chip length was 5 mm. Waveguide lengths ranged from 5 to 20 mm in 5 mm steps, where the longer waveguide designs incorporated a “paper clip” shape where the waveguide path doubles back upon itself in order to lengthen the path. At the input and output of these waveguides, an inversed taper was fabricated to facilitate coupling between the waveguide and free space (see Fig. 7.5). The tapers work by adiabatically shaping the beam mode from its focused spot size in free space to its final size within the waveguide, and are able to achieve a free-space coupling efficiency of 13%.

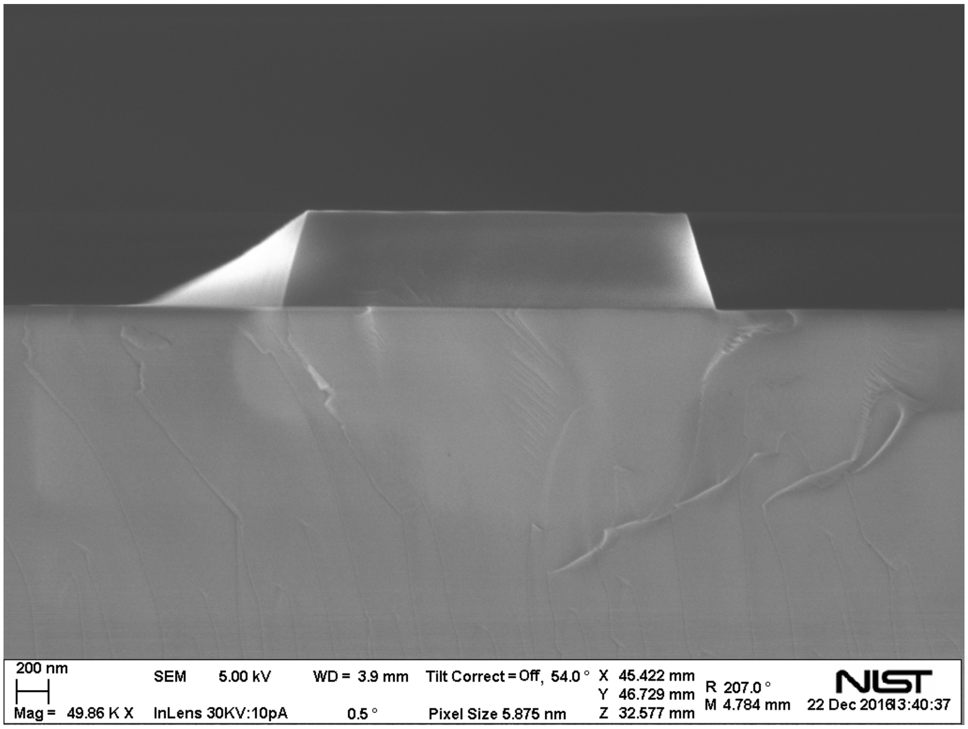
200 nm
SEM
5.00 kV
WD = 3.9 mm
Tilt Correct = Off, 54.0 °
X 45.422 mm
Y 46.729 mm
Z 32.577 mm
R 207.0 °
M 4.784 mm
NIST
Mag = 49.86 K X
InLens 30KV:10pA
0.5 °
Pixel Size 5.875 nm
22 Dec 2016 13:40:37

Figure 7.6: SEM image of a ridge waveguide design in silicon. The waveguide width in the image is 2.5 µm, with a height of 600 nm.

7.3.3.2 Silicon Waveguide Design

The silicon waveguides used for spectral broadening were designed and fabricated at NIST by Nima Nader and Jeff Shainline. The waveguides were created through etching the unwanted silicon away, leaving the waveguide, comprised of the remaining silicon, behind. The basic rectangular slab design (or “ridge”) is shown in an SEM image in Fig. 7.6.

In order to further control the waveguide dispersion, an added degree of geometrical complexity was introduced. For a waveguide constructed through etching, the simplest next step was to etch a notch into the waveguide. An SEM image of the resulting design is shown in Fig. 7.7. A number of parameters can be varied with the introduction of the notch — notch depth, notch width, and notch position — but for these waveguides, the notch depth was kept at 300 nm (half of the waveguide height) and the notch width was kept at 530 nm.

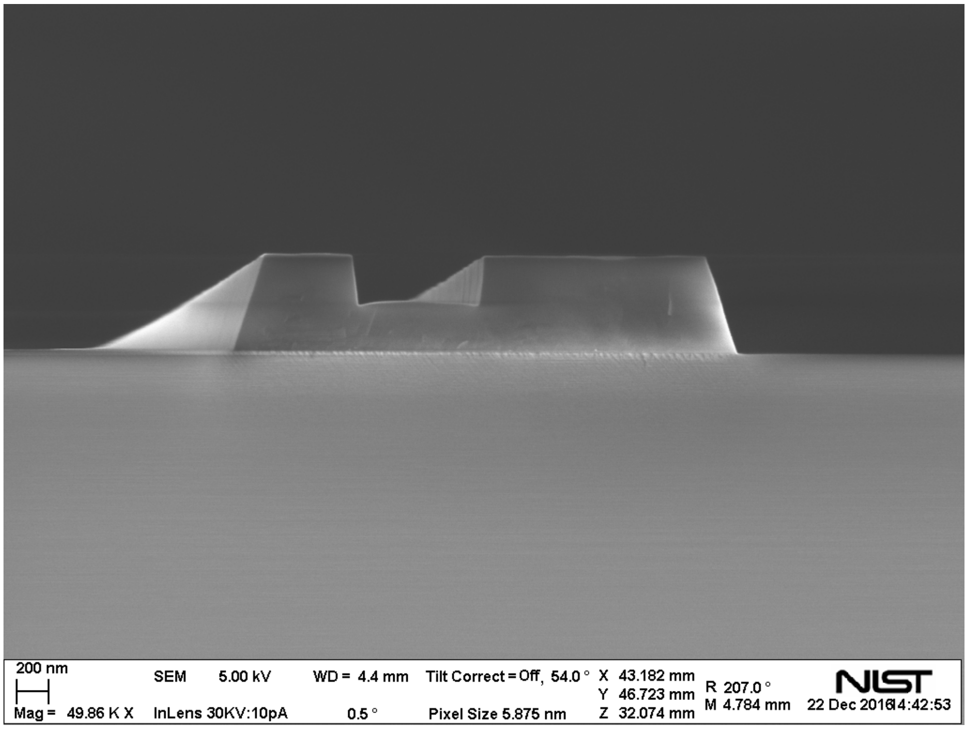
200 nm
Mag = 49.86 K X
SEM
5.00 kV
InLens 30KV:10pA
WD = 4.4 mm
0.5 °
Tilt Correct = Off, 54.0 °
Pixel Size 5.875 nm
X 43.182 mm
Y 46.723 mm
Z 32.074 mm
R 207.0 °
M 4.784 mm
NIST
22 Dec 2016 14:42:53

Figure 7.7: SEM image of a sample notch waveguide design in silicon. The notch width in the image is 0.8 µm, and the notch is offset from the center of the waveguide by 0.4 µm. The notch depth is 300 nm.

7.3.4 Dispersion Simulations

The dispersion of a waveguide can be determined through the use of a mode-solver program, which numerically solves Maxwell's equations using a set of boundary conditions introduced by the waveguide materials and geometry. These calculations provide an effective index of each geometry as a function of wavelength, yielding the waveguide's total dispersion. Python and MATLAB can perform these calculations, as well as more specialized software such as COMSOL (used for the silicon simulations) or Lumerical.

A sample image of a simulated mode area is shown in Fig. 7.3, for a 2.71 µm waveguide. For the silicon nitride waveguides, these were modeled by collaborators at EPFL for the TE and TM modes. For the silicon waveguides, these were modeled for ridge and notch designs. As wider and wider waveguides are simulated, the dispersion curves approach that of the bulk material, signifying that a larger portion of the mode is contained within the bulk material.

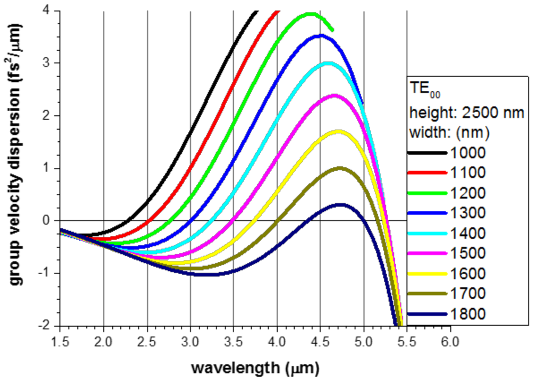

Figure 7.8: Dispersion as a function of wavelength for TE propagation in silicon nitride for nine different waveguide widths.

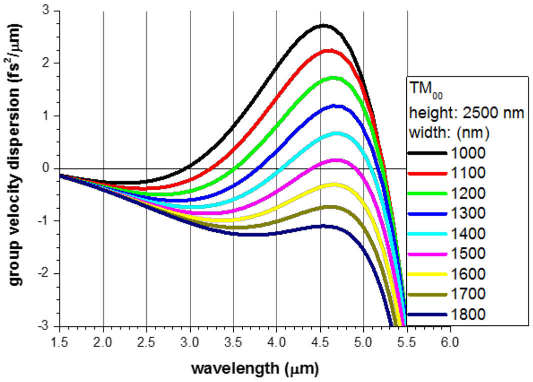

Figure 7.9: Dispersion as a function of wavelength for TM propagation in silicon nitride for nine different waveguide widths.

7.3.4.1 Dispersion Simulations in Silicon Nitride

The simulated dispersion profiles of the silicon nitride waveguides for TE and TM modes are shown in Figs. 7.8 and 7.9. Compared to the bulk dispersion of silicon nitride (Fig. 7.2), the introduced geometric dispersion is able to create regions of normal dispersion (whereas the bulk material exclusively exhibits anomalous dispersion), and additionally an extended wavelength region of low, anomalous dispersion. As a result, soliton formation is supported at a range of wavelengths, depending on power and the waveguide width, and dispersive wave generation is also

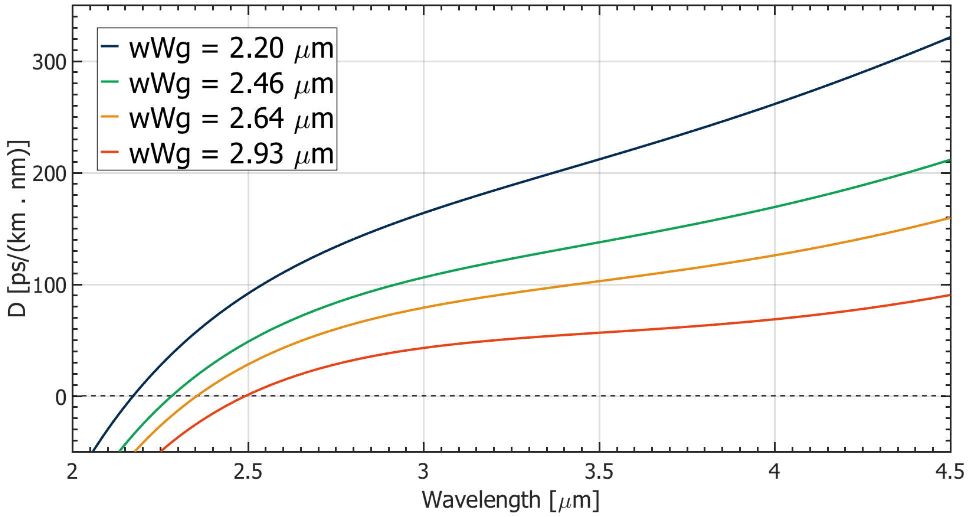

Figure 7.10: Dispersion as a function of wavelength for ridge waveguides in silicon for four different waveguide widths.

supported across a range of wavelengths, as can be seen by the position of the ZDWs.

7.3.4.2 Dispersion Simulations in Silicon Ridge Waveguides

The effect of varying waveguide widths (denoted in the figure as wWg) can similarly be seen in silicon in Fig. 7.10. It is again evident how the effect of geometric dispersion alters the dispersion of the waveguides as compared to the bulk material. Rather than possessing normal dispersion throughout the mid-infrared window exhibited by bulk silicon, geometric dispersion introduces anomalous dispersion, generating ZDWs between 2 and 2.5 µm and supporting soliton formation in the anomalous dispersion regime at longer wavelengths.

7.3.4.3 Dispersion Simulations in Silicon Notch Waveguides

In a notched waveguide design, there are several parameters that can be adjusted (notch width, notch depth, notch position); however, this array of simulations were limited to a fixed notch width of 530 nm, a fixed notch depth of 300 nm (half the height), with variation in the notch position (nP), measured from the center. The notch has a significantly different effect on

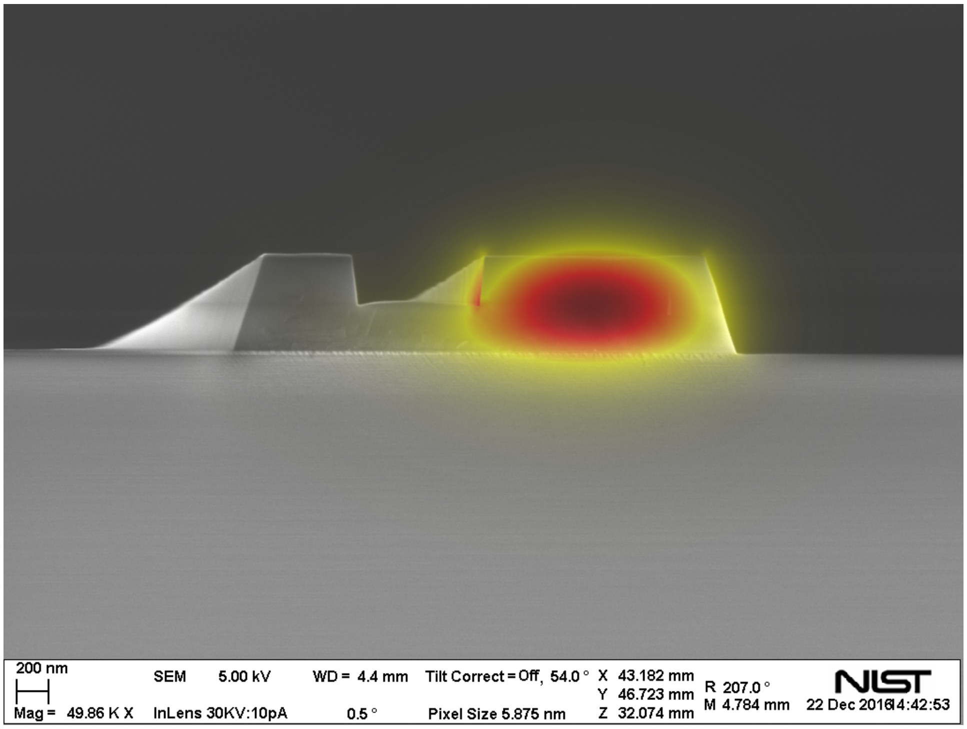
200 nm
Mag = 49.86 K X
SEM
5.00 kV
InLens 30KV:10pA
WD = 4.4 mm
0.5 °
Tilt Correct = Off, 54.0 °
Pixel Size 5.875 nm
X 43.182 mm
Y 46.723 mm
Z 32.074 mm
R 207.0 °
M 4.784 mm
NIST
22 Dec 2016 14:42:53

Figure 7.11: SEM image of a notch waveguide design in silicon, overlaid with the mode profile of the waveguide.

the waveguide mode, as can be seen in Fig. 7.11. Between 5 and 10 % of the mode power is in the air gap within the notch, and the mode extends throughout the notch and into the silicon core opposite the central mode.

The effect of this notch can be seen in Fig. 7.12. In comparison to the ridge simulations in Fig. 7.10, the notch waveguides experience a second ZDW at a longer wavelength, and exhibit normal dispersion at longer wavelengths. A notch at the center (nP = 0 nm) has a ZDW near 3 µm, whereas a notch further from the center (nP = 600 nm) has a ZDW at 4.2 µm. Through the phase-matching condition highlighted earlier, this supports the generation of a dispersive wave at longer wavelengths.

7.3.4.4 Dispersion Simulations in Silicon: Broadest Output Spectra

In addition to the two surveys of waveguide parameters shown in Figs. 7.10 and 7.12, dispersion simulations for the two waveguides that produced the broadest output spectra of each type

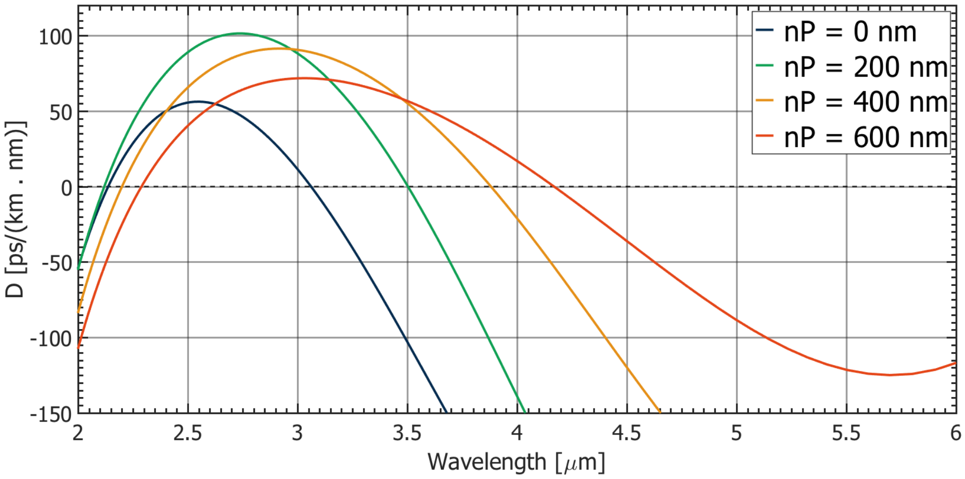

Figure 7.12: Dispersion as a function of wavelength for notch waveguides in silicon for four different notch positions.

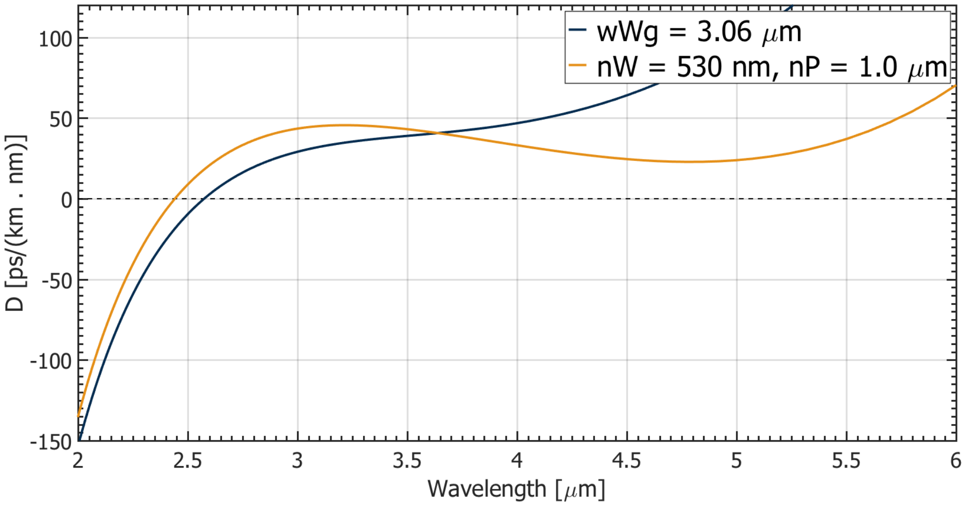

Figure 7.13: Dispersion as a function of wavelength for the two most promising waveguide designs in silicon: a ridge waveguide with a width of 3.06 µm and a notch waveguide with a notch position of 1 µm.

are shown in Fig. 7.13. Both simulations demonstrate anomalous dispersion at and beyond 3 µm.

7.4 Waveguide Spectral Broadening

The waveguides modeled in Sec. 7.3.3 were pumped with the high power, 3 µm source detailed in Chapter 5. The difference frequency generation (DFG) source was operated at 100 mW output power, with pulse durations measured to be roughly 100 fs. 86 mW of the source reached the waveguides after steering and focusing optics. The output spectra of different waveguides were recorded with a Fourier-transform infrared spectrometer (FTIR). The waveguides show different broadening performance depending on their GVD profiles. Spectral broadening was not simulated in each case because of the dependence on peak power, which is highly variable as a result of the coupling efficiency. Instead, waveguide choices were based on a rough estimate of spectral behavior using the simulated dispersion curves.

7.4.1 Spectral Broadening in Silicon Nitride

Fig. 7.14 shows spectra generated from a 20-mm-long waveguide for five different waveguide widths, as well as the 3 µm pump used for reference. While waveguides with lengths of 5, 10, and 15 mm were provided by EPFL as well, the 20 mm waveguides were the only ones able to exhibit broadening. Slight variation in spectral shape is evident from varying the waveguide GVD; the central wavelength shifted to longer wavelengths for all waveguides, but more so for the wider waveguides. All generated light at both 2.9 µm and 3.3 µm, with the boosted power in the 1600 nm waveguide able to broaden beyond 2.9 µm to 2.8 µm. These were coupled into the TE mode of the waveguide; however, no discernable difference in the output was evident as the input polarization was rotated. While an exhaustive study was not conducted using the silicon nitride waveguides, the results indicate the current peak power in the waveguide was insufficient to generate substantial broadening, and higher peak power would be required to generate the degree of broadening seen in silicon.

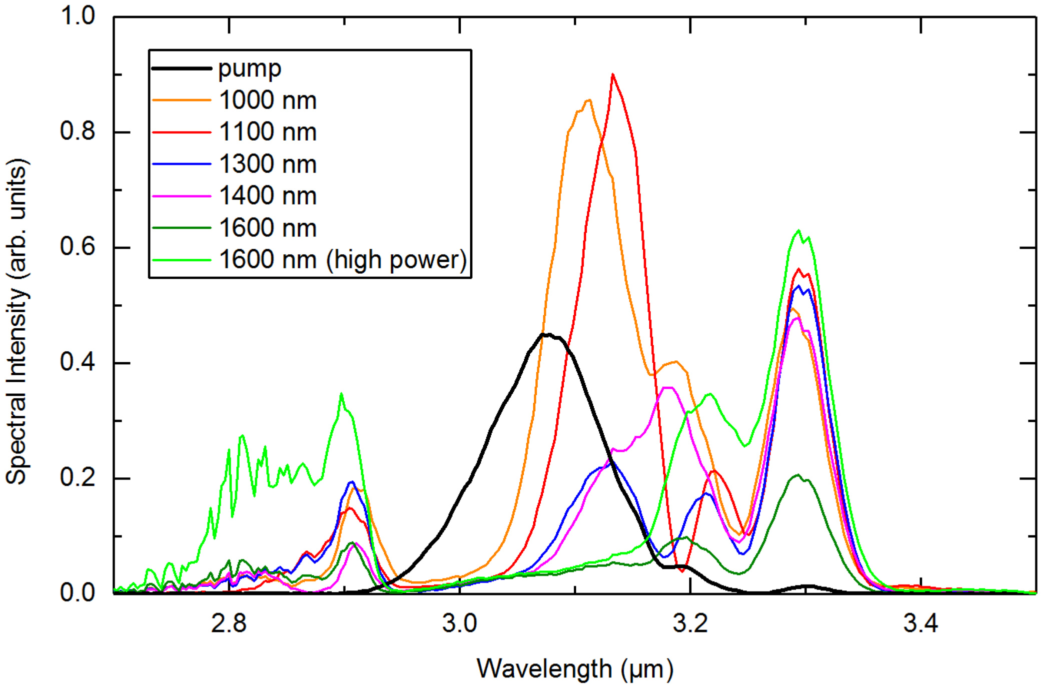

Figure 7.14: Normalized spectra for the pump and five different 20-mm-long silicon nitride waveguides, with widths ranging from 1000 to 1600 nm. An additional spectrum at the 1600 nm width was retrieved with the 3 µm source power increased by 25 %.

7.4.2 Spectral Broadening in Silicon

In comparison to the silicon nitride waveguides, the high-nonlinearity silicon waveguides demonstrated significant broadening. The waveguides from the three simulated dispersion plots (Figs. 7.10, 7.12, and 7.13) were pumped, and the generated spectra are shown in Figs. 7.15, 7.16, and 7.17. The simpler ridge waveguide outputs are shown in Fig. 7.15, in addition to the 3 µm pump. Here, the waveguide output wavelength exhibits a strong dependence on waveguide width, with spectra possible out to 4 µm.

Through the use of notches, however, these spectra can reach much further into the mid-infrared, as seen in Fig. 7.16. In comparison to the dispersion plot (Fig. 7.12), it is evident that the generated dispersive wave was in fact formed across the ZDW from the pump wavelength. The spectral range achievable with a ridge waveguide surpassed that of the PPLN-based system from Chapter 6. The best spectral coverage from each design (ridge and notch) are shown fully in

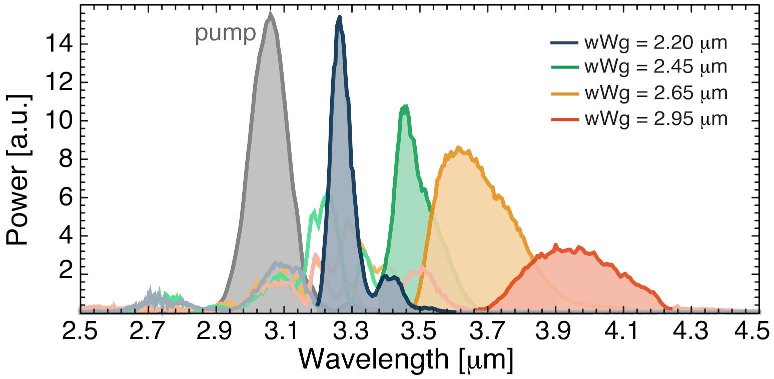

Figure 7.15: Spectra from the four ridge waveguide designs in silicon simulated in Fig. 7.10. The waveguides with lower 3 µm dispersion are able to generate spectra at longer wavelengths.

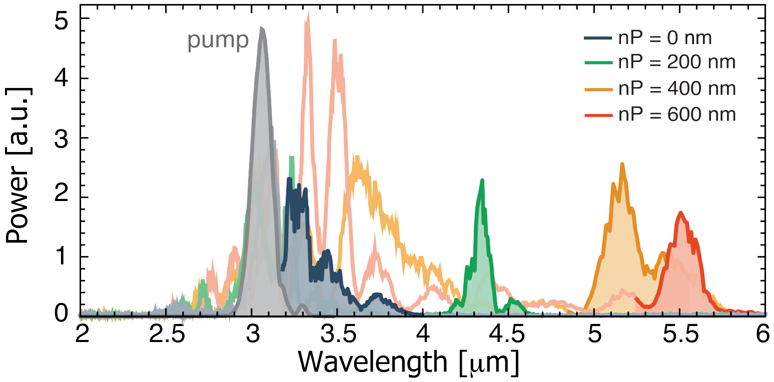

Figure 7.16: Spectra from the four notch waveguide designs in silicon simulated in Fig. 7.12. The wider notches, which have longer-wavelength zero crossings in Fig. 7.12, generate spectra at longer wavelengths.

Fig. 7.17. The simultaneous bandwidth demonstrated significantly exceeds that from PPLN, as phase-matching bandwidth is no longer a limiting factor.

7.5 RIN in Silicon

Fig. 7.18 presents the RIN spectra of the waveguide output compared to that of the 3 µm pump. Some RIN is acquired at lower frequencies, but additional RIN is largely not introduced as a result of broadening in the waveguides.

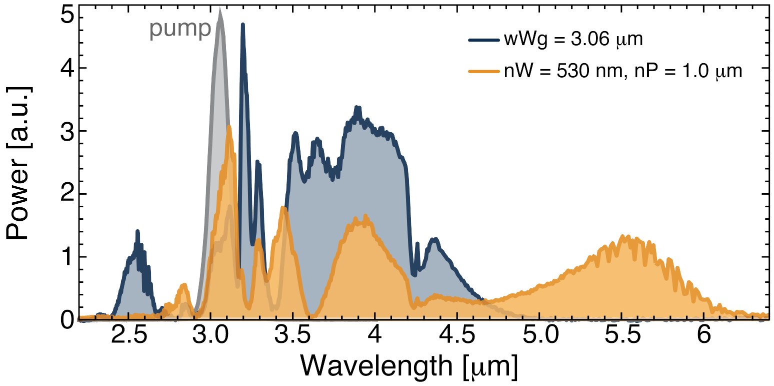

Figure 7.17: Spectra from the two waveguide designs in silicon simulated in Fig. 7.13, along with the 3 µm pump. The notched waveguide, in yellow, spans an octave, from below 3 µm to beyond 6 µm. The ridge waveguide, in blue, is also able to generate a broad spectrum spanning nearly an octave, from 2.5 µm to nearly 5 µm.

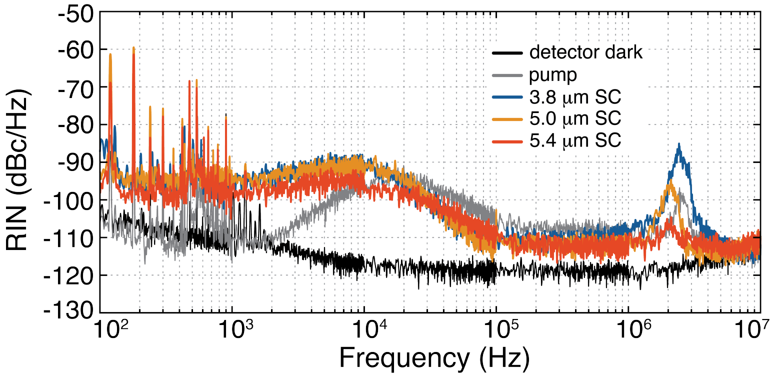

Figure 7.18: The relative intensity noise (RIN) of the generated supercontinuua as compared to that of the pump and the dark detector.

7.6 5 µm Dual Comb Spectroscopy with Output of Silicon Waveguide

In both a test of coherence and a demonstration of an exciting application, the output of the silicon waveguide was heterodyned with the output from the broadly tunable DFG source in Chapter 6. This was performed at 4.8 µm, at a strong absorption feature of the molecule carbonyl sulfide (OCS). The top of Fig. 7.19 shows the measured pulse train of ten interferograms in a 20 ms time span; with a repetition rate difference of 512 Hz, a heterodyne beat occurred every ~ 2 ms. The center burst of the heterodyne signal along with the molecular free induction decay from an OCS sample was measured in a 20 µs time span and presented at bottom in Fig. 7.19.

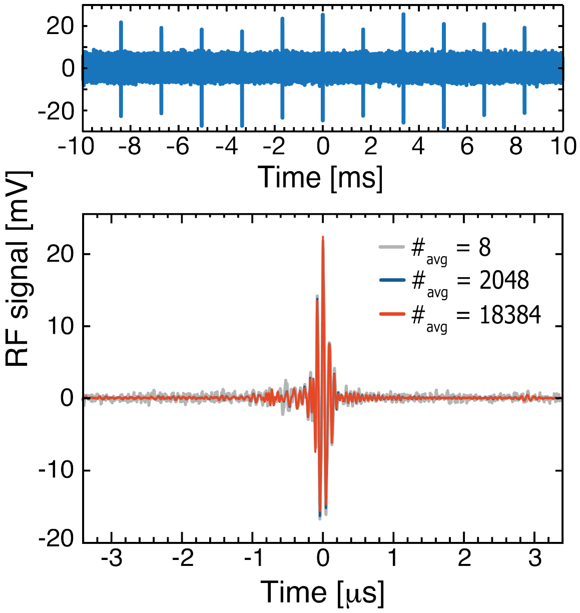

Figure 7.19: Top: train of interferograms of the heterodyne beat between the silicon waveguide output and the long-wave DFG output at 4.8 µm. Bottom: single interferogram of the heterodyne beat, with three different averages shown.

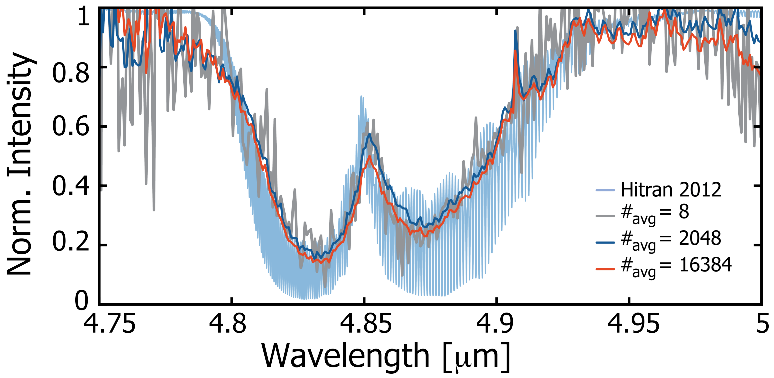

Figure 7.20: Fourier transform of the heterodyne beat interferogram, overlaid with the HITRAN spectrum of carbonyl sulfide (OCS). Transforms are plotted for three different averages. While individual ro-vibrational absorptions are unable to be resolved, the broader absorption branches are well-resolved.

Data was averaged for 16384 interferograms without losing spectral features, as evidenced by the Fourier-transform-calculated optical spectrum (Fig. 7.20).

The optical spectrum of the dual comb system with imprinted OCS absorption was obtained by calculating the Fourier transform of the averaged interferograms. The measured data was compared to a reference spectrum from the HITRAN2012 [55] database in Fig. 7.20. The measured spectra closely overlap with the database reference, although they lack the fine resolution to fully resolve the ro-vibrational lines. However, the lower resolution of these measurements is attributed to the hardware limitations of the data acquisition technique.

7.7 Conclusion

This chapter presented an exciting development in the direction of the generation of broadband mid-infrared spectra, and showed the tunability, coherence, and a first application of the waveguide output in silicon. In the future, a suspended waveguide design with silicon and gallium arsenide will enable longer wavelength generation. Additionally, on-chip integration can enable dual-comb detection entirely on a more robust, integrated platform. If pump generation can also occur in a less bulky framework without free-space optics, this shows enormous potential in migrating this technology towards much a more compact, robust, and integrated platform.

Chapter 8

Conclusion

The field of mid-infrared frequency comb spectroscopy is growing and developing rapidly, and the Optical Frequency Measurements Group at NIST has been one of the groups at the forefront of source development. Using the developments from previous work featuring low-power and less coherent sources, I have developed high-power, broadband, widely tunable sources and successfully demonstrated basic absorption measurements using dual comb spectroscopy. The success of mid-infrared spectral broadening in waveguides helped to push mid-infrared frequency combs away from bulky, table-top, free-space experiments and towards chip-scale devices in the direction of eventual viability for field applications.

This thesis first detailed the importance of frequency combs and the plethora of methods by which broadband, coherent mid-infrared radiation is generated. After summarizing the nonlinear optics behind the processes used in mid-infrared frequency comb generation, the thesis outlined the many projects in which I have been involved which propelled this field forward: an optical parametric oscillator, erbium-doped fiber amplifiers, difference frequency generation (both with high power at 3 µm and broadly tunable between 2.6 and 5.2 µm), and silicon and silicon nitride waveguide pumping. The three- and four-wave mixing modeling developed for this work has been immensely valuable for nonlinear simulation both within the Optical Frequency Measurements Group and elsewhere, available for public use at `github.com/pyNLO`.

The mid-infrared spectral region has largely been overlooked in the development of frequency combs, and we are on the verge of filling in this gap with the coherent, low-noise, broadband sources that have been well-established at shorter wavelengths. This thesis lays the groundwork for future research in the mid-infrared and begins to explore the promising direction of silicon and silicon nitride chip-scale nonlinear devices. Through the use of highly nonlinear fiber (HNLF), coherent, broadband mid-infrared radiation has been achieved across the entire transmission window of periodically-poled lithium niobate (PPLN).

In the future, difference frequency generation can extend from the mid-infrared, through the far-infrared, and eventually into the terahertz regime through the choice of appropriate materials and input wavelengths. $\chi^{(2)}$ materials transparent beyond 6 µm, such as gallium arsenide and gallium phosphide, are already being seeded with pump-signal combinations in order to enable spectral generation beyond 10 µm. Chip-based mid-infrared platforms can be extended beyond the spectral broadening explored in this dissertation to eventual on-chip difference frequency generation and switching networks into different waveguides of varying dispersion, yielding dispersive waves throughout the mid-infrared region. Lastly, a combination of more stable sources, portable technology, and new wavelengths permit fieldable spectral measurements of larger molecules useful for defense and industrial applications. The inherent coherent and broadband nature of frequency combs enables this degree of sensitivity across molecular absorption features, and the technology explored in this thesis helps to bring these properties into spectral regimes useful for numerous applications.

Bibliography

[1] J. Ye, S.T. Cundiff (eds.), Femtosecond Optical Frequency Comb: Principle, Operation, and Applications (Springer Nature, 2005)

[2] Quantum Electronics and Photonics Division, National Institute of Science and Technology (NIST). Spectral combs from UV to THz (SCOUT) proposal: Broadband dual-comb spectrometry for hazardous material detection (2014)

[3] E. Baumann, F.R. Giorgetta, W.C. Swann, A.M. Zolot, I. Coddington, N.R. Newbury, Phys. Rev. A **84**, 062513 (2011)

[4] O. Chalus, P.K. Bates, M. Smolarski, J. Biegert, Opt. Express **17**(5), 3587 (2009)

[5] C. Erny, K. Moutzouris, J. Biegert, D. Kühlke, F. Adler, A. Leitenstorfer, U. Keller, Opt. Lett. **32**(9), 1138 (2007)

[6] I. Galli, F. Cappelli, P. Cancio, G. Giusfredi, D. Mazzotti, S. Bartalini, P. De Natale, Opt. Express **21**(23), 28877 (2013)

[7] A. Gambetta, R. Ramponi, M. Marangoni, Opt. Lett. **33**(22), 2671 (2008)

[8] A. Gambetta, N. Coluccelli, M. Cassinerio, D. Gatti, P. Laporta, G. Galzerano, M. Marangoni, Opt. Lett. **38**(7), 1155 (2013)

[9] C. Hu, W. Yue, T. Chen, P. Jiang, B. Wu, Y. Shen, Appl. Opt. **56**(6), 1574 (2017)

[10] K. Iwakuni, S. Okubo, O. Tadanaga, H. Inaba, A. Onae, F.L. Hong, H. Sasada, Opt. Lett. **41**(17), 3980 (2016)

[11] L. Jin, M. Yamanaka, V. Sonnenschein, H. Tomita, T. Iguchi, A. Sato, T. Oh-hara, N. Nishizawa, App. Phys. Express **10**(1), 012503 (2016)

[12] F. Keilmann, S. Amarie, J. Infrared Millim. Terahertz Waves **33**(5), 479 (2012)

[13] J. Krauth, A. Steinmann, R. Hegenbarth, M. Conforti, H. Giessen, Opt. Express **21**(9), 11516 (2013)

[14] S.A. Meek, A. Poisson, G. Guelachvili, T.W. Hänsch, N. Picqué, Applied Physics B **114**(4), 573 (2014)

[15] R.T. Murray, T.H. Runcorn, E.J.R. Kelleher, J.R. Taylor, Opt. Lett. **41**(11), 2446 (2016)

[16] T.W. Neely, T.A. Johnson, S.A. Diddams, Opt. Lett. **36**(20), 4020 (2011)

[17] C. Phillips, J. Jiang, C. Mohr, A. Lin, C. Langrock, M. Snure, D. Bliss, M. Zhu, I. Hartl, J. Harris, et al., Opt. Lett. **37**(14), 2928 (2012)

[18] I. Pupeza, D. Sánchez, J. Zhang, N. Lilienfein, M. Seidel, N. Karpowicz, T. Paasch-Colberg, I. Znakovskaya, M. Pescher, W. Schweinberger, et al., Nature Photonics **9**(11), 721 (2015)

[19] A. Ruehl, A. Gambetta, I. Hartl, M.E. Fermann, K.S.E. Eikema, M. Marangoni, Opt. Lett. **37**(12), 2232 (2012)

[20] T. Steinle, F. Mörz, A. Steinmann, H. Giessen, Opt. Lett. **41**(21), 4863 (2016)

[21] M. Tsuzuki, L. Jin, M. Yamanaka, V. Sonnenchein, H. Tomita, A. Sato, T. Ohara, Y. Sakakibara, E. Omoda, H. Kataura, et al., Photonics Research **4**(6), 313 (2016)

[22] D.G. Winters, P. Schlup, R.A. Bartels, Opt. Lett. **35**(13), 2179 (2010)

[23] Y. Yao, W.H. Knox, Opt. Express **21**(22), 26612 (2013)

[24] F. Zhu, H. Hundertmark, A.A. Kolomenskii, J. Strohaber, R. Holzwarth, H.A. Schuessler, Opt. Lett. **38**(13), 2360 (2013)

[25] F. Adler, K.C. Cossel, M.J. Thorpe, I. Hartl, M.E. Fermann, J. Ye, Opt. Lett. **34**(9), 1330 (2009)

[26] K. Balskus, Z. Zhang, R.A. McCracken, D.T. Reid, Opt. Lett. **40**(17), 4178 (2015)

[27] Y. Jin, S.M. Cristescu, F.J.M. Harren, J. Mandon, Applied Physics B **119**(1), 65 (2015)

[28] N. Leindecker, A. Marandi, R.L. Byer, K.L. Vodopyanov, Opt. Express **19**(7), 6296 (2011)

[29] L. Maidment, P.G. Schunemann, D.T. Reid, Opt. Lett. **41**(18), 4261 (2016)

[30] V.O. Smolski, S. Vasilyev, P.G. Schunemann, S.B. Mirov, K.L. Vodopyanov, Opt. Lett. **40**(12), 2906 (2015)

[31] Z. Zhang, R.J. Clewes, C.R. Howle, D.T. Reid, Opt. Lett. **39**(20), 6005 (2014)

[32] O. Cathabard, R. Teissier, J. Devenson, A.N. Baranov, Electronics Letters **45**(20), 1028 (2009)

[33] Daylight solutions ⟩⟩ quantum cascade lasers. `http://www.daylightsolutions.com/technology/qcl_technology.htm`. Accessed: 2017-02-27

[34] F. Fuchs, S. Hugger, M. Kinzer, R. Aidam, W. Bronner, R. Lösch, Q. Yang, K. Degreif, F. Schnürer, Optical Engineering **49**(11), 111127 (2010)

[35] A. Hugi, R. Terazzi, Y. Bonetti, A. Wittmann, M. Fischer, M. Beck, J. Faist, E. Gini, Applied Physics Letters **95**(6), 061103 (2009)

[36] A. Hugi, G. Villares, S. Blaser, H.C. Liu, J. Faist, Nature **492**(7428), 229 (2012)

[37] A. Lyakh, R. Maulini, A. Tsekoun, R. Go, C. Pflgl, L. Diehl, Q.J. Wang, F. Capasso, C.K.N. Patel, Applied Physics Letters **95**(14), 141113 (2009)

[38] M.B. Pushkarsky, I.G. Dunayevskiy, M. Prasanna, A.G. Tsekoun, R. Go, C.K.N. Patel, Proceedings of the National Academy of Sciences **103**(52), 19630 (2006)

[39] A. Spott, J. Peters, M.L. Davenport, E.J. Stanton, C.D. Merritt, W.W. Bewley, I. Vurgaftman, C.S. Kim, J.R. Meyer, J. Kirch, L.J. Mawst, D. Botez, J.E. Bowers, Optica **3**(5), 545 (2016)

[40] G. Villares, A. Hugi, S. Blaser, J. Faist, Nature Communications **5**, 5192 (2014)

[41] S. Duval, M. Bernier, V. Fortin, J. Genest, M. Piché, R. Vallée, Optica **2**(7), 623 (2015)

[42] I.T. Sorokina, V.V. Dvoyrin, N. Tolstik, E. Sorokin, IEEE Journal of Selected Topics in Quantum Electronics **20**(5), 99 (2014)

[43] S. Vasilyev, I. Moskalev, M. Mirov, S. Mirov, V. Gapontsev, Opt. Lett. **40**(21), 5054 (2015)

[44] B. Kuyken, T. Ideguchi, S. Holzner, M. Yan, T.W. Hänsch, J. Van Campenhout, P. Verheyen, S. Coen, F. Leo, R. Baets, et al., Nature Communications **6** (2015)

[45] A. Marandi, C.W. Rudy, V.G. Plotnichenko, E.M. Dianov, K.L. Vodopyanov, R.L. Byer, Opt. Express **20**(22), 24218 (2012)

[46] S. Xie, N. Tolstik, J.C. Travers, E. Sorokin, C. Caillaud, J. Troles, P.S. Russell, I.T. Sorokina, Opt. Express **24**(11), 12406 (2016)

[47] A.G. Griffith, R.K.W. Lau, J. Cardenas, Y. Okawachi, A. Mohanty, R. Fain, Y.H.D. Lee, M. Yu, C.T. Phare, C.B. Poitras, A.L. Gaeta, M. Lipson, Nature Communications **6**, 6299 (2015)

[48] K. Luke, Y. Okawachi, M.R.E. Lamont, A.L. Gaeta, M. Lipson, Opt. Lett. **40**(21), 4823 (2015)

[49] C.Y. Wang, T. Herr, P. DelHaye, A. Schliesser, J. Hofer, R. Holzwarth, T. Hänsch, N. Picqué, T.J. Kippenberg, Nature Communications **4**, 1345 (2013)

[50] M. Yu, Y. Okawachi, A.G. Griffith, M. Lipson, A.L. Gaeta, Optica **3**(8), 854 (2016)

[51] F.C. Cruz, D.L. Maser, T. Johnson, G. Ycas, A. Klose, F.R. Giorgetta, I. Coddington, S.A. Diddams, Opt. Express **23**(20), 26814 (2015)

[52] D.L. Maser, L. Nugent-Glandorf, G. Ycas, F. Adler, K. Knabe, S.A. Diddams, in CLEO: 2014 (Optical Society of America, 2014), p. JTu4A.110

[53] D.L. Maser, G. Ycas, W.I. Depetri, F.C. Cruz, S.A. Diddams, Applied Physics B **123**(5), 142 (2017)

[54] J. Hult, Journal of Lightwave Technology **25**(12), 3770 (2007)

[55] L. Rothman, I. Gordon, Y. Babikov, A. Barbe, D.C. Benner, P. Bernath, M. Birk, L. Bizzocchi, V. Boudon, L. Brown, A. Campargue, K. Chance, E. Cohen, L. Coudert, V. Devi, B. Drouin, A. Fayt, J.M. Flaud, R. Gamache, J. Harrison, J.M. Hartmann, C. Hill, J. Hodges, D. Jacquemart, A. Jolly, J. Lamouroux, R.L. Roy, G. Li, D. Long, O. Lyulin, C. Mackie, S. Massie, S. Mikhailenko, H. Müller, O. Naumenko, A. Nikitin, J. Orphal, V. Perevalov,

A. Perrin, E. Polovtseva, C. Richard, M. Smith, E. Starikova, K. Sung, S. Tashkun, J. Tennyson, G. Toon, V. Tyuterev, G. Wagner, Journal of Quantitative Spectroscopy and Radiative Transfer **130**, 4 (2013)

[56] M. Leidinger, S. Fieberg, N. Waasem, F. Kühnemann, K. Buse, I. Breunig, Opt. Express **23**(17), 21690 (2015)

[57] C.D. Salzberg, J.J. Villa, J. Opt. Soc. Am. **47**(3), 244 (1957)

[58] M.H.P. Pfeiffer, A. Kordts, V. Brasch, M. Zervas, M. Geiselmann, J.D. Jost, T.J. Kippenberg, Optica **3**(1), 20 (2016)

[59] R.A. Sawyer, Experimental Spectroscopy, 3rd edn. (Dover Publications, Inc., 1963)

[60] I. Newton, Philosophical Transactions **6**(69-80), 3075 (1671)

[61] T. Melvill, Physical and Literary Essays, Edinburgh (1752)

[62] W.H. Wollaston, Philosophical Transactions of the Royal Society of London **92**, 365 (1802)

[63] J. Fraunhofer, Annalen der Physik **56**(7), 264 (1817)

[64] G. Kirchhoff, The London, Edinburgh, and Dublin Philosophical Magazine and Journal of Science **20**(130), 1 (1860)

[65] G. Kirchhoff, R. Bunsen, Annalen der Physik **186**(6), 161 (1860)

[66] J.N. Lockyer, Philosophical Transactions of the Royal Society of London **163**, 253 (1873)

[67] I. Galli, S. Bartalini, S. Borri, P. Cancio, D. Mazzotti, P. De Natale, G. Giusfredi, Phys. Rev. Lett. **107**, 270802 (2011)

[68] S.A. Diddams, L. Hollberg, V. Mbele, Nature **445**(7128), 627 (2007)

[69] K.C. Cossel, F. Adler, K.A. Bertness, M.J. Thorpe, J. Feng, M.W. Raynor, J. Ye, Applied Physics B **100**(4), 917 (2010)

[70] M.J. Thorpe, D. Balslev-Clausen, M.S. Kirchner, J. Ye, Opt. Express **16**(4), 2387 (2008)

[71] C. Wang, P. Sahay, Sensors **9**(10), 8230 (2009)

[72] L.C. Sinclair, I. Coddington, W.C. Swann, G.B. Rieker, A. Hati, K. Iwakuni, N.R. Newbury, Opt. Express **22**(6), 6996 (2014)

[73] G.B. Rieker, F.R. Giorgetta, W.C. Swann, J. Kofler, A.M. Zolot, L.C. Sinclair, E. Baumann, C. Cromer, G. Petron, C. Sweeney, P.P. Tans, I. Coddington, N.R. Newbury, Optica **1**(5), 290 (2014)

[74] A. Klose, G. Ycas, D.L. Maser, S.A. Diddams, Opt. Express **22**(23), 28400 (2014)

[75] A. Klose, G. Ycas, F.C. Cruz, D.L. Maser, S.A. Diddams, Applied Physics B **122**(4), 78 (2016)

[76] G.W. Truong, E.M. Waxman, K.C. Cossel, E. Baumann, A. Klose, F.R. Giorgetta, W.C. Swann, N.R. Newbury, I. Coddington, Opt. Express **24**(26), 30495 (2016)

[77] A. Dax, J.S. Wells, L. Hollberg, A.G. Maki, W. Urban, Journal of Molecular Spectroscopy **168**(2), 416 (1994)

[78] M. Mürtz, M. Schaefer, T. George, J. Wells, W. Urban, Applied Physics B: Lasers and Optics **60**(1), 31 (1995)

[79] M. Mürtz, J. Wells, L. Hollberg, T. Zibrova, N. Mackie, Applied Physics B: Lasers and Optics **66**(3), 277 (1998)

[80] B.J. Bjork, T.Q. Bui, O.H. Heckl, P.B. Changala, B. Spaun, P. Heu, D. Follman, C. Deutsch, G.D. Cole, M. Aspelmeyer, et al., Science **354**(6311), 444 (2016)

[81] A.J. Fleisher, B.J. Bjork, T.Q. Bui, K.C. Cossel, M. Okumura, J. Ye, The Journal of Physical Chemistry Letters **5**(13), 2241 (2014)

[82] P. Weibring, D. Richter, J.G. Walega, A. Fried, Opt. Express **15**(21), 13476 (2007)

[83] K.C. Cossel, E.M. Waxman, I.A. Finneran, G.A. Blake, J. Ye, N.R. Newbury, JOSA B **34**(1), 104 (2017)

[84] F. Tittel, D. Richter, A. Fried, in Solid-State Mid-Infrared Laser Sources, ed. by I.T. Sorokina, K.L. Vodopyanov (Springer-Verlag, 2003)

[85] C. Bauer, A. Sharma, U. Willer, J. Burgmeier, B. Braunschweig, W. Schade, S. Blaser, L. Hvozdara, A. Müller, G. Holl, Applied Physics B **92**(3), 327 (2008)

[86] F. Fuchs, B. Hinkov, S. Hugger, J.M. Kaster, R. Aidam, W. Bronner, K. Köhler, Q. Yang, S. Rademacher, K. Degreif, et al., in OPTO (International Society for Optics and Photonics, 2010), pp. 760,809–760,809

[87] R. Furstenberg, C. Kendziora, J. Stepnowski, S. Stepnowski, M. Rake, M. Papantonakis, V. Nguyen, G. Hubler, R. McGill, Applied Physics Letters **93**(22), 224103 (2008)

[88] R. Harig, R. Braun, C. Dyer, C. Howle, B. Truscott, Opt. Express **16**(8), 5708 (2008)

[89] D.S. Moore, Sensing and Imaging: An International Journal **8**(1), 9 (2007)

[90] M.W. Todd, R.A. Provencal, T.G. Owano, B.A. Paldus, A. Kachanov, K.L. Vodopyanov, M. Hunter, S.L. Coy, J.I. Steinfeld, J.T. Arnold, Applied Physics B **75**(2-3), 367 (2002)

[91] S. Wallin, A. Pettersson, H. Östmark, A. Hobro, Analytical and Bioanalytical Chemistry **395**(2), 259 (2009)

[92] T.A. Johnson, S.A. Diddams, Applied Physics B **107**(1), 31 (2012)

[93] H. Kapteyn, O. Cohen, I. Christov, M. Murnane, Science **317**(5839), 775 (2007)

[94] M.C. Chen, C. Mancuso, C. Hernndez-Garca, F. Dollar, B. Galloway, D. Popmintchev, P.C. Huang, B. Walker, L. Plaja, A.A. Jaro-Becker, A. Becker, M.M. Murnane, H.C. Kapteyn, T. Popmintchev, Proceedings of the National Academy of Sciences **111**(23), E2361 (2014)

[95] T. Popmintchev, M.C. Chen, D. Popmintchev, P. Arpin, S. Brown, S. Ališauskas, G. Andriukaitis, T. Balčiunas, O.D. Mücke, A. Pugzlys, et al., Science **336**(6086), 1287 (2012)

[96] E.A. Muller, B. Pollard, M.B. Raschke, The Journal of Physical Chemistry Letters **6**(7), 1275 (2015)

[97] S. Amarie, T. Ganz, F. Keilmann, Opt. Express **17**(24), 21794 (2009)

[98] B. Darquié, C. Stoeffler, A. Shelkovnikov, C. Daussy, A. Amy-Klein, C. Chardonnet, S. Zrig, L. Guy, J. Crassous, P. Soulard, et al., Chirality **22**(10), 870 (2010)

[99] F. Rust, Science **211**(4486), 1044 (1981)

[100] M. Lezius, T. Wilken, C. Deutsch, M. Giunta, O. Mandel, A. Thaller, V. Schkolnik, M. Schiemangk, A. Dinkelaker, A. Kohfeldt, et al., Optica **3**(12), 1381 (2016)

[101] A. Sell, G. Krauss, R. Scheu, R. Huber, A. Leitenstorfer, Opt. Express **17**(2), 1070 (2009)

[102] G. Ycas, S. Osterman, S.A. Diddams, Opt. Lett. **37**(12), 2199 (2012)

[103] D.L. Maser, F.C. Cruz, G. Ycas, T. Johnson, A. Klose, F. Giorgetta, L.C. Sinclair, I. Coddington, N.R. Newbury, S. Diddams, in Frontiers in Optics 2015 (Optical Society of America, 2015), p. FTu2E.3

[104] D. Maser, G. Ycas, F. Cruz, S. Diddams, in Frontiers in Optics 2016 (Optical Society of America, 2016), p. JTh2A.85

[105] J.C. Gauthier, V. Fortin, S. Duval, R. Vallée, M. Bernier, Opt. Lett. **40**(22), 5247 (2015)

[106] Y. Tang, L.G. Wright, K. Charan, T. Wang, C. Xu, F.W. Wise, Optica **3**(9), 948 (2016)

[107] R. Thapa, R.R. Gattass, V. Nguyen, G. Chin, D. Gibson, W. Kim, L.B. Shaw, J.S. Sanghera, Opt. Lett. **40**(21), 5074 (2015)

[108] L.R. Robichaud, V. Fortin, J.C. Gauthier, S. Châtigny, J.F. Couillard, J.L. Delarosbil, R. Vallée, M. Bernier, Opt. Lett. **41**(20), 4605 (2016)

[109] S.B. Mirov, V.V. Fedorov, D. Martyshkin, I.S. Moskalev, M. Mirov, S. Vasilyev, IEEE Journal of Selected Topics in Quantum Electronics **21**(1), 292 (2015)

[110] A.M. Jones, A.V. Nampoothiri, A. Ratanavis, T. Fiedler, N.V. Wheeler, F. Couny, R. Kadel, F. Benabid, B.R. Washburn, K.L. Corwin, et al., Opt. Express **19**(3), 2309 (2011)

[111] J. Faist, Quantum Cascade Lasers (Oxford University Press, 2013)

[112] R.F. Curl, F. Capasso, C. Gmachl, A.A. Kosterev, B. McManus, R. Lewicki, M. Pusharsky, G. Wysocki, F.K. Tittel, Chemical Physics Letters **487**(1), 1 (2010)

[113] F. Capasso, Optical Engineering **49**(11), 111102 (2010)

[114] Y. Yao, A.J. Hoffman, C.F. Gmachl, Nature Photonics **6**(7), 432 (2012)

[115] B. Bureau, C. Boussard, S. Cui, R. Chahal, M.L. Anne, V. Nazabal, O. Sire, O. Loréal, P. Lucas, V. Monbet, et al., Optical Engineering **53**(2), 027101 (2014)

[116] L. Nugent-Glandorf, T. Neely, F. Adler, A.J. Fleisher, K.C. Cossel, B. Bjork, T. Dinneen, J. Ye, S.A. Diddams, Opt. Lett. **37**(15), 3285 (2012)

[117] L. Nugent-Glandorf, F.R. Giorgetta, S.A. Diddams, Applied Physics B **119**(2), 327 (2015)

[118] R.W. Boyd, Nonlinear Optics, 3rd edn. (Elsevier Inc., 2008)

[119] J. Seres, J. Hebling, JOSA B **17**, 741 (2000)

[120] J.M. Dudley, G. Genty, S. Coen, Rev. Mod. Phys. **78**, 1135 (2006)

[121] M. Fox, Optical Properties of Solids (Oxford Master Series in Physics) (Oxford University Press, 2010)

[122] P.L. Francois, JOSA B **8**(2), 276 (1991)

[123] A.M. Heidt, Journal of Lightwave Technology **27**(18), 3984 (2009)

[124] G. Agrawal, Nonlinear Fiber Optics (Academic Press, 2013)

[125] K.J. Blow, D. Wood, IEEE Journal of Quantum Electronics **25**(12), 2665 (1989)

[126] F. DeMartini, C.H. Townes, T.K. Gustafson, P.L. Kelley, Phys. Rev. **164**, 312 (1967)

[127] A. Schliesser, N. Picqué, T.W. Hänsch, Nature Photonics **6**(7), 440 (2012)

[128] S.T. Yang, R.C. Eckardt, R.L. Byer, JOSA B **10**, 1684 (1993)

[129] M. Ebrahimzadeh, in Solid-State Mid-Infrared Laser Sources, ed. by I.T. Sorokina, K.L. Vodopyanov (Springer-Verlag, 2003)

[130] Z. Zhang, T. Gardiner, D.T. Reid, Opt. Lett. **38**(16), 3148 (2013)

[131] K.F. Lee, J. Jiang, C. Mohr, J. Bethge, M.E. Fermann, N. Leindecker, K.L. Vodopyanov, P.G. Schunemann, I. Hartl, Opt. Lett. **38**(8), 1191 (2013)

[132] N. Leindecker, A. Marandi, R.L. Byer, K.L. Vodopyanov, J. Jiang, I. Hartl, M. Fermann, P.G. Schunemann, Opt. Express **20**, 7046 (2012)

[133] R. Gebs, T. Dekorsy, S.A. Diddams, A. Bartels, Opt. Express **16**(8), 5397 (2008)

[134] S.T. Wong, T. Plettner, K.L. Vodopyanov, K. Urbanek, M. Digonnet, R.L. Byer, Opt. Lett. **33**(16), 1896 (2008)

[135] S.T. Wong, K.L. Vodopyanov, R.L. Byer, JOSA B **27**(5), 876 (2010)

[136] M.H. Dunn, M. Ebrahimzadeh, Science **286**, 1513 (1999)

[137] F. Adler, S.A. Diddams, Opt. Lett. **37**, 1400 (2012)

[138] K. Ohta, H. Ishida, Applied Spectroscopy **42**, 952 (1988)

[139] S. Kumkar, G. Krauss, M. Wunram, D. Fehrenbacher, U. Demirbas, D. Brida, A. Leitenstorfer, Opt. Lett. **37**(4), 554 (2012)

[140] H. Hoogland, A. Thai, D. Sánchez, S. Cousin, M. Hemmer, M. Engelbrecht, J. Biegert, R. Holzwarth, Opt. Express **21**(25), 31390 (2013)

[141] K.W. DeLong, R. Trebino, J. Hunter, W.E. White, JOSA B **11**(11), 2206 (1994)

[142] R.L. Fork, O.E. Martinez, J.P. Gordon, Opt. Lett. **9**(5), 150 (1984)

[143] R.E. Sherriff, J. Opt. Soc. Am. B **15**(3), 1224 (1998)

[144] J.W. Nicholson, A. Yablon, P. Westbrook, K. Feder, M. Yan, Opt. Express **12**(13), 3025 (2004)

[145] I. Coddington, W.C. Swann, N.R. Newbury, Opt. Lett. **35**(9), 1395 (2010)

[146] D.S. Hum, M.M. Fejer, Comptes Rendus Physique **8**(2), 180 (2007)

[147] J.C. Diels, W. Rudolph, Ultrashort Laser Pulse Phenomena, Second Edition (Optics and Photonics Series) (Academic Press, 2006)

[148] S. Witte, R. Zinkstok, W. Hogervorst, K. Eikema, Applied Physics B **87**(4), 677 (2007)

[149] I.N. Ross, P. Matousek, G.H.C. New, K. Osvay, J. Opt. Soc. Am. B **19**(12), 2945 (2002)

[150] G. Krauss, S. Lohss, T. Hanke, A. Sell, S. Eggert, R. Huber, A. Leitenstorfer, Nature Photonics **4**(1), 33 (2010)

[151] H. Mabuchi, E. Poizik, H.J. Kimble, JOSA B **11**(10), 2023 (1994)

[152] N.R. Newbury, I. Coddington, W. Swann, Opt. Express **18**(8), 7929 (2010)

[153] N. Singh, D.D. Hudson, Y. Yu, C. Grillet, S.D. Jackson, A. Casas-Bedoya, A. Read, P. Atanackovic, S.G. Duvall, S. Palomba, et al., Optica **2**(9), 797 (2015)

[154] D.Y. Oh, K.Y. Yang, C. Fredrick, G. Ycas, S.A. Diddams, K.J. Vahala, Nature Communications **8**, 13922 (2017)

Appendix A

Mathematical Identities

The following identities are used in Chapter 2 [118, 119]:

The curl of a curl:

$$\nabla \times \nabla \times \mathbf{A} = \nabla(\nabla \cdot \mathbf{A}) - \nabla^2 \mathbf{A} \tag{A.1}$$

Derivatives between Fourier domains (where F is in the time domain and f is in the frequency domain):

$$\frac{\mathrm{d}^n F}{\mathrm{d}t^n} \leftrightarrow (i\omega)^n f \tag{A.2}$$

Convolution:

$$\begin{aligned} f \otimes g &= \int_{-\infty}^{\infty} f(\tau) g(t-\tau) \mathrm{d}\tau & \text{(A.3)} \\ &= \int_{-\infty}^{\infty} f(t-\tau) g(\tau) \mathrm{d}\tau & \text{(A.4)} \end{aligned}$$

Cross-correlation:

$$f \oplus g = \int_{-\infty}^{\infty} f^*(\tau) g(t+\tau) \mathrm{d}\tau \tag{A.5}$$

Transferring a convolution between Fourier domains:

$$FG \longleftrightarrow \frac{1}{2\pi} f \otimes g \tag{A.6}$$

Transferring a cross-correlation between Fourier domains:

$$FG^* \longleftrightarrow \frac{1}{2\pi} f \oplus g \tag{A.7}$$

Appendix B

List of Part Numbers and Manufacturers Used in Dissertation

B.1 Oscillators

Component	**Manufacturer**	**Part Number**
frequency comb	MenloSystems	100 MHz C-Comb

Table B.1: Commercial oscillator used as basis for near-infrared frequency comb system.

B.2 EDFA

Component	**Manufacturer**	**Part Number**
PANDA PM 1550	Corning	PM 15-U25D
fiber bench	Thorlabs	FB-51W
fiber port	Thorlabs	PAF-X-2-C
quarter-wave plate	Thorlabs	FBR-AQ3
half-wave plate	Thorlabs	FBR-AH3
optical isolator	Thorlabs	IO-4-1550-VLP
fiber bench adapter for isolator	Thorlabs	H1C
45 nm bandpass filter	Omega Optical	1550DF45
PM 980/1550 WDM	AFW	WDM-PM-1598
(alt. WDM vendor)	(Gooch & Housego)	(FPW-980C50110)
PM EDF	nLight LIEKKI	Er80-4/125-PM-HD
980 pump diode	Gooch & Housego	AC1409-0980-0700-PM
(alt. pump diode vendors)	(Lumentum, 3S Photonics, II-IV)	(N/A)
980 pump combiner	Gooch & Housego	FFP-5M3180G210
PM LMA fiber	Nufern	PLMA-GDF-15/130

Table B.2: List of parts used in PM EDFA and pulse compression testing in Chapter 4.

B.3 YDFA Pre-Amp

Component	**Manufacturer**	**Part Number**
PM 980/1064 WDM	AFW	WDM-PM-9864
PM 1064 isolator	AFW	PISO-64-2
PM YDF	Nufern	PM-YSF-HI
976 pump diode	Gooch & Housego	AC1409-0976-0700-PM

Table B.3: List of parts used in the PM YDFA. This device is used as a pre-amplifier to see the high-power ytterbium amplifier, used in difference frequency generation in Chapters 5 and 6.

B.4 High-Power YDFA

Component	**Manufacturer**	**Part Number**
Yb amplifier	Keopsys	CYFA-PB-BW1-PM-33-NL1-OM1-M305-FA-FA
PM YDF	Nufern	PLMA-YDF-10/125-HI-8
transmission gratings	Lightsmyth	T-1600-1030s
976 pump diode	Gooch & Housego	AC1409-0976-0700-PM

Table B.4: Full list of parts used in the high-power PM YDFA used in difference frequency generation in Chapters 5 and 6

B.5 Pump Diode Controller Infrastructure

Component	**Manufacturer**	**Part Number**
diode controller module	ILX-Lightwave	LDC-3916376
diode controller mainframe	ILX-Lightwave	LDC-39XX
pump diode butterfly mount chassis	ILX-Lightwave	LDM-4616

Table B.5: Hardware required for pump diode current and TEC control.

B.6 Nonlinear Crystals

Component	**Manufacturer**	**Part Number**
$AgGaSe_2$	Altechna/Magic Photonics	5x5x1, $\theta = 52.8°$, $\phi = 45°$
MgO:PPLN (Chapter 5)	Covesion	MOPO1-0.5-X (1, 3)
MgO:PPLN (Chapter 6)	Covesion	MSHG3100-0.5-X (1, 3)

Table B.6: Nonlinear crystals featured in Chapters 3, 5, and 6.

B.7 Diagnostics

Component	**Manufacturer**	**Part Number**
TEC-cooled MIR detector	Vigo	PVI-2TE-5 / MIPAC-F-100
LN_2-cooled MIR detector	Kolmar Technologies	KV104-0.1-E/11 / KA200
LN_2-cooled MIR camera	IRCameras	IRC800

Table B.7: Diagnostic tools used in the mid-infrared.